TITLE:

STUDIES ON SHOCK VIBRATION CONTROL BY MOMENTUM EXCHANGE IMPACT DAMPER(Dissertation_全文)

AUTHOR(S):

Son, Lovely

CITATION:

Son, Lovely. STUDIES ON SHOCK VIBRATION CONTROL BY MOMENTUM EXCHANGE IMPACT DAMPER. 京都大学, 2007, 博士(工学)

ISSUE DATE:

2007-09-25

URL:

https://doi.org/10.14989/doctor.k13388

RIGHT:

京都大学学術情報リポジトリ
KURENAI 紅
Kyoto University Research Information Repository

STUDIES

ON SHOCK VIBRATION CONTROL

BY

MOMENTUM EXCHANGE IMPACT DAMPER

Lovely SON

TABLE OF CONTENTS

Table of Contents **i**
List of Figures **iii**
List of Tables **vii**

Chapter 1 INTRODUCTION **1**
1.1 Problem statement 1
1.1.1 Flexible Support 2
1.1.2 Bumpered Vibration Isolator 3
1.1.3 Dynamic Vibration Absorber 4
1.1.4 Dynamic Damper with Preview Action 5
1.2 Research Scope and Objectives 7
1.3 Contribution 7
1.4 Outline of the Dissertation 8

Chapter 2 THREE BODIES COLLISION PROBLEM **9**
2.1 Introduction 9
2.2 Rigid Body Collision 9
2.2.1 Solution by Assumption of Contact Spring 9
2.2.2 Solution Using the Coefficient of Restitution 15
2.3 Elastic Rod Collision 17
2.4 Experiment 22
2.4.1 Rigid Body Collision 22
2.4.2 Elastic Rod Collision 26
2.5 Summary 28

Chapter 3 REDUCING FLOOR IMPACT VIBRATION AND SOUND USING A MOMENTUM EXCHANGE IMPACT DAMPER **29**
3.1 Introduction 29
3.2 Flooring System with Impact Damper 29
3.3 Theoretical Model and Identification 30
3.4 Sound Pressure Calculation 34
3.5 Simulation Result 38
3.6 Experimental Result 42

3.7 Summary 45

Chapter 4 APPLICATION OF MOMENTUM EXCHANGE IMPACT DAMPER TO FORGING MACHINE 46

4.1 Introduction 46
4.2 New Impact Damper for Forging Machine 46
4.3 System Modeling and Equations of Motion 47
4.4 Energy Transfer and Transmitted Force 49
4.4.1 Case 1: Using Floating Base with Soft Support Springs 50
4.4.2 Case 2: Using Floating Base with Hard Support Springs 59
4.4.3 Case 3: Without Floating Base 61
4.5 Experimental Validation 64
4.6 Summary 66

Chapter 5 APPLICATION OF MOMENTUM EXCHANGE IMPACT DAMPER TO BOAT 67

5.1 Introduction 67
5.2 Two Degree of Freedom Model of Boat with Impact Damper 67
5.3 Laboratory Model 75
5.3.1 Pinned Beam Model 75
5.3.2 Small Scale Boat Model 85
5.4 Experiment **89**
5.4.1 Pinned Beam Model 89
5.4.2 Small Scale Boat Model 91
5.5 Summary 91

Chapter 6 CONCLUSIONS 93

6.1 Summary 93
6.2 Recommendation for Future Research 94
6.2.1 Full-scale Test 94
6.2.2 Modification of MEID 94

APPENDIX
BIBLIOGRAPHY
ACKNOWLEDGEMENTS

LIST OF FIGURES

Figure 1.1 Flexible support
Figure 1.2 Transmissibility diagrams
Figure 1.3 Vibration isolation with bumper
Figure 1.4 Dynamic Vibration Absorber (DVA)
Figure 1.5 Dynamic absorber with preview action
Figure 1.6 Three-ball cradle
Figure 1.7 Configuration of momentum exchange impact damper
Figure 2.1 Rigid body collision
Figure 2.2 Collision model of rigid body
Figure 2.3 Transfer of energy in collision of rigid bodies
Figure 2.4 Time history for $\omega_b/\omega = 1.25$
Figure 2.5 Time history for $\omega_b/\omega = 2.5$
Figure 2.6 Collision of free elastic rod
Figure 2.7 Transfer of energy of the free rod
Figure 2.8 Time history for $\omega_b/\omega_1=0.8$
Figure 2.9 Time history for $\omega_b/\omega_1=1.1$
Figure 2.10 Time history for $\omega_b/\omega_1=2$
Figure 2.11 Experimental apparatus for collision of rigid body
Figure 2.12 Influence of leaf spring size on cylinder acceleration for $\mu = 0.25$
Figure 2.13 Influence of leaf spring size on cylinder acceleration for $\mu = 0.75$
Figure 2.14 Influence of leaf spring size on rod displacement for $\mu = 0.25$
Figure 2.15 Transfer of energy of rigid body
Figure 2.16 Experimental setup for collision of elastic rod
Figure 2.17 Experimental setup for determining the contact stiffness
Figure 2.18 Elastic rod energy transfer
Figure 3.1 Experimental apparatus of the flooring system with impact damper
Figure 3.2 Model of flooring system with impact damper
Figure 3.3 Determination of k_{cb} and c_{cb}
Figure 3.4 Floor, support frame and slab mode shape
Figure 3.5 Frequency responses of floor and slab system
Figure 3.6 The room bellow the slab
Figure 3.7 Simulation results of acceleration in point B
Figure 3.8 Simulation results of velocity in point O_s

Figure 3.9 Simulation results sound pressure in the wooden box
Figure 3.10 Simulation results comparison of acceleration response
Figure 3.11 Simulation results comparison of sound pressure
Figure 3.12 Experimental results of acceleration in point B
Figure 3.13 Experimental results sound pressure in the wooden box
Figure 3.14 Experimental results comparison of acceleration response
Figure 3.15 Experimental results comparison of sound pressure
Figure 4.1 Experimental model of press machine
Figure 4.2 Significant mode shapes of bed, column and floating base system
Figure 4.3 Relationship between energy transfer and contact condition
Figure 4.4 Relationship between energy transfers and mass ratio
Figure 4.5 Variation of energy ratio with frequency ratio ω_s/ω_6 and mass ratio m_d/m_b
Figure 4.6 Energy time history for m_d/m_b =0.35, ω_s/ω_6=150 and ω_d/ω_6 =150 (point Q)
Figure 4.7 Energy time history for m_d/m_b =0.35, ω_s/ω_6=150 and ω_d/ω_6 =25 (point P)
Figure 4.8 Energy time history for m_d/m_b =0.35, ω_s/ω_6=150 and ω_d/ω_6 =220 (point R)
Figure 4.9 Comparison between added mass and impact damper method
Figure 4.10 Simulation results of acceleration at point S
Figure 4.11 Simulation results of transmitted force at point S
Figure 4.12 Relationship between energy transfer and contact condition for $K_f = 1\times 10^7$
Figure 4.13 Simulation results of acceleration at point T
Figure 4.14 Simulation results of transmitted force point T
Figure 4.15 Several mode shapes of press machine without using floating base
Figure 4.16 Relationship between energy transfer and contact condition without floating base
Figure 4.17 Variation of energy with ratio frequency ω_s/ω_4 and mass ratio m_d/m_b
Figure 4.18 Simulation results of acceleration at point U ($\omega_s = \omega_d$)
Figure 4.19 Simulation results of transmitted force at point U ($\omega_s = \omega_d$)
Figure 4.20 Photo of experimental apparatus
Figure 4.21 Experimental results of acceleration
Figure 4.22 Experimental results of transmitted force
Figure 5.1 Two degree of freedom model

Figure 5.2 Acceleration ratio of mass m
Figure 5.3 Time history for $m_d/m = 0.6$
Figure 5.4 One degree of freedom equivalent model
Figure 5.5 Optimal value of contact parameter
Figure 5.6 Laboratory model of impact of boat
Figure 5.7 Mode shape of beam
Figure 5.8 Beam energy variation
Figure 5.9 Time history for $\omega_w/\omega_1=9$
Figure 5.10 Energy profile of beam mode shape without impact damper with $\omega_w/\omega_1=9$
Figure 5.11 Energy profile of beam mode shape with $\omega_w/\omega_1=9$ and $\omega_d/\omega_1=5$
Figure 5.12 Energy profile of beam mode shape with $\omega_w/\omega_1=9$ and $\omega_d/\omega_1=5$ at point P
Figure 5.13 Energy profile of beam mode shape with $\omega_w/\omega_1=9$ and $\omega_d/\omega_1=40$
Figure 5.14 Beam energy for $\omega_w= 4.7\times 10^3$ N/m
Figure 5.15 Variation of minimum beam energy
Figure 5.16 Acceleration response for $K_{cw}= 5\times 10^5$ and K_d calculated from Eq.(5.45)
Figure 5.17 Comparison between impact damper and added mass method
Figure 5.18 The small scale model of the boat
Figure 5.19 Small scale boat and impact damper model
Figure 5.20 Contact area between boat and water
Figure 5.21 Location of impact damper
Figure 5.22 Four lowest mode of the boat
Figure 5.23 Acceleration ratio of the boat
Figure 5.24 Experimental setup beam and ball
Figure 5.25 Comparison between experiment and calculation result of transfer function
Figure 5.26 Acceleration response of pinned beam
Figure 5.27 Experimental setup of the boat
Figure 5.28 Comparison between simulation and experimental result
Figure A.1 Elastic element
Figure A.2 Plate element
Figure A.3 Three dimensional frame element
Figure A.4 Displacement in *x-y* plane
Figure A.5 Displacement in *x-z* plane

Figure A.6 Axes rotation in 3 dimensional space
Figure A.7 The P point in space frame

LIST OF TABLES

Table 2.1	Simulation parameters for rigid body collision
Table 2.2	Final Energy given by the coefficient of restitution method
Table 2.3	Simulation parameters of elastic rod collision
Table 2.4	Experimental parameters for rigid body collision
Table 2.5	Natural frequency of the supported rod
Table 2.6	Contact stiffness and contact frequency
Table 3.1	Variation of k_{cb} and c_{cb}
Table 4.1	Simulation parameters for floating base,column, damper, slider, and bed
Table 5.1	Simulation parameters
Table 5.2	Simulation parameters for response calculation
Table A.1	The shape function and its differentiation for 3D frame element

Chapter 1
INTRODUCTION

1.1 Problem Statement

Impact occurs when two bodies collide during a very short time period, causing large impulsive forces to be exerted between the bodies (Goldsmith, 1960; Chatterjee , 1997, 1999; Chatterjee and Ruina, 1998; Brach, 1991). Commonly, the impulsive forces exerted during collision always excite all vibration modes of the colliding bodies (Son and Matsuhisa, 2006; Fegelman and Gross, 2002). Moreover, most of impact problems for human body occur at low natural frequency range, generally less than 10 Hz (McKay, 1972).

Recently, low frequency impact problems become common problem in industrial and social area (Tanaka and Kikushima, 1986, 1987; Hanagan and Muray, 1994, 1997). Moreover, the low frequency components of the vibration mode usually have less inherent damping (Setareh and Hanson, 1992; Webster and Vaicajtis, 1992). The large vibration response and transmitted force in the processing machines using impact force such as forging machines is one example of impact problems found in the industry. These problems decrease the machining accuracy and cause vibration pollution to surroundings, which is transmitted by machine base structure. Another example of impact problem is vibration of floor on the multistory mansion or apartment caused by shock excitation by human activities such as walking, dancing, jumping etc (Allen and Pernica, 1984). This excitation force induced the floor vibration and noise to the ceiling of the lower room. The impact problem also affects the safety and comfort in the transportation system such as a boat. When the boat was driven at a high-speed level, the crew of boat will have a large shock when it was impacted by a big wave.

There are many methods can be used to reduce the impact vibration. Conventional methods such as using an added mass, rubber mounting and a passive dynamic vibration absorber (DVA) have limitation and can be disruptive if the parameter has changed (Collette, 1998). There have been several attempts to use the semi active and active control methods to address this problem, but disadvantages such as cost and the need for frequent maintenance limit their use (Wu and Griffin, 1997; Tanaka and Kikushima, 1986, 1987; Kim and Park, 2002). In general, there has been limited success in finding appropriate control method for impact problem. Some of previous works for reducing the impact vibration are described bellows

1.1.1 Flexible Support

When machine or engine is rigidly attached to supporting structure, the vibration originating from it is transmitted directly to the support, thus often resulting in undesirable vibrations of the surrounding structure. To reduce transmitted vibration to minimum, the disturbing source must be isolated by means of flexible support (Timoshenko, 1974).

Figure 1.1(a) shows a schematic diagram of an isolated system. The vibratory force F_t originating in the supported mass can influence the foundation only through the spring and dashpot hence the transmitted force F_{TR} is represented by the sum of the damping force and spring force. The vector diagram of the force components is depicted in Fig. 1.1 (b), the transmitted force and acting force are calculated as

$$F_{TR} = \sqrt{(kX)^2 + (cX\omega)^2} = X\sqrt{k^2 + (c\omega)^2}\,, \tag{1.1}$$

$$F_0 = \sqrt{\left(kX - mX\omega^2\right)^2 + (cX\omega)^2} = X\sqrt{\left(k - m\omega^2\right)^2 + (c\omega)^2}\,. \tag{1.2}$$

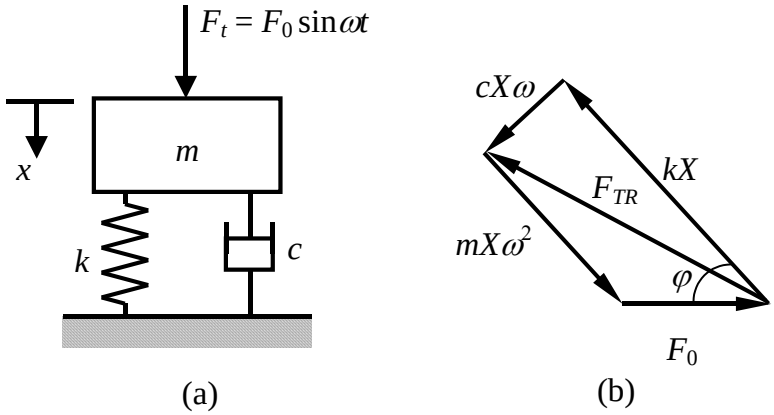

Fig. 1.1 Flexible support.

F_0 is the disturbing force, which is transmitted directly to foundation if the system is rigidly attached without springs. F_{TR}/F_0 represents the ratio of the force transmitted through the flexible support to the force transmitted directly when mounted rigidly, and is called the transmissibility *TR* of the system.

$$TR = \frac{F_{TR}}{F_0} = \sqrt{\frac{k^2 + (c\omega)^2}{\left(k - m\omega^2\right)^2 + (c\omega)^2}}\,, \tag{1.3}$$

In nondimensional form, Eq. (1.3) can be written as

$$TR = \sqrt{\frac{1+(2\zeta\eta)^2}{(1-\eta^2)^2+(2\zeta\eta)^2}}\,. \tag{1.4}$$

where $\zeta = c/2\sqrt{mk}$, $\eta = \omega/\omega_0$ and $\omega_0 = \sqrt{k/m}$ are damping ratio, frequency ratio and natural frequency, respectively. Fig. 1.2 shows the transmissibility for various value of ζ. It is shown that all curves pass through $TR = 1$ when $\eta = \sqrt{2}$. The transmitted force is greater than the value for rigid mounting when $\eta < \sqrt{2}$ and less than the value for rigid mounting when $\eta > \sqrt{2}$. It follows that vibration isolation is possible only in the region $\eta > \sqrt{2}$. In the region $\eta > \sqrt{2}$, where vibration isolation is effective, the damping tends to increase the transmitted force. Contrariwise in region $\eta < \sqrt{2}$ the damping limits transmitted force. In point of view of vibration suppression, the damping should be as high as possible in order to obtain high vibration suppression. According to this condition, the flexible support cannot be used for vibration isolation and suppression simultaneously.

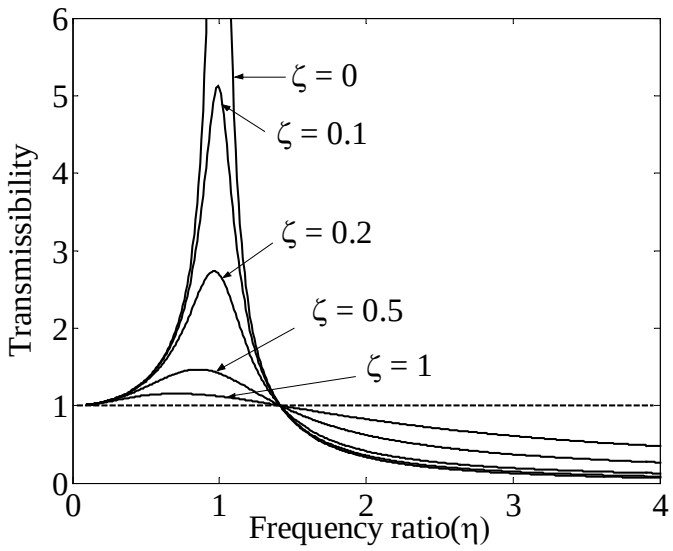

Fig. 1.2 Transmissibility diagrams.

1.1.2 Bumpered Vibration Isolator

The limiting of vibratory energy transmission from a machine to its foundation and vice versa may be achieved by the proper use of flexible support. If the natural frequencies of the resiliently suspended machine are located well below the lowest frequency in the excitation spectrum, a significant attenuation of vibration transmission may be achieved in a certain high-frequency range. In this case, it is recommended to use a soft and undamped flexural suspension.

In fact, such a simple vibration isolator is feasible in a limited number of cases of moderate environmental disturbances. As soon as an application involves exposure to severe environmental disturbances such as shock, the spectrum of excitation already contains dangerous low frequency components. The low frequency and undamped isolator under such condition exhibits excessive deflections that can over-stress the flexural suspension and even damage the machine and enclosure.

Due to the possible low frequency amplification, the flexible suspension is supplied with considerable free oscillation space to avoid impacts against the machine enclosure. In order to protect a machine and its enclosure from unavoidable excessive motions, the pre-designed deflection limiters (bumpers) are usually an integral component of a vibration isolation arrangement (Babitsky and Veprik, 1998). When the sufficient stiffness and damping is used, bumpers can effectively trim machine deflection in an emergency. Figure 1.3 shows the vibration isolation with bumper.

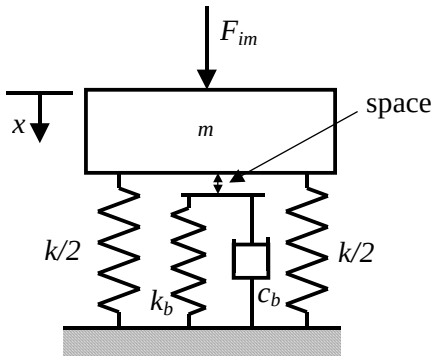

Fig. 1.3 Vibration isolation with bumper.

1.1.3 Dynamic Vibration Absorber

The dynamic vibration absorber DVA usually used to suppress the vibration level of system with steady state excitation (Webster and Vaicajtis, 1992). The application of DVA for reducing the transmitted force of transient vibration is reported by Tanaka (Tanaka and Kikushima, 1986). Figure 1.4 shows the schematic of system with DVA as reported in reference. The effect of DVA is significantly determined by mass ratio m_d/m. According to the reference, the reduction of maximum transmitted force by using the DVA with mass ratio 0.2 is 8.2 %. As reported in the reference, the DVA fails to suppress the first wave of transient response due to the delay of the damper motion.

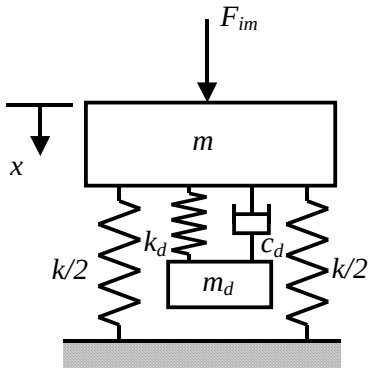

Fig. 1.4 Dynamic Vibration Absorber (DVA).

1.1.4 Dynamic Damper with Preview Action

Active control of impact vibration by using dynamic damper with preview action was proposed by Tanaka (Tanaka and Kikushima, 1987). Figure 1.5 shows the schematic of dynamic damper with preview action. In this method the optical sensor is used to determine the action time. The actuators are consisting of a mass, which is rigidly attached to the push rod. The pre load using initial deflection of coil spring is applied to the rod. The constant deflection of coil spring is accomplished by using a clamp, which is driven by hydraulic force. The rod is initially positioned at a small free space from the main mass *m*. When the impact load excites mass *m*, the impulsive force exerted by this impact load is counteracting by kinetic energy from the rod, which is generated by releasing the preload spring.

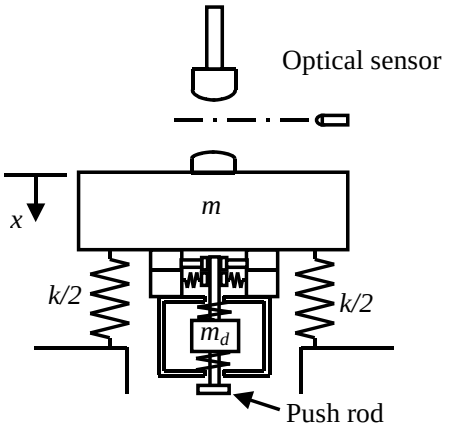

Fig. 1.5 Dynamic absorber with preview action.

This research proposes a new impact damper as an alternative means for reducing excessive impact vibrations. The applications of momentum exchange impact damper (MEID) in reducing the shock vibration are reported in reference (Son and Matsuhisa, 2006, Friend and Kinra, 2000, Peterka and Blazejczyk, 2005). The principle of MEID is

similar to the three-ball cradle system as shown in Fig. 1.6 (Newton, 1976; Ceanga and Hurmuzlu, 2001; Herrmann and Schmalzle, 1981 ; Herrmann and Seitz, 1984). When the first ball collides the second ball, a part of its kinetic energy is transferred to the second ball (Reinsch, 1994). A part of kinetic energy of the second ball is simultaneously transferred to the third ball when the second ball collides with the third ball. Consequently, the second ball has a small force induced and it can be possible to keep the second ball stable.

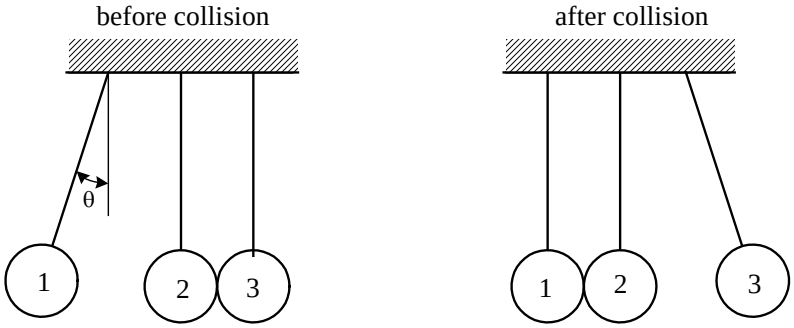

Fig. 1.6 Three-ball cradle.

The MEID was developed by analogy to the three-ball cradle system. In this analogy the first, second and third ball were regarding as the impact source, main body and the absorber, respectively. Figure 1.7 shows two configurations of the system using impact damper. In the first configuration depicted on Fig. 1.7 (a), the main body consists of a mass and a spring system. In this configuration, the collision can be regarded as the rigid body collision problem (Routh, 1897, Whittaker, 1947) and the transfer of energy and momentum during collision is depending on the contact frequency and mass ratio between both masses. For the second configuration as shown in Fig. 1.7 (b), the main body is a continuous body that has many elastic modes. In this case the transfer of energy and momentum is influenced by each vibration mode of the body (Stoianovici and Hurmuzlu, 1996).

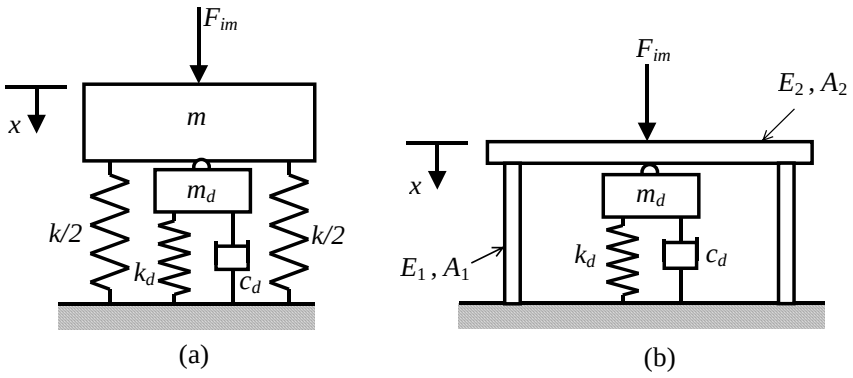

Fig. 1.7 Configuration of momentum exchange impact damper.

One application of MEID is in the floor impact vibration where MEID was used to reduce the floor vibration and transmitted force (Son and Matsuhisa, 2006). In the application described in the reference, MEID was put on the slab under the floor. The mass of MEID is contacted to the floor. When a falling object collides with the floor, the floor interacts with the absorber mass and momentum of the falling object is transferred to the absorber mass.

One of important feature of MEID, which is not obtained from conventional method is its ability to reduce the first wave of transient response. In the conventional method such as Dynamic Vibration Absorber (DVA), the first wave of transient response is not significantly reduced due to the delay of the damper motion. By using the MEID, the transient response could be reduced because the collision between impact damper and main body occurs simultaneously after the main body impacted by impact source.

1.2 Research Scope and Objectives

This study focuses on development of the new control method using MEID and dynamic evaluation of the system controlled by MEID. Therefore, this research intends to develop a new type of impact control that uses the momentum exchange principle. It also intends to asses the comprehensive dynamics of the system with MEID. The primary objectives of this study can be summarized as follows:

(1) To evaluate the dynamics of the system using MEID
(2) To investigate the optimum parameter of MEID to transfer the maximum energy during collision.
(3) Application of MEID to several impact problems such as a flooring system, a forging machine and a boat.

1.3 Contribution

The findings of this research will contribute to the development of a new class of vibration absorber for reducing impact vibrations in structures and mechanical systems. This impact damper demonstrates superior performance in reducing the low frequency impact vibration level and proves to have better performance than conventional passive control system. Moreover, the MEID is more cost effective and maintenance free than a comparable active control system. Therefore, the current research is anticipated to contribute the broader application of the MEID to mechanical and structural systems.

More specific contributions of this research include:

- This research demonstrates the optimal parameter of MEID for specific application of the impact damper
- This study, numerically and experimentally, evaluates various application of MEID. Based on these results, it suggests an adequate design parameter of MEID for each application.
- The experimental result will serve as a valuable proof of concept MEID for full-scale application and field use.
- The outcomes of this research will be the foundation of further research into the use of MEID for structures and mechanical vibration control.

1.4 Outline of the Dissertation

The next chapter, Chapter 2 presents the basic principle of MEID modeled as collision of three-body system. It covers the comprehensive dynamic analysis of two types of three-body collision systems. Chapter 3 presents the application of MEID to floor system. This chapter investigates the numerical calculation of floor vibration response and sound generation in the room bellow the slab. Moreover, experimental investigation to the scale model of floor system is also conducted to validate the simulation result. Chapter 4 evaluates the application of MEID to forging machine. Several configuration of forging machine using MEID is investigated in this chapter. The application of MEID to boat system is presented in Chapter 5. A Simple two DOF model of boat and impact damper system was proposed to investigate the best parameter of impact damper for boat application. Finally, chapter 6 provides a summary of the work. Significant results are highlighted, and recommendation for the future research also discussed.

Chapter 2
THREE BODIES COLLISION PROBLEM

2.1 Introduction

Impact induced vibrations has recently received a great deal of attention in industrial and social environments. Accompanying noise generation and large impact force transmission to the surrounding are the primary motivation for studying such problems (Schedin and Lambourge, 1999). Many researchers have carried out studies in this area and a number of methods have been developed to solve such problems (Hu and Eberhard, 2001; Hurmuzlu, 1998; Lee and Byrne, 1998).

The momentum exchange method using an impact damper was proposed to reduce the vibration and force transmission in impact induced vibration problems. By using these impact dampers, part of kinetic energy of the main body is transferred to the absorber mass during collision. This type of absorber can reduce the impact shock of the main body.

In the work presented in this chapter, the effect of the contact condition between main body and both the impact mass and the absorber mass to the amount of energy transfer is investigated. Two simple models, a spring-supported rigid rod and an elastic rod, are used as the main body to study the energy exchange within an impact damper. The relationship between the natural frequency of the main body and the contact frequencies of the impact source and the impact damper are investigated theoretically and experimentally.

2.2 Rigid Body Collision

2.2.1 Solution by Assumption of Contact Spring

The main body consists of a mass m and support spring k. An impact source mass m_b collides m with initial velocity v_{b-}. Before collision, the impact damper mass m_d is contacting with m. When the collision takes place, as shown in Fig. 2.1, the momentum and the kinetic energy of m_b is transferred to m and m_d. The momentum and energy exchanges continue while the masses remain in contact with each other.

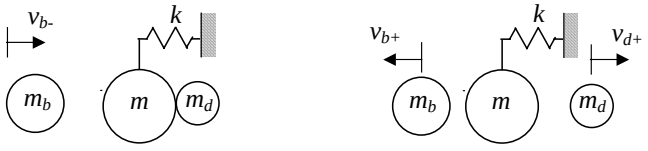

Before collision After collision

Fig. 2.1 Rigid body collision.

In this study, the contact condition is assumed to be given by linear springs k_b and k_d as shown in Fig. 2.2. This linear spring model is appropriate to be used in some engineering application (Rajaligham and Rakheja, 2000)

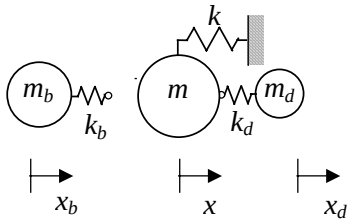

Fig. 2.2 Collision model of rigid body.

The governing equations of the three rigid bodies in Fig. 2.2 are given by

$$m_b\ddot{x}_b + f_b = 0, \tag{2.1}$$

$$m\ddot{x} + kx - f_b + f_d = 0, \tag{2.2}$$

$$m_d\ddot{x}_d - f_d = 0, \tag{2.3}$$

where x_b, x and x_d are the displacements of the impact mass, main body, and absorber mass, respectively. The variable f_b is the contact force between m and m_b and f_d is contact force between m and m_d. These forces are given by

$$f_b = \begin{cases} k_b\left(x_b - x\right), & for \;\; x_b - x \geq 0, \\ 0, & for \;\; x_b - x < 0, \end{cases} \tag{2.4}$$

$$f_d = \begin{cases} k_d\left(x - x_d\right), & for \;\; x - x_d \geq 0, \\ 0, & for \;\; x - x_d < 0. \end{cases} \tag{2.5}$$

The transfers of energy from m_b to m_d and m after collision are calculated as

$$\frac{E_{d+}}{E_{b-}} = \frac{\frac{1}{2}m_d v_{d+}^2}{\frac{1}{2}m_b v_{b-}^2}, \tag{2.6}$$

$$\frac{E}{E_{b-}} = 1 - \frac{\frac{1}{2}m_b v_{b+}^2}{\frac{1}{2}m_b v_{b-}^2} - \frac{\frac{1}{2}m_d v_{d+}^2}{\frac{1}{2}m_b v_{b-}^2}, \tag{2.7}$$

where v_{b+} and v_{d+} are the velocity of m_b and m_d after collision.

When $f_b \neq 0$ and $f_d \neq 0$, the three masses remain in contact with each other. In this state, the solution of Eq. (2.1)-(2.3) is given by the combination of three harmonic

functions relating to the natural frequencies of the system. The response of mass m_d is calculated as

$$x_d(t) = r_b\omega_b^2\omega_d^2 v_{b-}\left[\frac{1}{\omega_1\left(\omega_1^2-\omega_2^2\right)\left(\omega_1^2-\omega_3^2\right)}\sin\omega_1 t - \frac{1}{\omega_2\left(\omega_1^2-\omega_2^2\right)\left(\omega_2^2-\omega_3^2\right)}\sin\omega_2 t\right.$$

$$\left. + \frac{1}{\omega_3\left(\omega_1^2-\omega_3^2\right)\left(\omega_2^2-\omega_3^2\right)}\sin\omega_3 t\right], \tag{2.8}$$

where

$$\omega_b = \sqrt{\frac{k_b}{m_b}}, \quad \omega_d = \sqrt{\frac{k_d}{m_d}}, \tag{2.9}$$

ω_1, ω_2 and ω_3 are the natural frequencies when the masses remain in contact. These natural frequencies are obtained by solving the characteristic equation of the system

$$s^6 + \left(\left(1+r_b\right)\omega_b^2 + \omega^2 + \left(1+r_d\right)\omega_d^2\right)s^4 + \left(\omega_b^2\omega^2 + \left(1+r_b+r_d\right)\omega_b^2\omega_d^2 + \omega^2\omega_d^2\right)s^2$$

$$+\omega_b^2\omega^2\omega_d^2 = 0. \tag{2.10}$$

where

$$r_b = \frac{m_b}{m}, \quad r_d = \frac{m_d}{m}, \omega = \sqrt{\frac{k}{m}}, \tag{2.11}$$

The velocity of m_d is obtained by differentiating Eq. (2.8),

$$v_d(t) = r_b\omega_b^2\omega_d^2 v_{b-}\left[\frac{1}{\left(\omega_1^2-\omega_2^2\right)\left(\omega_1^2-\omega_3^2\right)}\cos\omega_1 t - \frac{1}{\left(\omega_1^2-\omega_2^2\right)\left(\omega_2^2-\omega_3^2\right)}\cos\omega_2 t\right.$$

$$\left. + \frac{1}{\left(\omega_1^2-\omega_3^2\right)\left(\omega_2^2-\omega_3^2\right)}\cos\omega_3 t\right]. \tag{2.12}$$

Suppose that m_b looses contact at $t = \pi/\omega_b$ and m_d looses contact after m_b, the velocity of m_d at $t = \pi/\omega_b$ is given by

$$v_d\left(\frac{\pi}{\omega_b}\right) = r_b\omega_b^2\omega_d^2 v_{b-}\left[\frac{1}{\left(\omega_1^2-\omega_2^2\right)\left(\omega_1^2-\omega_3^2\right)}\cos\frac{\pi\omega_1}{\omega_b} - \frac{1}{\left(\omega_1^2-\omega_2^2\right)\left(\omega_2^2-\omega_3^2\right)}\cos\frac{\pi\omega_2}{\omega_b}\right.$$

$$+\frac{1}{\left(\omega_1^2-\omega_3^2\right)\left(\omega_2^2-\omega_3^2\right)}\cos\frac{\pi\omega_3}{\omega_b}\Bigg]. \tag{2.13}$$

The maximum value of the first term in Eq. (2.13) is found when

$$\cos\frac{\pi\omega_1}{\omega_b}=1, \tag{2.14}$$

$$\frac{\omega_1}{\omega_b}=0,2,4,\cdots. \tag{2.15}$$

The maximum value of the second term in Eq.(2.13) is given by

$$\cos\frac{\pi\omega_2}{\omega_b}=-1, \tag{2.16}$$

$$\frac{\omega_2}{\omega_b}=1,3,5,\cdots. \tag{2.17}$$

The maximum value of the third term in Eq.(2.13) is obtained when

$$\cos\frac{\pi\omega_3}{\omega_b}=1, \tag{2.18}$$

$$\frac{\omega_3}{\omega_b}=0,2,4,\cdots. \tag{2.19}$$

Eqs. (2.15), (2.17) and (2.19) indicate that the maximum kinetic energy of m_d can be achieved when the ratio of the natural frequencies to ω_b are integer numbers.

In ideal case, ω_b should be as larger as possible to transfer a large amount of kinetic energy from m_b to m_d. Regarding this condition, the optimum value for the first term in Eq. (13) is achieved when

$$\frac{\omega_1}{\omega_b}=0,$$

$$\omega_1=0. \tag{2.20}$$

Substitution of $\omega_1= 0$ into Eq. (2.11), indicates that the zero value of the characteristic root is obtained when

$$\omega_b^2\omega^2\omega_d^2=0, \ \rightarrow \omega=0. \tag{2.21}$$

For ratios of ω_r/ω_b =1, (r = 1,2,3,$\cdots$), an optimum condition is obtained by substitution of $s^2=-\omega_b^2$ into Eq. (2.11), which yields,

$$\omega_b=\omega_d. \tag{2.22}$$

Equation (2.22) indicates that the optimum condition for transfer of energy is obtained when the contact frequencies are the same. Table 2.1 shows the parameter

values used in the simulation. One value of mass ratio m_b/m and four values of mass ratio m_d/m were used in the simulation. The natural frequency of mass m is fixed at 200π rad/s.

Table 2.1 Simulation parameters for rigid body collision.

Parameter	Value
m_b/m	0.5
m	1.8 kg
m_d/m	0.25, 0.5, 1, 1.5
ω	200π rad/s
v_{b-}	1 m/s

Integration of Eq. (2.1)-(2.3) was carried in MatLab/Simulink by using the fifth-order Dormand-Prince method with variable time steps. Simulation results for the energy transfer with mass ratios m_d/m 0.25, 0.5, 1 and 1.5 are depicted in Fig. 2.3. The solid line is the transfer of energy (E_{d+}/E_{b-}) and the dashed line is the energy absorbed by the main body m (E/E_{b-}). It can be shown that the transfer of energy increases with increasing values of ω_b/ω. The peak transfer of energy and the point of minimum energy absorption are located close to point $\omega_b = \omega_d$ as indicated by Eq. (2.22). The mass ratio m_d/m is the significant factor in determining energy transfer. The minimum energy of main body is obtained when $m_d/m = 1$. In this condition, wherein $\omega_b/\omega = 100$, almost all of the kinetic energy of main body is transferred to the absorber mass as shown in Fig. 2.3(c).

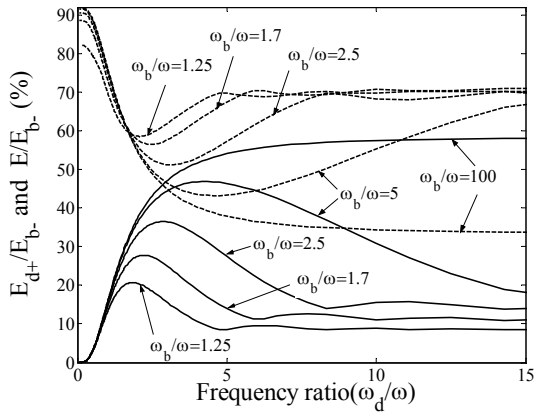

(a) m_b/m=0.5, m_d/m=0.25

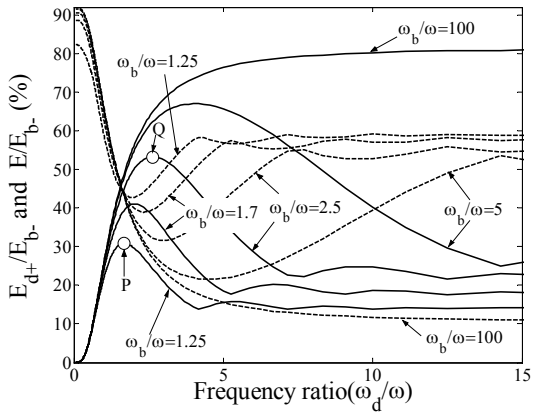

(b) m_b/m=0.5, m_d/m=0.5

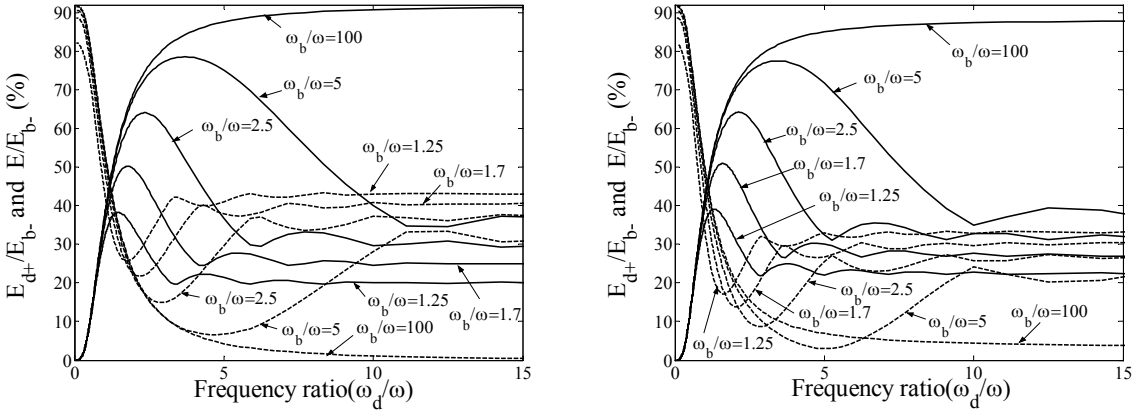

(c) m_b/m=0.5, m_d/m=1 (d) m_b/m=0.5, m_d/m=1.5

Fig. 2.3 Transfer of energy in collision of rigid bodies.
(solid line: E_{d+}/E_{b-}, dashed line : E/E_{b-})

Figure 2.4 and 2.5 show two sets of typical time responses of the system for ω_b/ω = 1.25 and ω_b/ω = 2.5. These responses are obtained for mass ratios m_b/m = 0.5 and m_d/m 0.5. In these figures, force variables f_b, f_d and f_k were normalized by dividing them by $m_b\omega_b v_{b-}$. The velocity and time variables were also normalized by dividing them by v_{b-} and $\pi(m_b/k_b)^{1/2}$, respectively. As one might observe from these figures, the contact force f_b follows a nearly sinusoidal path for half a period after the impact. Figure 2.4 and Fig. 2.5 show that the velocity of m_d has a maximum value when ω_d/ω is located at the peak ratio of E_{d+}/E_{b-} (denoted by point P and Q in Fig. 2.3(b)). When ω_d/ω = 0.1, the velocity of m_d is small compared to the initial velocity of m_b. The reason for this is that the contact force f_d is small so that the transfer of momentum from m to m_d is low. The contact force f_d follows an un-smooth path for ω_d/ω=15. This phenomenon may be caused by multiple collisions.

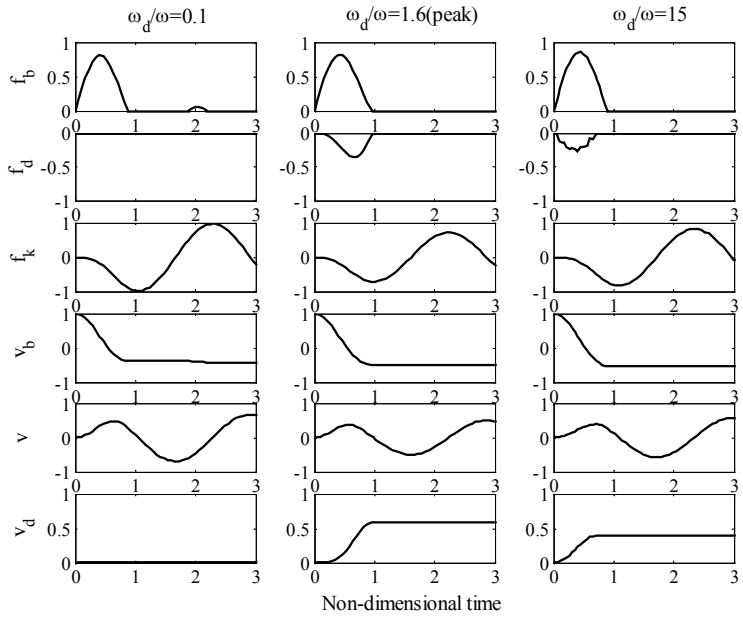

Fig. 2.4 Time history for $\omega_b/\omega = 1.25$.

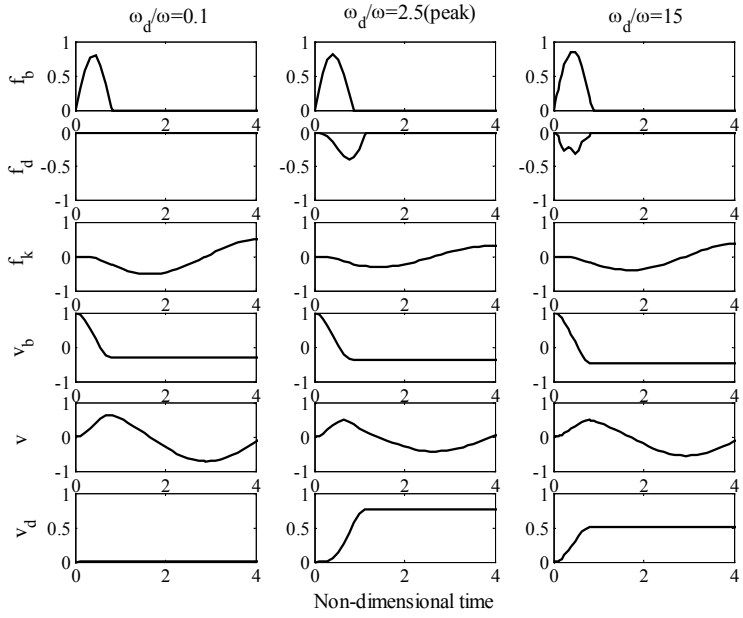

Fig. 2.5 Time history for $\omega_b/\omega = 2.5$.

2.2.2 Solution Using the Coefficient of Restitution

When $\omega_b >> \omega$ and $\omega_d >> \omega$, more energy is stored within the contact spring than in the oscillator spring (Pinnington, 2003). This state can be regarded as a free collision problem(Johnson, 1985; Kane and Levinson, 1985; Kilmister and Reeve, 1966; Lagrange, 1811). For this special case, the conservation of momentum and coefficient of

restitution can be applied to the collision between mass m and both m_b and m_d(Escalona and Mayo, 1999; Chung and Ming, 2003; Smith and Liu, 1992).

By using the conservation of momentum and coefficient of restitution for the first collision between m_b and m, yields

$$m_b v_{b+} + m v_{+} = m_b v_{b-} + m v_{-}, \tag{2.23}$$

$$e_b = \frac{\left(v_{+} - v_{b+}\right)}{\left(v_{b-} - v_{-}\right)}, \tag{2.24}$$

$$J_b = \left(m v_{+} - m v_{-}\right), \tag{2.25}$$

where v_{-} is velocity of m before the first collision, v_{+} is velocity of m after the first collision, e_b is coefficient of restitution and J_b is impulse between m and m_b. Eq. (2.23)-(2.25) can be arranged to give

$$J_b = \frac{m_b m}{m_b + m}\left(1 + e_b\right)\left(v_{b-} - v_{-}\right). \tag{2.26}$$

By using the same procedure for the second collision between m and m_d the following is obtained,

$$m v_{++} + m_d v_{d+} = m v_{+} + m_d v_{d-}, \tag{2.27}$$

$$e_d = \frac{\left(v_{d+} - v_{++}\right)}{\left(v_{+} - v_{d-}\right)}, \tag{2.28}$$

$$J_d = \left(m_d v_{d+} - m_d v_{d-}\right), \tag{2.29}$$

$$J_d = \frac{m m_d}{m + m_d}\left(1 + e_d\right)\left(v_{+} - v_{d-}\right), \tag{2.30}$$

where v_{++} is velocity of m after the second collision, v_{d-} is velocity of m_d before the second collision, e_d is coefficient of restitution and J_d is impulse between m and m_d, respectively. In this case,

$$v_{-} = v_{d-} = 0. \tag{2.31}$$

By using Eqs. (2.23)-(2.24) and Eqs. (2.27)-(2.28), the final velocities of m_b and m_d are given by

$$v_{b+} = \frac{m_b - m e_b}{m_b + m} v_{b-}, \tag{2.32}$$

$$v_{d+} = \frac{\left(1 + e_b\right)\left(1 + e_d\right) m m_b}{\left(m + m_d\right)\left(m_b + m\right)} v_{b-}. \tag{2.33}$$

If $e_b = e_d$=1, the final energy of mass m_b, m_d and m can be expressed as

$$\left(\frac{E_{d+}}{E_{b-}}\right)_{free} = \frac{\frac{1}{2}m_d v_{d+}^{\ 2}}{\frac{1}{2}m_b v_{b-}^2} = \frac{16m^2 m_b m_d}{\left(m+m_d\right)^2\left(m_b+m\right)^2}, \tag{2.34}$$

$$\left(\frac{E_{b+}}{E_{b-}}\right)_{free} = \frac{\frac{1}{2}m_b v_{b+}^{\ 2}}{\frac{1}{2}m_b v_{b-}^2} = \left(\frac{m_b-m}{m_b+m}\right)^2, \tag{2.35}$$

$$\left(\frac{E}{E_{b-}}\right)_{free} = 1-\left(\frac{E_{b+}}{E_{b-}}\right)_{free} - \left(\frac{E_{d+}}{E_{b-}}\right)_{free}. \tag{2.36}$$

Equation (2.35) shows that the reflected energy is a function of m_b and m only. Increasing the mass ratio m_d/m only affects the final energy of mass m and m_d. When the mass ratio m_d/m=1, the final energy of m becomes zero.

Table 2.2 shows the results of final energy, calculated using Eqs. (2.34) ~ (2.36) for m_b/m=0.5 and m_d/m 0.25, 0.5, 1 and 1.5. The results in Table 2.2 agree well with the calculated results based on the contact spring model using Eqs. (2.1)-(2.5), as shown in Fig. 2.3 for $\omega_b/\omega \geq 100$.

Table 2.2 Final Energy given by the coefficient of restitution method.

m_d/m	$\frac{E}{E_{b-}}$	$\frac{E_{b+}}{E_{b-}}$	$\frac{E_{d+}}{E_{b-}}$
0.25	0.23	0.11	0.56
0.5	0.1	0.11	0.79
1	0	0.11	0.89
1.5	0.03	0.11	0.85

2.3 Elastic Rod Collision

Figure 2.6 shows the model of a free one-dimensional elastic rod in collision with an impact source mass m_b. Mass m_d is initially in contact with the rod.

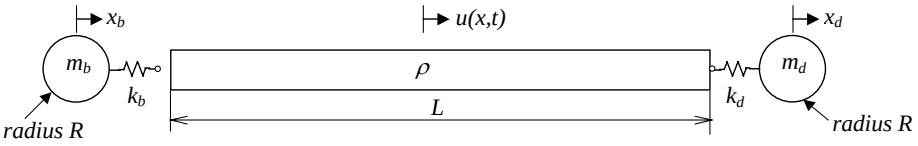

Fig. 2.6 Collision of free elastic rod.

The governing equations of motion are expressed as

$$EA\frac{\partial^2 u}{\partial x^2}-\rho A\frac{\partial^2 u}{\partial t^2}=f_b\delta(x-0)-f_d\delta(x-L), \tag{2.37}$$

$$m_b\ddot{x}_b+f_b=0, \tag{2.38}$$

$$m_d\ddot{x}_d-f_d=0, \tag{2.39}$$

where E is Young modulus, A is the cross section area, δ. is delta function and f_b and f_d are the contact force between rod and both m_b and m_d, respectively. The contact forces are given by

$$f_b=\begin{cases}k_b\{x_b-u(0,t)\}, & for \quad x_b-u(0,t)\geq 0,\\ 0, & for \quad x_b-u(0,t)<0,\end{cases} \tag{2.40}$$

$$f_d=\begin{cases}k_d\{u(L,t)-x_d\}, & for \quad u(L)-x_d\geq 0,\\ 0, & for \quad u(L)-x_d<0.\end{cases} \tag{2.41}$$

Longitudinal vibration of the rod can be given by summation of the normalized eigenfunctions $\psi_r(x)$ as

$$u(x,t)=\sum_{r=0}^{\infty}\psi_r(x)q_r(t), \tag{2.42}$$

where

$$\psi_r=\cos\frac{r\pi x}{L},\quad r=0,\cdots,\infty, \tag{2.43}$$

and q_r is the general coordinate. ψ_0 represents the non-vibrational rigid body transverse motion. By substituting Eq. (2.42) for u and using the orthogonality of the eigenfunctions, the differential equation of motion Eq. (2.37) can be written as[11]

$$\ddot{q}_r+\omega_r^2 q_r=\frac{f_r(t)}{m}, \tag{2.44}$$

where $f_r(t)$ is given by

$$f_r(t)=\int_0^L\left[f_b\delta(x-0)-f_d\delta(x-L)\right]\psi_r(x)dx, \tag{2.45}$$

and where $m=\rho A$ is the mass per unit length, $\omega_r=r\pi c/L$ is the natural frequency and c is the speed of sound for the rod.

Two simulations using a steel rod with differing lengths were conducted to simulate the collision of rigid masses with an elastics rod. The simulation parameters were shown in Table 2.3, where ω_0 - ω_3 are the natural frequencies of the rod.

Table 2.3 Simulation parameters of elastic rod collision.

Parameter	L = 2m	L = 3m
m_b	1 kg	1 kg
$\rho A\, L$	5 kg	7.4 kg
m_d	1 kg	1 kg
A	7.85×10^{-5}m^2	7.85×10^{-5}m^2
v_{b-}	1m/s	1m/s
ω_0	0 rad/s	0 rad/s
ω_1	7.92×10^3 rad/s	5.28×10^3 rad/s
ω_2	1.58×10^4 rad/s	1.06×10^4 rad/s
ω_3	2.38×10^4 rad/s	1.58×10^4 rad/s

Numerical simulation was carried in MatLab/Simulink computational environment by using the fifth-order Dormand-Prince method with variable time steps. Variables ω_b and ω_d were varied within the range $\omega_b \in [6.6 \times 10^3, 4 \times 10^4]$ rad/s and $\omega_d \in [1.6\times10^3, 1.6\times10^5]$ rad/s.

Because the elastic rod is modeled as a continuous component, the system has an infinite number of vibration modes. Each mode contributes to the transfer of energy during the collision. Figure 2.7 shows simulated energy ratios as a function of ω_b/ω_1 and ω_d/ω_1 using the 50 lowest modes for rod lengths of 2 and 3 m. The solid line represents the transfer of energy (E_{d+}/E_{b-}) and the dashed line the energy absorbed by main body m (E/E_{b-}). Similarly to the previous case, the peak energy transfer and minimum absorbed energy are located near the point $\omega_b = \omega_d$. The transfer of energy is increases as ω_b/ω_1 is increased. For $\omega_d/\omega_1 > 5$ the transfer of energy is nearly constant.

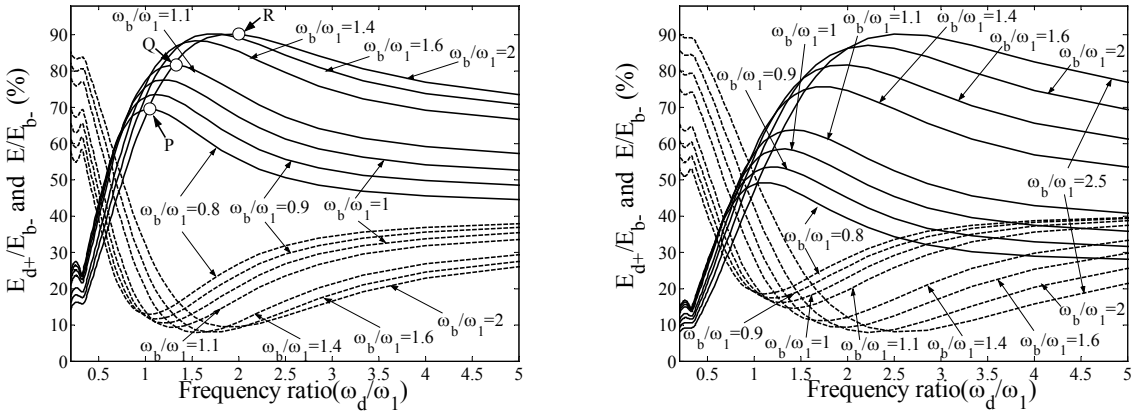

(a) L=2m (a) L=3m

Fig. 2.7 Transfer of energy of the free rod.
(solid line: E_{d+}/E_{b-}, dashed line : E/E_{b-})

It should be pointed out that the transfer of energy in the free elastic rod problem is primarily governed by the elastic modes of the rod. This phenomenon is different from the transfer of energy in the free rigid body case described previously. For example, when the rod is assumed to be rigid, the transfer of energy calculated using Eq. (2.34) for a 2 m rod, yields

$$\frac{E_{d+}}{E_{b-}} = \frac{16m^2 m_b m_d}{\left(m+m_d\right)^2\left(m_b+m\right)^2} = 31\% . \tag{2.46}$$

This result is clearly lower than the resultant energy transfer shown in Fig. 2.7 (a) for the elastic rod. This is because its one-dimensional vibration modes were ignored in the calculation.

Figures 2.8, 2.9 and 2.10 show three sets of typical time responses of the system for ω_b/ω_1 = 0.8, 1.1 and 2. These responses were obtained for L = 2m. In these figures, all variables were normalized according to the previously described criteria. Figure 2.8 shows that the velocity of m_d has a maximum value when ω_d/ω_1 is located at the peak of the E_{d+}/E_{b-} curves (denoted by point P in Fig. 2.7(a)). The contact force f_d has two peaks for ω_d/ω_1= 0.2 because the contact stiffness is small and the contact force is not large enough to make m_d loose contact simultaneously.

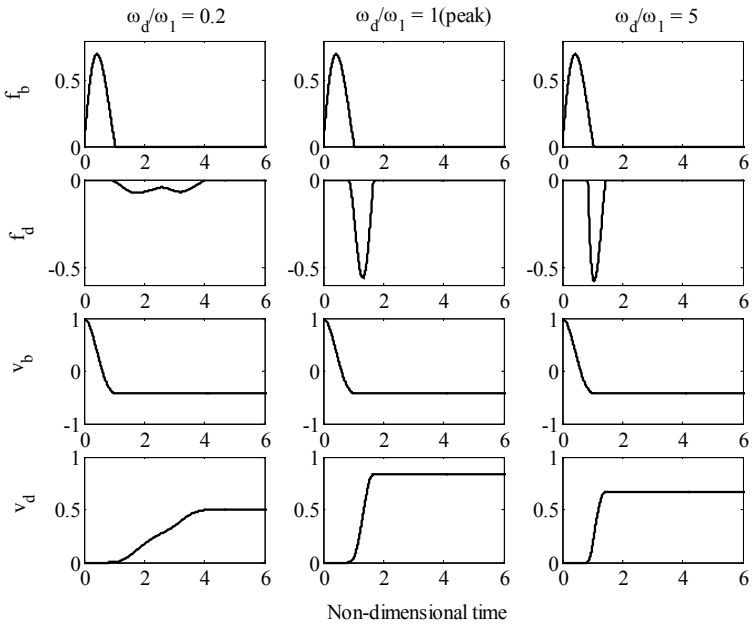

Fig. 2.8 Time history for ω_b/ω_1= 0.8.

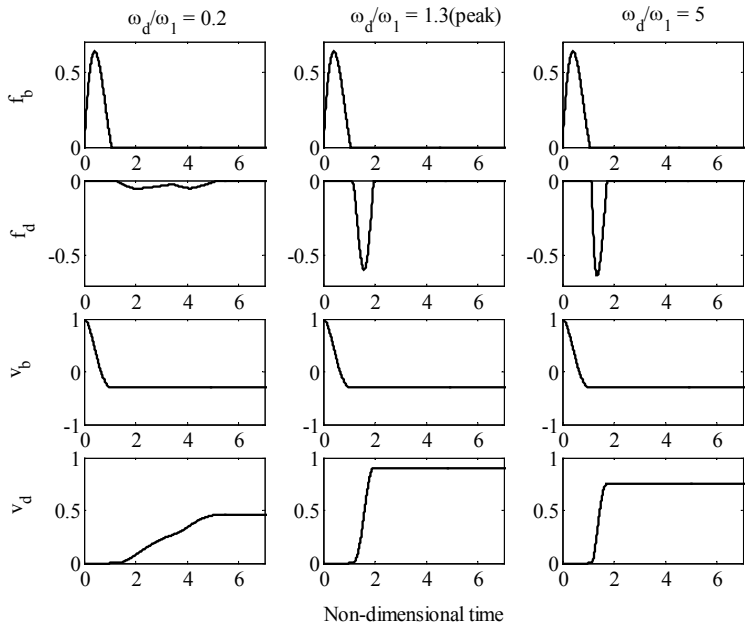

Fig. 2.9 Time history for $\omega_b/\omega_1 = 1.1$.

For small values of ω_b/ω_1 as shown in Fig. 2.8, the reflected energy is almost 42% of the initial kinetic energy of m_b(indicated by final velocity of m_b). In contrast, for large values of of ω_b/ω_1, as shown in Fig. 2.10, the reflected energy is only 7%. In this case, nearly all of the kinetic energy of m_b is transferred to the rod.

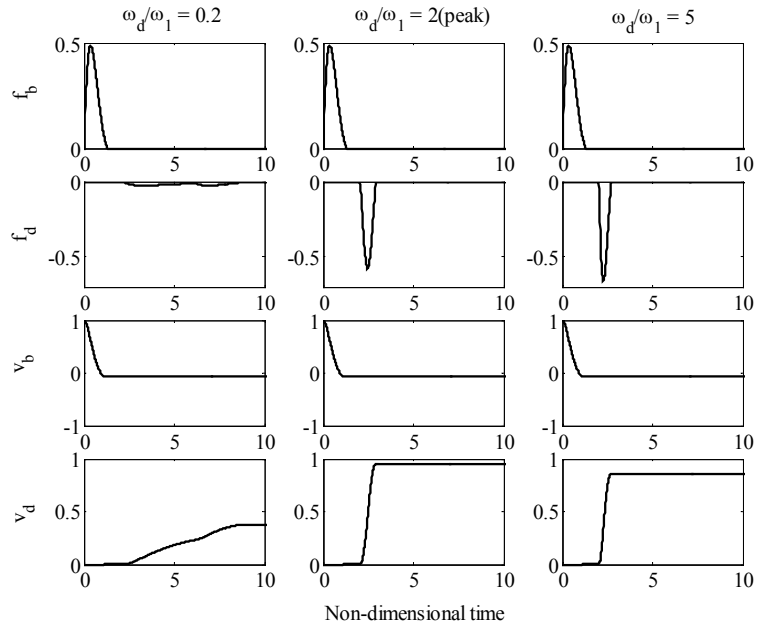

Fig. 2.10 Time history for $\omega_b/\omega_1 = 2$.

2.4 Experiment

2.4.1 Rigid Body Collision

An experimental apparatus consisting of two steel rigid masses and one short rod was used to validate the mathematical simulations. A golf ball was attached to each end of the rigid masses. The rigid masses were hung from a support frame by an aluminum arm (see Fig. 2.11). The impacts were obtained by releasing the first mass from a predetermined height. Table 2.4 shows the experimental parameters defining the rod and rigid masses. With this configuration, it is possible to assume that the elastic modes of vibration can be neglected during impacted because ω_b and ω_d are small compared with the natural frequencies of elastic vibration.

Table 2.4 Experimental parameters for rigid body collision.

Parameter	Value
m_b	0.9 kg
mL	1.8 kg
m_d	0.45, 0.9 kg
h_b	0.15 m
k_b	1×10^6 N/m
k_d	1×10^6 N/m
ω_b	1×10^2 rad/s
ω_d	1×10^3, 1.5×10^3 rad/s

The rod was supported by leaf springs on two supporting points to avoid yawing motion. The natural frequency of the supported rod was varied by altering the spring length and thickness. Table 2.5 shows the natural frequencies of the supported rod.

Table 2.5 Natural frequency of the supported rod.

No	Length of leaf spring (mm)	Thickness of leaf spring (mm)	k (N/m)	ω (rad/s)
1	32.15	4	6.1×10^6	2835.3
2	53.35	4	2.2×10^6	1562.9
3	31.30	1	1.8×10^5	477.5
4	42.85	1	7.3×10^4	318.9
5	97.50	1	8.9×10^3	95.5

Kinematics data for m_d was acquired using a high speed camera with a frame rate of

250 frames/sec. Video images of the experimental results were post-processed to determine the maximum height of m_d after the collision. The transfer of energy from m_b to m_d was calculated by comparing the maximum height of m_d after collision to the height of m_b before collision.

$$\frac{E_{d+}}{E_{b-}} = \frac{h_{d\max}}{h_{b-}} . \tag{2.47}$$

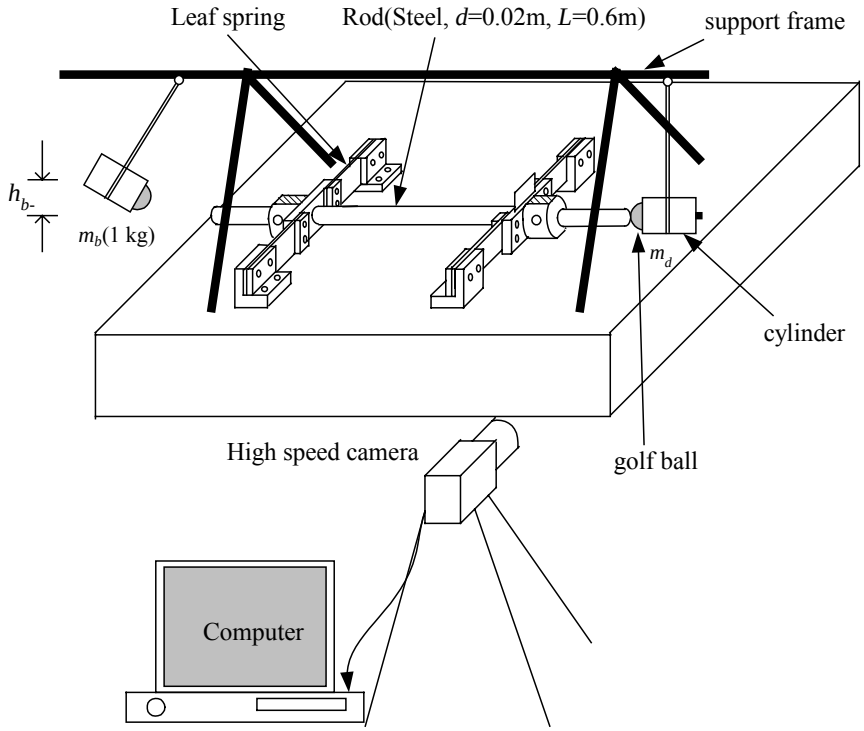

Fig. 2.11 Experimental apparatus for collision of rigid body.

Figure 2.12 shows the influence of leaf spring size on the acceleration of second cylinder for mass ratio $\mu = m_d/m_r = 0.25$. T in Figure 2.12 denotes the contact time as obtained experimentally. As shown in Figure 2.12, the acceleration on the end surface of the second cylinder resembled a single pulse and the amplitude of the subsequent periodic waves was reduced.

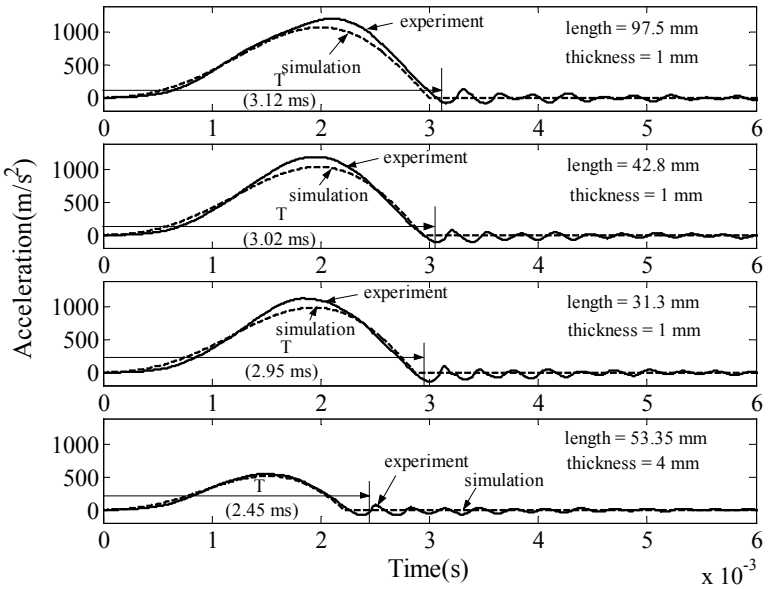

Figure 2.12 Influence of leaf spring size on cylinder acceleration for $\mu = 0.25$.

The influence of leaf spring size on the acceleration of second cylinder for mass ratio $\mu = 0.75$ is depicted in Fig. 2.13. Comparison the contact time in Fig. 2.13 with the result in Fig. 2.12 shows that the contact ratio increases when the mass ratio increases. On the other hand, the maximum peak of acceleration decreases when the mass ratio increases.

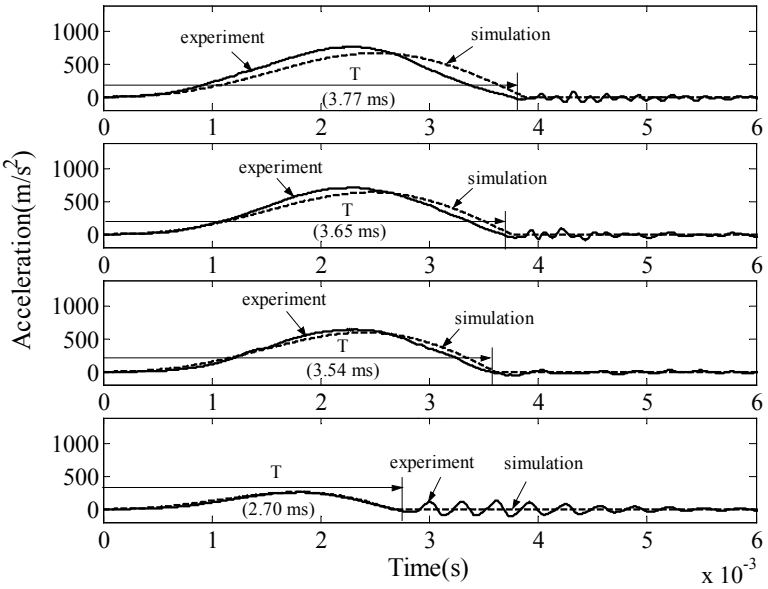

Figure 2.13 Influence of leaf spring size on cylinder acceleration for $\mu = 0.75$.

Figure 2.14 shows the influence of leaf spring size on the rod displacement. As shown in Figure 2.14, identical wave pattern was periodically repeated when the leaf spring has low stiffness, and the period corresponds to that of the rigid body mode of the rod. However, for leaf spring with high stiffness the waveform of displacement resembled a single pulse and the amplitude of the subsequent periodic waves corresponding to the rigid body mode was lower than the first single pulse.

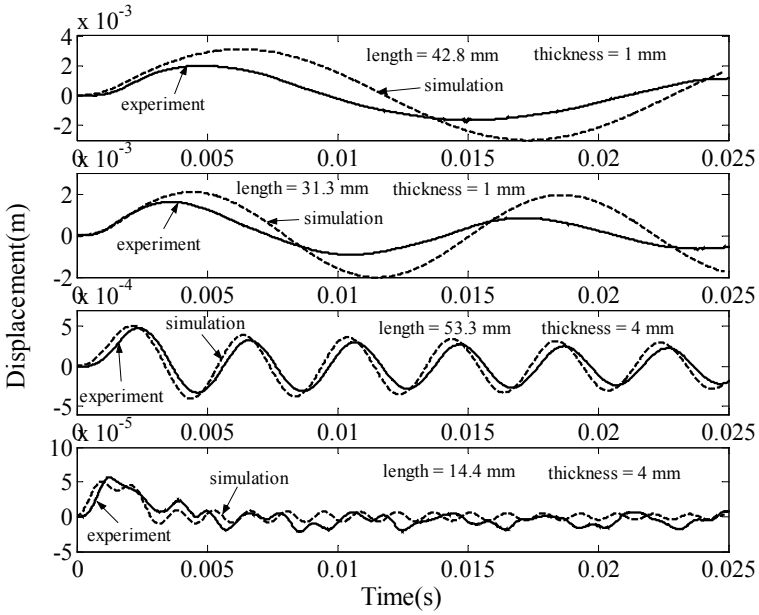

Figure 2.14 Influence of leaf spring size on rod displacement for $\mu = 0.25$.

Figure 2.15 shows the simulation and experimental result of the energy transfer, E_{d+}/E_{b-}. It should be pointed out that the results shown in Fig. 2.15 are for the special case, depicted in Fig. 2.3, wherein $k_b = k_d$. The transfer of energy that was obtained in the experimental was smaller than that calculated in the simulation. The difference is mainly due to energy losses from contact damping.

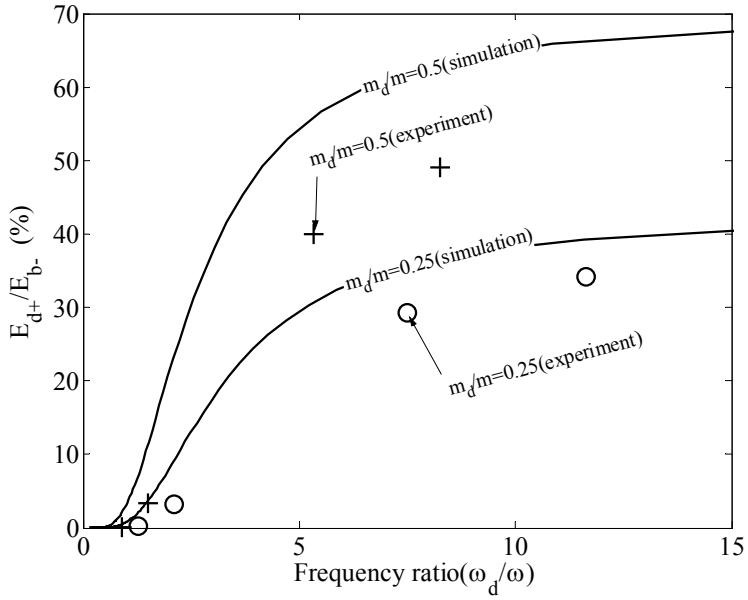

Fig. 2.15 Transfer of energy of rigid body.

2.4.2 Elastic Rod Collision

Figure 2.16 shows the experimental apparatus for the elastic rod problem. A long rod with 2 m lengths and 0.02 m diameters was hung using two wires. Two rigid masses m_b and m_d were positioned on each side of the rod. The initial height of m_b from its equilibrium position was 0.05 m, while m_d was initially contacting the rod. The rigid mode natural frequency of the rod is 6.2 rad/s. This frequency is small compared to the natural frequency of its first elastic mode and the contact frequencies ω_b and ω_d, which allows the rod to be assumed to be in a freely supported condition.

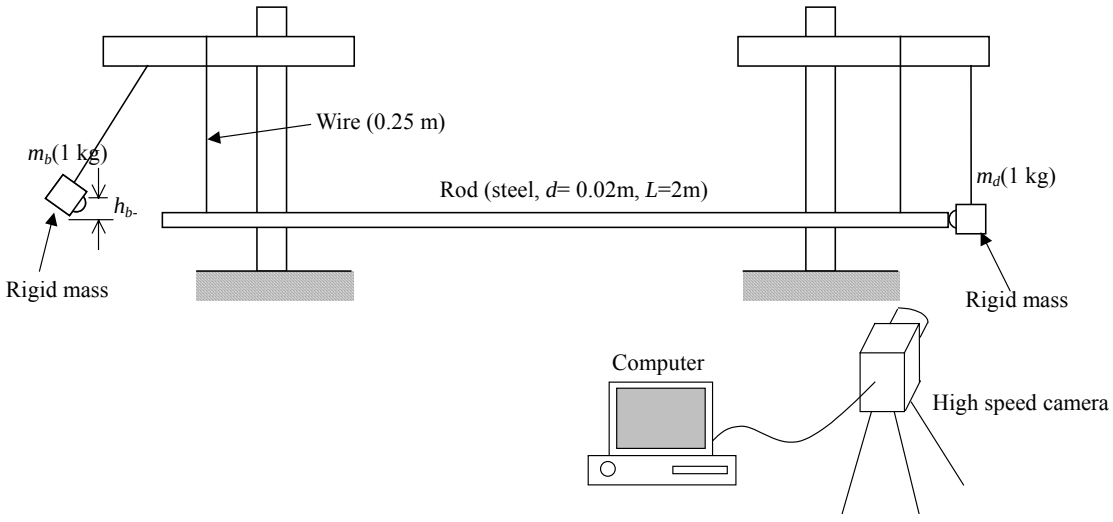

Fig. 2.16 Experimental setup for collision of elastic rod.

Variation of frequency ratio was obtained by using different contact stiffness. The contact stiffnesses between the rod and both m_b and m_d were determined by collisions with a rigid wall using the experiment set-up shown in Fig. 2.17. A mass is shown colliding with a rigid wall with initial velocity v_{b-}. The response of the mass during the collision was measured using an accelerometer. The contact duration was measured by using an electrical contact switch. The contact stiffness is obtained by reconciling the simulation results and the experimental data. Table 2.6 shows the calculated contact stiffness for four kinds of contact surfaces.

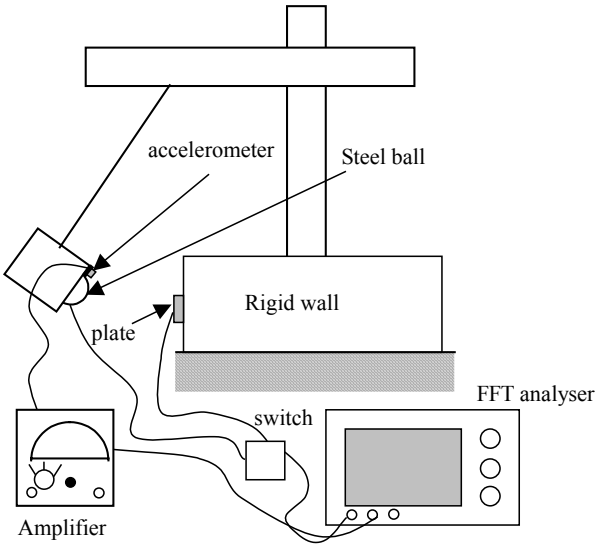

Fig. 2.17 Experimental setup for determining the contact stiffness.

Table 2.6 Contact stiffness and contact frequency.

Material of contact type	Contact stiffness (N/m)	Contact frequency(rad/s)
Steel ball(R = 12.5mm)-steel plate	1.5×10^8	12000
Steel ball(R = 12.5mm)-brass plate	8×10^7	8900
Steel ball(R = 12.5mm)-aluminum plate	6×10^7	7700
Steel ball(R = 12.5mm)-plastic plate	6×10^6	2400

The transfer of energy from m_b to m_d is shown in Fig. 2.18. Figure 2.18 shows that the simulation results and the experimental data are in good agreement. The differences in magnitude between simulation and experimental results are mainly due to contact damping.

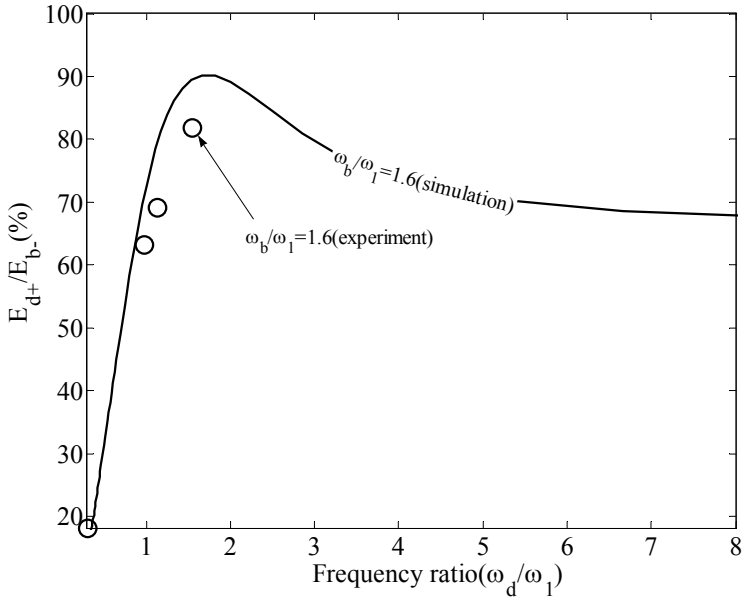

Fig. 2.18 Elastic rod energy transfer.

2.5 Summary

The formulation and analysis of collision problems consisting of two rigid masses with a supported rigid rod and a free elastic rod has been presented. Although these are idealized systems, they can be used to simply model systems involving momentum exchange impact dampers.

For collision between rigid bodies, the maximum transfer of energy is obtained when the natural frequency of the system in the contact state is the same as contact frequency between main body and both the impact mass (ω_b) and the absorber mass (ω_d). In this collision case, the mass ratio is significant in determining the transfer of energy. The amount of energy transfer increases as the contact frequency ω_b increases. When the frequency ratio between ω_b and natural frequency of main body greater than 100, the collision can be regarded as a free collision problem and the transfer of energy can be calculated using energy and momentum conservation.

For collision problems involving a free elastic rod, the maximum transfer of energy is obtained when the value of ω_b is close to that of ω_d. The transfer of energy is primarily governed by its elastic modes of vibration. In this case, changing the mass ratio does not significantly influence the energy transfer.

Chapter 3
REDUCING FLOOR IMPACT VIBRATION AND SOUND USING A MOMENTUM EXCHANGE IMPACT DAMPER

3.1 Introduction

Floor vibration problems are common in many types of industrial building and housing structures. These vibrations can result from many sources (e.g., reciprocating machinery, explosions, and human activity). The human activities such as walking, dancing, jumping, etc have been reported as the most common problems. The forces resulting from these activities are particularly problem because they cannot be easily isolated from the structure and they occur frequently.

Many researches have been conducted to control floor vibrations. Early studies focused the research on the tuned mass dampers (TMDs). Allen and Pernica used TMDs consisting of wooden planks with weights on top for the reduction of annoying vibrations due to human walking (Allen and Pernica, 1984). Setareh and Hanson used TMDs to control the floor vibrations due to dancing in auditorium floor (Setareh and Hanson, 1992). Webster and Vaicajtis used TMDs to control the annoying vibrations of a long-span cantilevered composite floor system due to human movements (Webster and Vaicajtis, 1992).

Recent years, research efforts on active control are increasingly used for reducing floor vibration. Hanagan and Murray used active control to reduce vibration level of floors (Hanagan and Murray, 1994, 1997). Even though active control has better performance than passive control, they have several disadvantages, such as needs for actuator, high operational costs, and high power requirements.

In this work, a momentum exchange impact damper is used to control floor shock vibrations. The performance of this control method in reducing the floor impact vibration and sound was shown analytically and experimentally.

3.2 Flooring System with Impact Damper

An example flooring system consisting of floor (acrylic plate, $0.4 \times 0.32 \times 0.005$ m, m_f = 0.75 kg), support frame (steel), slab (concrete, $0.66 \times 0.57 \times 0.03$ m) and wooden box ($0.58 \times 0.47 \times 0.1$ m) for the room bellow the slab was analyzed (Fig. 3.1). The system has a novel impact damper placed between floor and a supporting slab. The impact damper is positioned in the center of the slab at O_s. The impact damper consists of a mass supported by spring and air damper (k_d = 507 N/m , c_d = 40 Ns/m). The

damper was designed to have lower damping coefficient for forward motion than that for the return motion. The purpose of this technique is to allow fast movement during the moment at which the impact takes place. A steel ball (d = 0.005 m) is glued to the impact damper mass. The steel ball contacts the floor at point O_f which is located at the center of the floor. When the floor has an impact load, it will collide with the damper resulting in exchange of momentum between floor and damper.

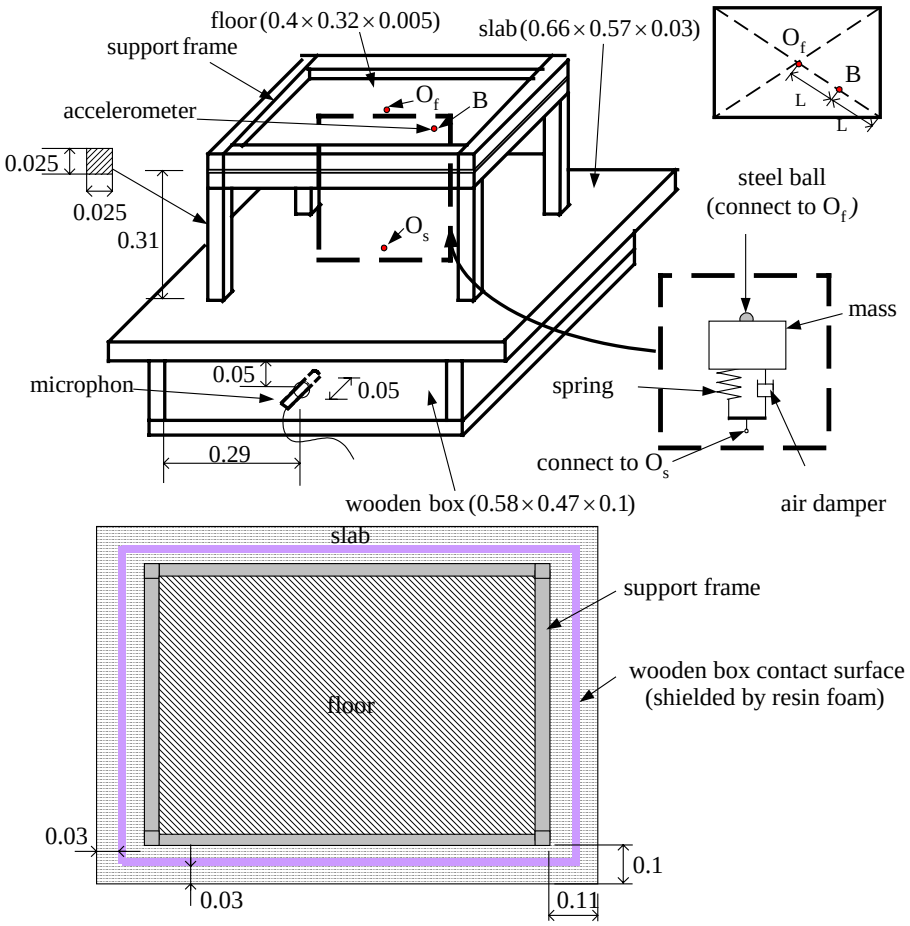

Fig. 3.1 Experimental apparatus of the flooring system with impact damper.

The impact force is generated by dropping a ball (tennis ball, m_b = 0.054 kg and acrylic ball m_b = 0.045 kg) from the height of 0.23 m onto point O_f. The contact surface between wooden box and the slab was shielded by resin foam. This foam was used to block the transmission wave via the gap between slab and wooden box.

3.3 Theoretical Model and Identification

Figure 3.2 shows the model of flooring system with momentum exchange impact damper. The governing equations for the structure consist of floor, support frame, slab

and distributed linear spring are solved using Finite Element Method (FEM)(Zhong, 1993). Uniformly distributed linear springs are used to express the stiffness of resin foam located on the top contact surface of wooden box. Four-node quadrilateral plate elements were used to model both the floor and slab system (see Appendix). The support frame is modeled using three dimensional frame elements(see Appendix).

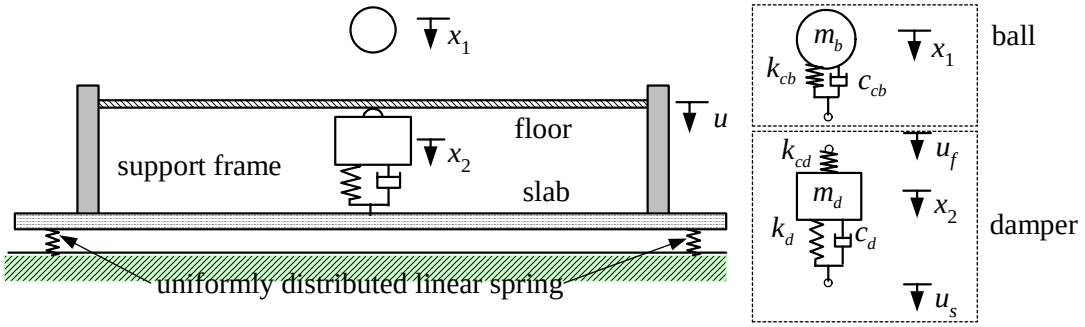

Fig. 3.2 Model of flooring system with impact damper.

The equations of motion for the structure, ball, and impact damper are written as

$$\mathbf{M}\ddot{\mathbf{u}} + \mathbf{C}\dot{\mathbf{u}} + \mathbf{K}\mathbf{u} = \mathbf{B}_{\mathbf{fb}} f_{fb} - \mathbf{B}_{\mathbf{fd}} f_{fd} + \mathbf{B}_{\mathbf{sd}} f_{sd}, \tag{3.1}$$

$$m_b \ddot{x}_1 + f_{fb} = 0, \tag{3.2}$$

$$m_d \ddot{x}_2 + f_{sd} - f_{fd} = 0, \tag{3.3}$$

where matrix **M**, **C** and **K** are the structure mass matrix, damping matrix and stiffness matrix, respectively, while f_{fb}, f_{fd}, f_{sd}, m_b and m_d are the contact force between floor and ball, contact force between floor and impact damper, transmitted force from impact damper to slab, mass of ball and mass of impact damper, respectively. Vector **u**, x_1 and x_2 are displacement vector of the structure, displacement of ball and displacement of impact damper, respectively.

$\mathbf{B}_{\mathbf{fb}}$, $\mathbf{B}_{\mathbf{fd}}$ and $\mathbf{B}_{\mathbf{sd}}$ are vectors that depend on the position of external forces. These vectors can be expressed as,

$$\mathbf{B}_{\mathbf{fb}} = \left\{ \delta_{e1,1} \quad \delta_{e1,2} \cdots \delta_{e1,j} \cdots \quad \delta_{e1,NDOF} \right\}^{\mathrm{T}}, \tag{3.4}$$

$$\mathbf{B}_{\mathbf{fd}} = \left\{ \delta_{e2,1} \quad \delta_{e2,2} \cdots \delta_{e2,j} \cdots \quad \delta_{e2,NDOF} \right\}^{\mathrm{T}}, \tag{3.5}$$

$$\mathbf{B}_{\mathbf{sd}} = \left\{ \delta_{e3,1} \quad \delta_{e3,2} \cdots \delta_{e3,j} \cdots \quad \delta_{e3,NDOF} \right\}^{\mathrm{T}}, \tag{3.6}$$

where, $e1$, $e2$ and $e3$ denote the position of external forces f_{fb}, f_{fd} and f_{sd}, respectively,

while *NDOF* is the number of degree of freedom. $\delta_{i,j}$ is delta function which can be expressed as

$$\delta_{i,j} = \begin{cases} 1, & i = j \\ 0, & i \neq j \end{cases}. \tag{3.7}$$

Contact force between floor and ball was modeled using nonlinear spring and nonlinear dashpot (Hongo, Sato and Iwata, 1999). Thus, the contact force can be expressed as

$$f_{fb} = \begin{cases} k_{cb}\left(x_1 - u_f\right)^{3/2} + c_{cb}\left|x_1 - u_f\right|^{1/2}\left(\dot{x}_1 - \dot{u}_f\right), & \left(x_1 - u_f\right) \geq 0 \\ 0, & \left(x_1 - u_f\right) < 0 \end{cases}, \tag{3.8}$$

where k_{cb} and c_{cb} are contact stiffness and contact damping coefficient between ball and floor, respectively, while u_f is displacement of floor at point O_f.

Note that when the ball is in contact with the floor, the contact force affects the equation of motion and for out of contact case the equation of motion is not affected by contact force.

The transmitted force from impact damper to the slab can be expressed as

$$f_{sd} = c_d(\dot{x}_2 - \dot{u}_s) + k_d(x_2 - u_s), \tag{3.9}$$

where k_d and c_d are the stiffness and damping coefficient of impact damper, respectively, while variable u_s is displacement of slab at point O_s.

The damping coefficient of impact damper for forward motion is very small and leads to

$$c_d = 0 \quad if \quad \dot{x}_2 - \dot{u}_s > 0\ . \tag{3.10}$$

The contact force between floor and impact damper was modeled using Hertz contact theory (Love, 1944)

$$f_{fd} = \begin{cases} k_{cd}\left(u_f - x_2\right)^{3/2}, & \left(u_f - x_2\right) \geq 0 \\ 0, & \left(u_f - x_2\right) < 0 \end{cases}, \tag{3.11}$$

where k_{cd} is contact stiffness between impact damper and floor.

Equation (3.1) can be written in modal coordinates giving

$$\ddot{q}_i + 2\zeta_i\omega_i\dot{q}_i + \omega_i^2 q_i = \boldsymbol{\psi}_i\left[\mathbf{B_{fb}}\, f_{fb} - \mathbf{B_{fd}}\, f_{fd} + \mathbf{B_{sd}}\, f_{sd}\right] \ , \mathrm{i} = 1,2,\cdots,\infty, \tag{3.12}$$

where q_i, ζ_i, ω_i, and $\boldsymbol{\psi}_i$ are the modal displacement, damping ratio, natural frequency and mass normalized eigenvector for i^{th} mode, respectively.

The parameters k_{cb} and c_{cb} were determined by reconciling the simulation and the experimental results of contact force time response as shown in Table 3.1. The experimental results were obtained by dropping a ball from different initial heights on a

small acrylic plate supported by a force sensor located in the center of the plate as shown in Fig. 3.3(a). Figure 3.3 (b) shows a comparison between the experimental and simulation result of tennis ball for h_0 = 0.15 m. It can be shown that there are good agreement between simulation and experimental result

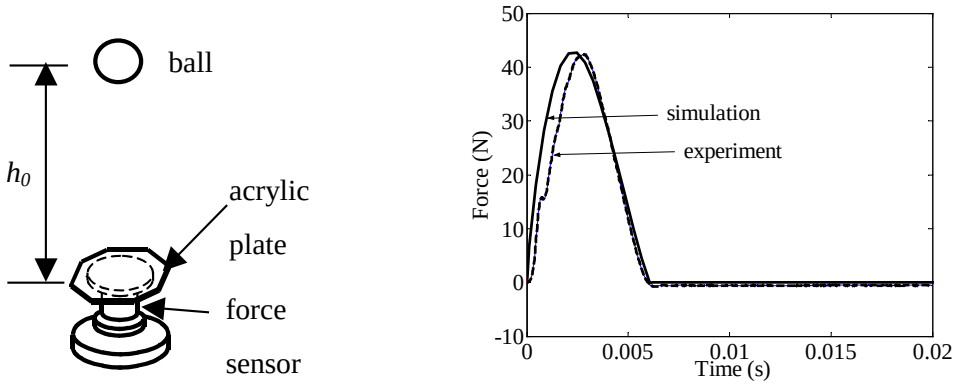

(a) (b)

Fig. 3.3 Determination of k_{cb} and c_{cb}.

Table 3.1 Variation of k_{cb} and c_{cb}.

h_0 (m)	Tennis ball		Acrylic ball	
	k_{cb} (N/m$^{3/2}$)	c_{cb} (Ns/m$^{3/2}$)	k_{cb} (N/m$^{3/2}$)	c_{cb} (Ns/m$^{3/2}$)
0.15	2.1×10^5	160	3.3×10^7	500
0.2	3.1×10^5	160	3.3×10^7	500
0.25	4.1×10^5	160	3.3×10^7	500

Figure 3.4 (a) ~ 3.4 (f) shows several low order mode shapes of the structure without damper obtained by FEM analysis. There are five important modes that play an important role for the center point response of the floor. The 4th mode, occurring at a 19.9 Hz frequency, is the first one. This mode is relating to rigid body motion of floor and slab in vertical direction. The other important modes are the 8th, 13th, 15th, and 18th corresponding to frequencies 151.1, 274.4, 347.1, and 448.3 Hz, respectively.

Figure 3.5 (a) and (b) show the comparison of Frequency Response Function (FRF) obtained from the simulation and experimental data. The experimental FRF was obtained by dividing the measured data of acceleration with input data of force in impulse test using impact hammer. Figure 3.5 (a) shows the results for the input point O_s and output point O_s. There are three dominant modes with frequencies about 19.9, 274.4, and 347.1 Hz. These frequencies relate to the 4th, 13th, and 15th modes,

respectively. Figure 3.5 (b) shows the frequency response function for the input point B and output point B. It can be shown that the simulation model is good enough in expressing the dynamic characteristic of the structure. Based on these responses, seven damping ratios were identified: ζ_4 = 0.06, ζ_8 = 0.018, ζ_{12} = 0.019, ζ_{13} = 0.010, ζ_{14} = 0.022, ζ_{15} = 0.01, and ζ_{18} = 0.019.

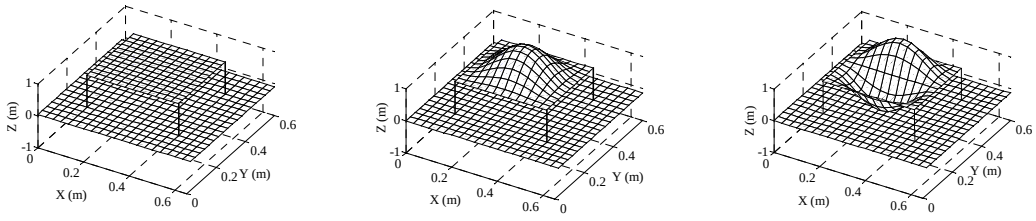

(a) f_4=19.9 Hz (b) f_8=151.1 Hz (c) f_{12}=264.1 Hz

(d) f_{13}=274.4 Hz (e) f_{15}=347.1 Hz (f) f_{18}=448.3 Hz

Fig. 3.4 Floor, support frame and slab mode shape.

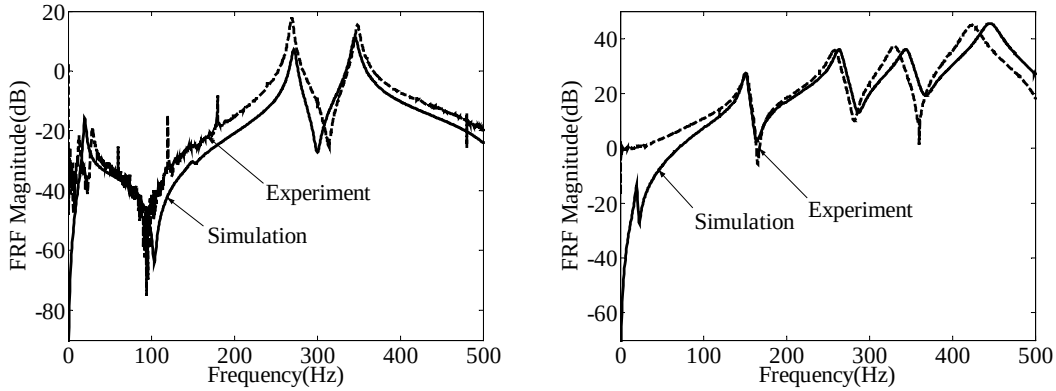

(a) input O_s, output O_s (b) input B, output B

Fig. 3.5 Frequency responses of floor and slab system.

3.4 Sound Pressure Calculation

The transmitted forces from support frame and impact damper to the slab induce the vibration of the slab. According to the acoustic theory, the variation of velocity potential cause propagation of compressible wave inside the room below the slab as shown in Fig. 3.6. The wave equation governing the propagation of small disturbance through a

homogeneous and compressible fluid flow may be written in rectangular Cartesian coordinate as (Craggi, 1986)

$$\frac{\partial^2 \phi}{\partial t^2} = \left(\frac{c}{1 + j\beta} \right)^2 \left(\frac{\partial^2 \phi}{\partial x^2} + \frac{\partial^2 \phi}{\partial y^2} + \frac{\partial^2 \phi}{\partial z^2} \right), \tag{3.13}$$

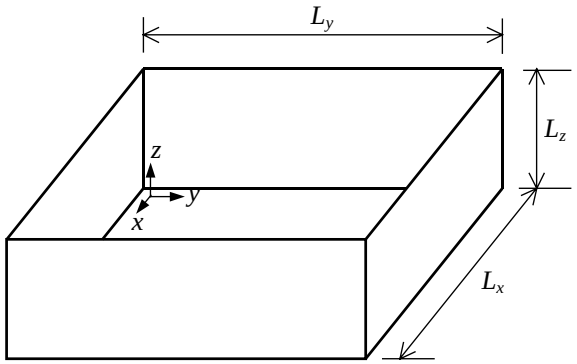

Fig. 3.6 The room bellow the slab.

where β, ϕ, and c describe the acoustic damping factor, velocity potential, and sound speed, respectively. It should be noted that the complex term of damping factor $j\beta$ was including in the wave equation to express the energy losses because of air reflection on the wall and air dispersion. The velocity potential ϕ is combination of several acoustic modes. Hence, it can be expressed as

$$\phi = \sum_n \Phi_n (x, y, z) e^{j\omega_n t}, \tag{3.14}$$

where ω_n is frequency. Φ_n in Eq. (3.14) can be expressed as multiplication of three partial functions $X_n(x)$, $Y_n(y)$, $Z_n(z)$ resulted

$$\phi = \sum_n X_n (x) Y_n (y) Z_n (z) e^{j\omega_n t}. \tag{3.15}$$

By considering the nth acoustic mode and introducing the velocity potential in Eq. (3.15) into wave equation in Eq. (3.13) yields

$$\frac{1}{X_n} \frac{d^2 X_n}{dx^2} + \frac{1}{Y_n} \frac{d^2 Y_n}{dy^2} + \frac{1}{Z_n} \frac{d^2 Z_n}{dz^2} + \frac{\omega_n^2 (1 + j\beta_n)^2}{c^2} = 0, \tag{3.16}$$

$$\mu_{x,n}^2 + \mu_{y,n}^2 + \mu_{z,n}^2 = \frac{\omega_n^2 (1 + j\beta_n)^2}{c^2}, \tag{3.17}$$

where

$$\frac{d^2X_n}{dx^2} + \mu_{x,n}^2 X_n = 0, \tag{3.18}$$

$$\frac{d^2Y_n}{dy^2} + \mu_{y,n}^2 Y_n = 0, \tag{3.19}$$

$$\frac{d^2Z_n}{dz^2} + \mu_{z,n}^2 Z_n = 0. \tag{3.20}$$

Solution of Eqs. (3.18) ~ (3.20) is determined in the form

$$X_n = B_{1,n}\cos\mu_{x,n}x + B_{2,n}\sin\mu_{x,n}x, \tag{3.21}$$

$$Y_n = C_{1,n}\cos\mu_{y,n}y + C_{2,n}\sin\mu_{y,n}y, \tag{3.22}$$

$$Z_n = D_{1,n}\cos\mu_{z,n}z + D_{2,n}\sin\mu_{z,n}z. \tag{3.23}$$

The constants $B_{1,n}$, $B_{2,n}$, $C_{1,n}$, $C_{2,n}$, $D_{1,n}$, $D_{2,n}$ are determined by satisfying boundary conditions. The velocity field inside the room is relating to gradient of velocity potential as expressed in Eq. (3.24)

$$v(x,y,z,t) = -grad\,\phi = \left(-\frac{\partial\phi}{\partial x}, -\frac{\partial\phi}{\partial y}, -\frac{\partial\phi}{\partial z}\right). \tag{3.24}$$

Application of boundary conditions of rectangular room as shown in Fig. 3.6 leads to

$$\frac{\partial\phi}{\partial x} = 0 \quad \text{for} \quad x = 0,\ L_x, \tag{3.25}$$

$$\frac{\partial\phi}{\partial y} = 0 \quad \text{for} \quad y = 0,\ L_y, \tag{3.26}$$

$$\frac{\partial\phi}{\partial z} = 0 \quad \text{for} \quad z = 0, \tag{3.27}$$

$$-\left.\frac{\partial\phi}{\partial z}\right|_{z=Lz} = v_s(x,y,t), \tag{3.28}$$

where v_s is the normal velocity of the slab. The slab normal velocity can be expressed as

$$v_s(x,y,t) = \sum_{i=1}^{\infty} \boldsymbol{\psi}_{s,i}(x,y)\,\dot{q}_{s,i}(t), \tag{3.29}$$

where $\boldsymbol{\psi}_{s,i}(x,y)$, $\dot{q}_{s,i}(t)$ are eigenvector and modal velocity of the slab, respectively.

Application of boundary conditions Eqs. (3.25) ~ (3.28) into Eqs. (3.21) ~ (3.23) yields

$$\Phi_n = \sum_{l=0}^{\infty}\sum_{m=0}^{\infty} A_{n(l,m)}\cos\frac{l\pi x}{L_x}\cos\frac{m\pi y}{L_y}\cos\mu_{n(l,m)}z, \tag{3.30}$$

where *l,m* are nonnegative integer. Substitution of Eq. (3.30) into Eq. (3.14) and applying the result into Eq. (3.28) leads to

$$\sum_{n}\sum_{l=0}^{\infty}\sum_{m=0}^{\infty} A_{n,(l,m)}\mu_{n,(l,m)}\cos\frac{l\pi x}{L_x}\cos\frac{m\pi y}{L_y}\sin\left\{\mu_{n,(l,m)}L_z\right\}e^{j\omega_n t} = v_s\left(x,y,z,t\right) \quad (3.31)$$

To obtain $A_{n,(l,m)}$, the summation term in equation in Eq. (3.31) should be simplified by introducing the inverse Fourier transform procedure

$$v_s\left(x,y,z,t_p\right) = \frac{2}{N}\sum_{q=0}^{N/2-1} V_s\left[x,y,\omega_q\right]e^{j\omega_q t_p}\ , \quad (3.32)$$

where V_s, N, t_p and ω_q are Fourier transform of v_s, the number of Fourier point, discrete time and discrete frequency in Fourier transform, respectively. The value of t_p and ω_q are determined in the form

$$t_p = pT_s\,, \quad (3.33)$$

$$\omega_q = \frac{2\pi q}{NT_s}, \quad (3.34)$$

where q = 0,1,2,…,N/2-1, p = 0,1,2,…,N-1 and T_s is sampling time.

Substitution of the result in Eq. (3.32) into Eq. (3.31) and by assuming the acoustic mode n is equal to q yields

$$\sum_{l=0}^{\infty}\sum_{m=0}^{\infty} A_{q,(l,m)}\mu_{q,(l,m)}\cos\frac{l\pi x}{L_x}\cos\frac{m\pi y}{L_y}\sin\left\{\mu_{q,(l,m)}L_z\right\} = \frac{2}{N}V_s\left(x,y,\omega_q\right). \quad (3.35)$$

It should be noted that the Fourier transform of $v_s(x,y,t_p)$ can be expressed as

$$V_s\left(x,y,\omega_q\right) = \sum_{p=0}^{N-1} v_s\left(x,y,t_p\right)e^{-j\omega_q t_p}. \quad (3.36)$$

Then, the expression in Eq. (3.29) and Eq. (3.36) is substituted into Eq. (3.35). Next, solution of $A_{q,(l,m)}$ is written in the form

$$A_{q,(l,m)} = \frac{\dfrac{2}{N}\displaystyle\sum_{i=1}^{\infty}\left[\sum_{p=0}^{N-1}\left\{\dot{q}_{s,i}\left(t_p\right)e^{-j\omega_q t_p}\iint_S \cos\frac{l\pi x}{L_x}\cos\frac{m\pi y}{L_y}\boldsymbol{\psi}_{s,i}\left(x,y\right)dS\right\}\right]}{\mu_{q,(l,m)}\sin\left\{\mu_{q,(l,m)}L_z\right\}\displaystyle\iint_S \cos^2\frac{l\pi x}{L_x}\cos^2\frac{m\pi y}{L_y}dS}, \quad (3.37)$$

and

$$\mu_{q,(l,m)} = \sqrt{\left\{\frac{\omega_q\left(1+j\beta_q\right)}{c}\right\}^2 - \left(\frac{l\pi}{L_x}\right)^2 - \left(\frac{m\pi}{L_y}\right)^2}\ , \quad (3.38)$$

where β_q and ω_q are acoustic damping factor, and acoustic natural frequency of the

room, respectively. Integral operator $\iint_S \cdots dS$ in Eq. (3.37) is used to express the surface integral.

The velocity potential can be calculated as

$$\phi\left(x,y,z,t_p\right) = \sum_{q=0}^{N/2-1}\sum_{l=0}^{\infty}\sum_{m=0}^{\infty} A_{q,(l,m)} \cos\frac{l\pi x}{L_x}\cos\frac{m\pi y}{L_y}\cos\mu_{q,(l,m)} z e^{j\omega_q t_p} . \quad (3.39)$$

Finally, the sound pressure generated in the room bellow the slab can be expressed as

$$p = \rho_a \frac{\partial\phi}{\partial t}, \quad (3.40)$$

$$p\left(x,y,z,t_p\right) = \rho_a \sum_{q=0}^{N/2-1}\sum_{l=0}^{\infty}\sum_{m=0}^{\infty} j\omega_q A_{q,(l,m)} \cos\frac{l\pi x}{L_x}\cos\frac{m\pi y}{L_y}\cos\mu_{q,(l,m)} z e^{j\omega_q t_p} , \quad (3.41)$$

where ρ_a is density of air.

3.5 Simulation Result

The initial ball dropping height was 0.23 m. First, the low impact load was applied to the simulation system. The low impact load was realized by dropping a tennis ball (m_b = 0.054 kg) into the acrylic plate. The parameters k_{cb} and c_{cb} for tennis ball were interpolated from Table 3.1 giving values of 3.7×10^5 N/m$^{3/2}$ and 150 Ns/m$^{3/2}$, respectively. k_{cd} is taken as 6.1×10^8 N/m$^{3/2}$ for contact radius $r_1 = \infty$ and r_2 = 0.005 m, Young's modulus $E_1 = 5.9\times10^9$ N/m^2 for the acrylic flat contact, and $E_2 = 210\times10^9$ N/m^2 for the steel spherical contact.

The sound pressure in the wooden box are calculated with the following constants: c = 340 m/s, ρ_a = 1.29 kg/m^3, β_q = 1.16 %. The acoustic damping factor was chosen to give comparable result with the experimental outcomes. In this case the acoustic damping factor was set such that the maximum peak for 4th mode in simulation result was almost the same as the peak spectrum obtained from experimental data.

Figure 3.7 shows the acceleration of floor at point B for three different cases. The first case is the response of the system without impact damper. The second and the third cases were the response of the system with mass ratios between impact damper and floor m_d/m_f of 0.6 and 1.2, respectively. In the simulation the floor mass m_f was set as 0.75 kg. The simulation results indicated that for mass ratios of 0.6 and 1.2 the maximum floor vibration could be reduced by 9% and 24%, respectively.

The simulation of velocity response at the center of the slab (point O_s) is shown in Fig. 3.8. The reductions of velocity response are about 47% and 62 % by using impact damper with mass ratio 0.6 and 1.2, respectively. The velocity response is dominated by

rigid body mode of vibration(4^{th} mode) as can be shown in the frequency response in Fig. 3.8. In the frequency response, the attenuations of velocity spectrum at the 8^{th} mode for mass ratios of 0.6 and 1.2 are 8.3 and 14 dB, respectively.

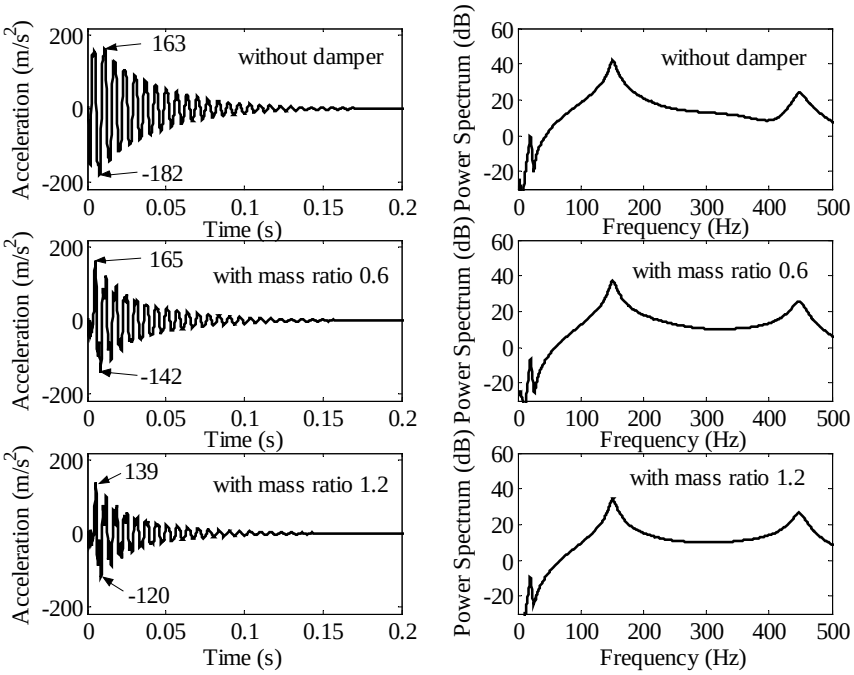

Fig. 3.7 Simulation results of acceleration in point B.

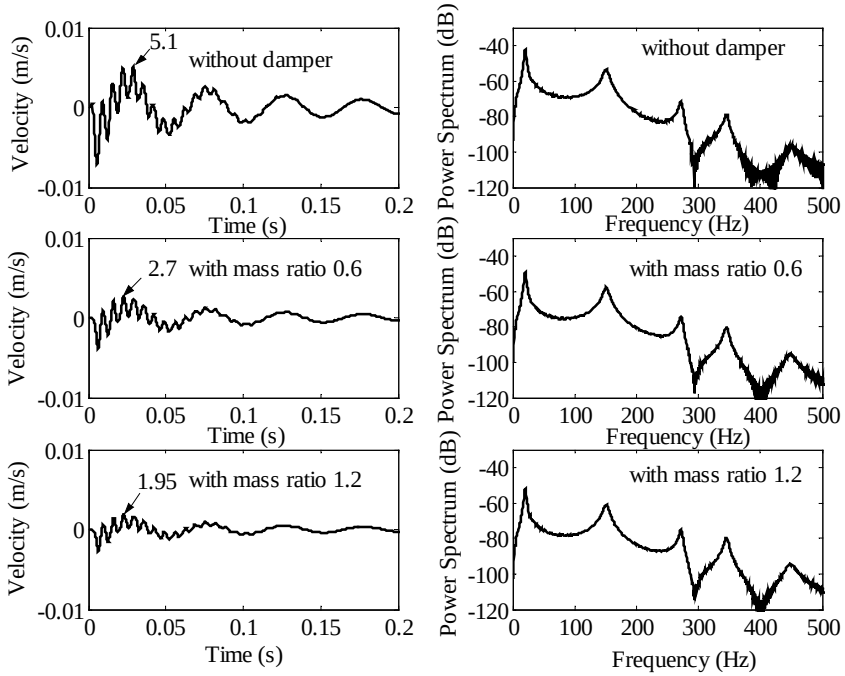

Fig. 3.8 Simulation results of velocity in point O_s.

Simulation results of sound pressure in the room bellow the slab is depicted in Fig. 3.9. The simulation results show that for mass ratios of 0.6 and 1.2, the sound pressure could be reduced by 53% and 67%, respectively. In the frequency response, the attenuations of sound power spectrum at the 8th mode for mass ratios of 0.6 and 1.2 are 4.6 and 7.7 dB, respectively.

It should be pointed out that the simulation results of floor acceleration response are dominated by 8th mode with frequency 151.1 Hz but for the sound pressure response, the 4th mode with frequency 19.9 Hz has the major contribution to the total response.

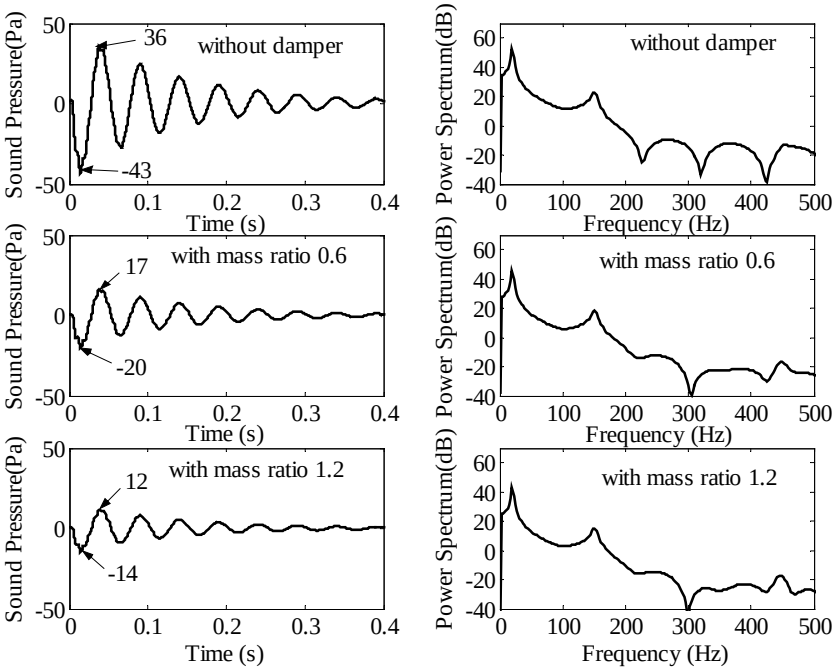

Fig. 3.9 Simulation results sound pressure in the wooden box.

The vibration suppression obtained by using impact damper is compared to conventional added mass method for high impact load case. The high impact load was obtained by dropping a mass with high contact stiffness to the floor. The mass tip was made from acrylic ball (m_b = 0.045 kg). The contact stiffness between floor and acrylic ball was obtained from Table 3.1. Three-simulation procedure was conducted. First, the response is calculated for case without damper. The second case is calculation using added mass 0.3 kg located in the center of the floor. The third case is calculation using impact damper with mass ratio 0.4(m_d = 0.3 kg). The impact damper was used to suppress the low frequency vibration response excited by impact force. For this reason the low pass filter within 1 kHz frequency was used in the analysis.

Figure 3.10 shows the comparison of floor acceleration in point B without damper,

with impact damper and with added mass cases, respectively. It can be shown from Fig. 3.10 that the impact damper has superior performance in suppressing 8th mode (151.1 Hz) and 18th mode (448.3 Hz) compare to added mass method.

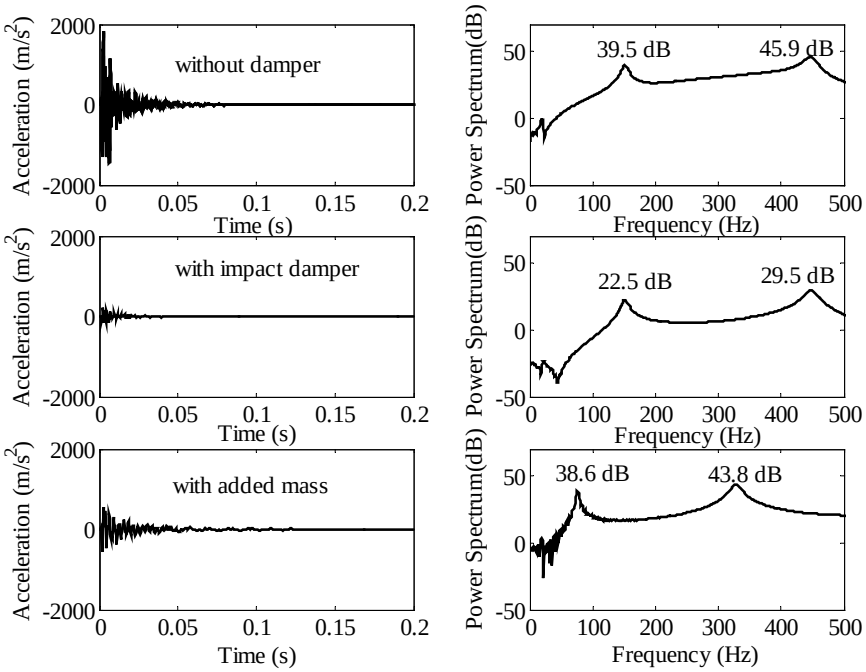

Fig. 3.10 Simulation results comparison of acceleration response.

Figure 3.11 shows the simulation results of sound pressure generation in the room bellow the slab for high impact load case. As the soft impact case, the sound pressure response is dominated by rigid body mode. It can be shown from Fig. 3.11 that the attenuation of sound pressure using impact damper is higher than the conventional added mass method.

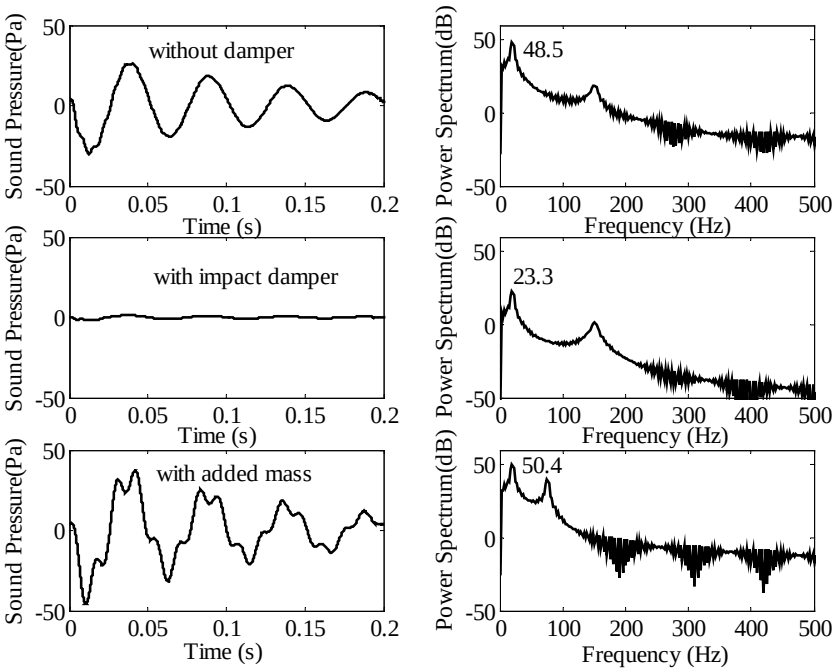

Fig. 3.11 Simulation results comparison of sound pressure.

3.6 Experimental Result

The simulation result of floor acceleration and sound pressure generation in the room bellow the slab was tested experimentally. Experimental results for the case of low impact load using tennis ball are shown in Fig. 3.12 and Fig. 3.13. Figure 3.12 shows that the maximum acceleration is reduced by 10 % and 25% by using the impact damper with mass ratios 0.6 and 1.2, respectively. There are two peaks appear between 150 Hz and 400 Hz which are not detected in simulation result. These peaks may be resulted from non-center collision between ball and floor.

The sound pressure response in the hypothetical room bellow the slab is shown in Fig. 3.13. Sound pressure is reduced by 50% and 63 % by the damper for mass ratios 0.6 and 1.2, respectively. Frequency response in Fig. 3.13 shows that the attenuations of sound power spectrum at the 8^{th} mode for mass ratios of 0.6 and 1.2 are 2.55 and 2.79 dB, respectively.

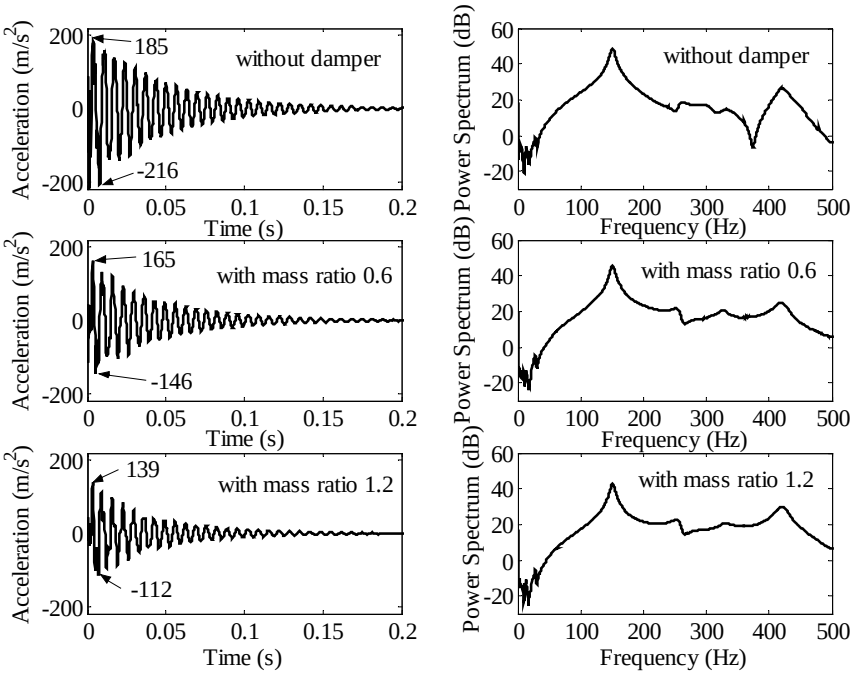

Fig. 3.12 Experimental results of acceleration in point B.

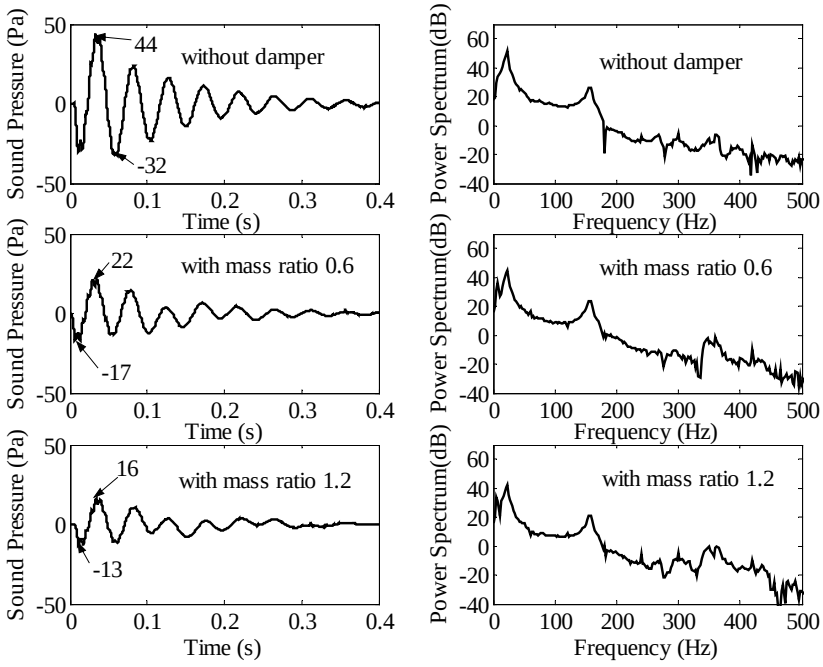

Fig. 3.13 Experimental results sound pressure in the wooden box.

Experimental results of floor acceleration for high impact load are depicted in Fig. 3.14. Figure 3.14 show that the vibration suppression obtained by using impact damper

for 8th mode was better than that of added mass case. The resonance peaks for this mode are 24.2 dB and 28.3 dB for impact damper case and added mass case, respectively. The resonance peak of 18th mode using impact damper is 31.4 dB. This value is lower than added mass case 32.8 dB. The experimental result of floor acceleration as depicted in Fig. 3.14 is lower than the simulation result as shown in Fig. 3.10, especially for case without impact damper. The reason is that, in the experiment, the impact location of the ball is not exactly located at the center of the floor. This un-centered impact force excites some of the higher modes.

Figure 3.15 shows the experimental results of sound pressure generation for high impact load. The sound pressure response is dominated by rigid body mode. The resonance peak of rigid body mode using impact damper and added mass method are 17.5 dB and 30.7dB, respectively. These results show that the attenuation of sound pressure generation using impact damper method is higher than that of the added mass method.

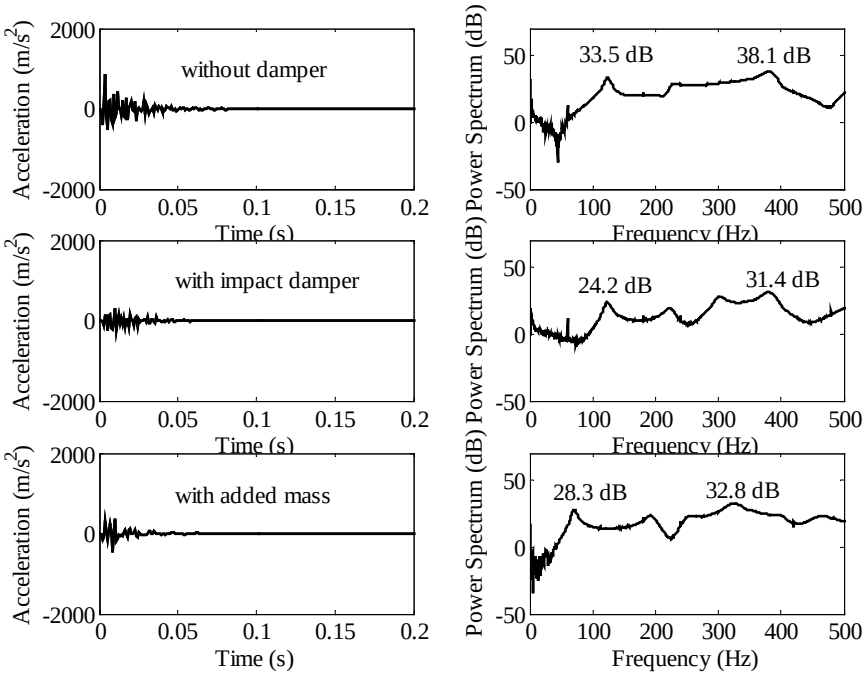

Fig. 3.14 Experimental results comparison of acceleration response.

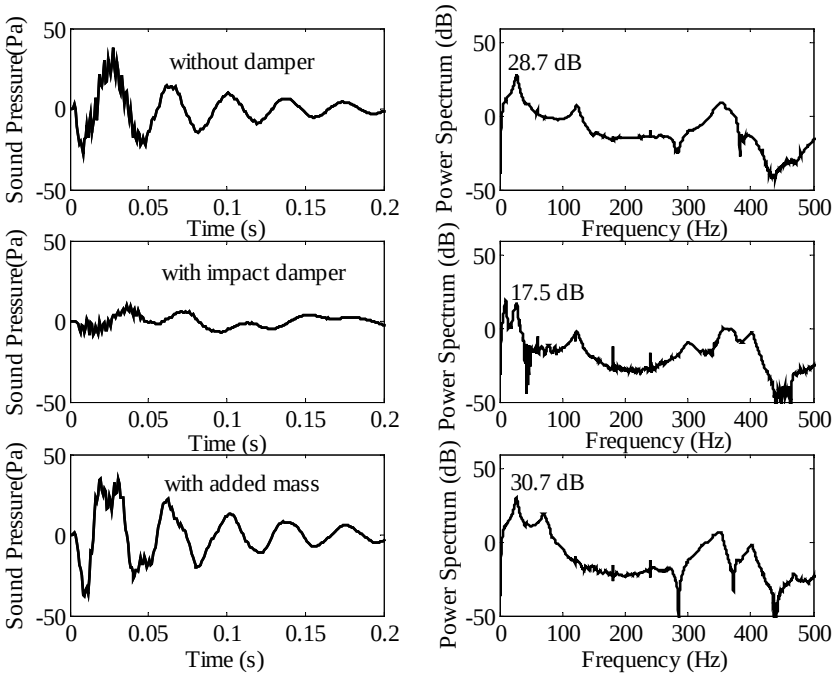

Fig. 3.15 Experimental results comparison of sound pressure.

3.7 Summary

In the present research, a new impact damper device has been invented to absorb floor vibration and to suppress the resulting sound pressure level generated by a flooring system. A numerical model of flooring system was generated using a FEM formulation. The model was order-reduced by using modal analysis. A small-scale model of flooring system was then fabricated to show the effectiveness of impact damper in reducing the impact vibration. Finally, the experimental results were compared to the model simulation results. The maximum floor impact vibration and sound generation depended strongly on the impact damper mass ratio. The experimental results show that for a mass ratio of 1.2, the acceleration of the floor and sound pressure generated could be reduced by 25% and 63%, respectively.

Comparison of impact damper method to conventional added mass at the center of the floor was conducted for case of high impact load. The results show that impact damper has the better performance compare to added mass method in suppressing the floor acceleration and sound pressure generation. Moreover, it was shown the transfer of energy obtained using ball with high contact frequency (acrylic ball) is much larger than obtained using ball with low contact frequency (tennis ball).

Chapter 4
APPLICATION OF MOMENTUM EXCHANGE IMPACT DAMPER TO FORGING MACHINE

4.1 Introduction

Industrial machines using impact force, such as forging machines, have two dominant problems relating to their dynamic operation. The first problem relates to the inertial force caused by rigid-body motion of the machines, which is excited by its reciprocating movement. The second problem relates to elastic vibration caused by the impacts. These problems compromize the machines accuracy and cause vibration pollution to the surroundings.

Conventional methods of addressing these problems typically involve using a floating base with a large mass to decrease the transmitted force. These methods fail to improve the vibration response of the forging machine bed. Some researchers use active dynamic damper with preview action to reduce the transient vibration subject to impact force (Tanaka and Kikushima, 1986,1987). This method effectively reduces the transmitted force and acceleration response. However, it requires sensors, a controller and an actuator to realize the preview action of the dynamic damper.

In this work, an innovative momentum exchange impact damper is proposed to reduce the vibration and transmitted force of the forging machine. This method is based on the momentum conservation principle for colliding bodies. When the forging machine bed is subjected to an impact force, a part of the energy of forging machine is transferred to the impact damper mass, which is initially contacting the forging machine bed.

4.2 New Impact Damper for Forging Machine

Figure 4.1 shows a dynamic model of a forging machine with an impact damper. There are four main components of this system. The first component is a slider, which is used as the impact force generator for the forging machine. The second component is the bed. The bed typically consists of a steel plate supported by four columns. These columns connect the forging machine bed to the third component, a floating base. The floating base is a steel plate supported by four coil springs. The last component is the impact damper. The impact damper consists of a mass, a spring and a dashpot.

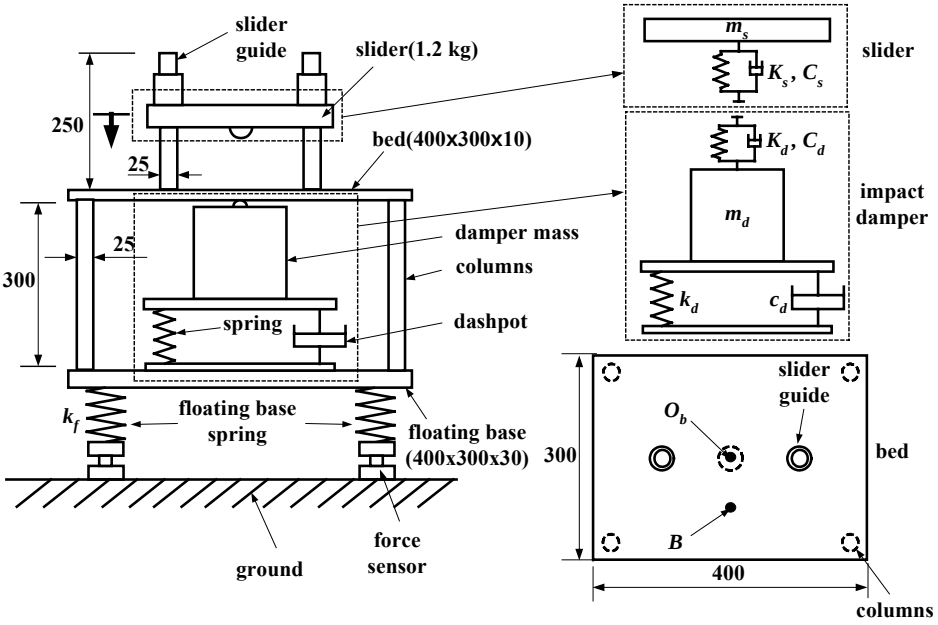

Fig. 4.1 Experimental model of a forging machine.

4.3 System Modeling and Equations of Motion

The dynamics of the forging machine structure, which consists of the slider guides, a bed, columns, a floating base and floating base springs is analyzed using the finite element method (FEM). Four-node quadrilateral plate elements are used to model both the bed and the floating base structure (see Appendix). The columns are modeled using the three dimensional frame elements (see Appendix). The slider and the impact damper are assumed to be rigid bodies.

Values for defining the slider, the bed, the impact damper and the floating base parameters are shown in Table 4.1.

Table 4.1 Simulation parameters for floating base, column, damper, slider and bed.

Parameter	Value
m_s : slider mass	1.2 kg
v_s : slider initial velocity	1.2 m/s
m_b: bed mass	10 kg
K_s : bed-slider contact stiffness	$1\times10^6 - 5\times10^7$ N/m
C_s : bed-slider contact damping coefficient	0 Ns/m
m_d : damper mass	3.6 kg, 7.2 kg
k_d : damper spring constant	1.8×10^3 N/m
c_d : damper damping coefficient	7×10^2 Ns/m
K_d: bed-damper contact stiffness	$5.5\times10^3 - 1.8\times10^9$ N/m

C_d : bed-damper contact damping coefficient	0 Ns/m
m_f : floating base mass	41 kg
k_f : floating base spring constant	1.54×10^4 N/m

The equations of motion of the forging machine structure, the slider and the impact damper are written as follows

$$\mathbf{M\ddot{u}} + \mathbf{C\dot{u}} + \mathbf{Ku} = \mathbf{B_{bs}}\, f_{bs} - \mathbf{B_{bd}}\, f_{bd} + \mathbf{B_{fd}}\, f_{fd}\,, \tag{4.1}$$

$$m_s \ddot{z}_s + f_{bs} = 0\,, \tag{4.2}$$

$$m_d \ddot{z}_d + f_{fd} - f_{bd} = 0\,, \tag{4.3}$$

where matrix **M**, **C** and **K** are the structure's; mass matrix, the damping matrix and the stiffness matrix, respectively; f_{bs}, f_{bd} and f_{fd} are the contact forces between the bed and the slider, the contact force between the bed and the impact damper and the transmitted force from the impact damper to the floating base, respectively; **u**, z_s and z_d are the displacement vectors of the structure, the displacement of slider and the displacement of the impact damper, respectively; $\mathbf{B_{bs}}$, $\mathbf{B_{bd}}$ and $\mathbf{B_{fd}}$ are vectors that represent the positions of external forces.

The contact force between the bed and slider is assumed to be given by a linear spring and a dashpot. Thus, the contact force can be expressed as

$$f_{bs} = \begin{cases} K_s\left(z_s - u_b\right) + C_s\left(\dot{z}_s - \dot{u}_b\right), & for\ \left(z_s - u_b\right) \geq 0 \\ 0, & for\ \left(z_s - u_b\right) < 0 \end{cases}, \tag{4.4}$$

where K_s and C_s are the contact stiffness and the contact damping coefficient between the slider and the bed, respectively, while u_b is the displacement of the bed at the contact point O_b. The transmitted force from the impact damper to the floating base can be expressed as

$$f_{fd} = c_d(\dot{z}_d - \dot{u}_f) + k_d(z_d - u_f)\,, \tag{4.5}$$

where k_d and c_d are the stiffness and the damping coefficients of the impact damper, respectively, while u_f is the displacement of the floating base at point O_f. The impact damper is designed such that it moves smoothly during the impact such that it dissipates energy when it releases. A one-way damper is used for this purpose. Mathematically, the damping coefficient can be expressed as

$$c_d = 0 \quad for\ \ \dot{z}_d - \dot{u}_f > 0\ . \tag{4.6}$$

The contact force between the bed and the impact damper is modeled using a linear spring and dashpot model

$$f_{bd} = \begin{cases} K_d\left(u_b - z_d\right) + C_d\left(\dot{u}_b - \dot{z}_d\right), & for\ \left(u_b - z_d\right) \geq 0 \\ 0, & for\ \left(u_b - z_d\right) < 0 \end{cases}, \qquad (4.7)$$

where C_d and K_d are the contact damping coefficient and the contact stiffness between the impact damper and the bed, respectively.

Equation (4.1) can be written in modal coordinates giving

$$\ddot{q}_i + 2\zeta_i\omega_i\dot{q}_i + \omega_i^2 q_i = \boldsymbol{\psi}_i\left[\mathbf{B_{bs}} f_{bs} - \mathbf{B_{bd}} f_{bd} + \mathbf{B_{fd}} f_{fd}\right] \ , \ \mathrm{i} = 1,2,\cdots,\infty , \qquad (4.8)$$

where q_i, ζ_i, ω_i, and $\boldsymbol{\psi}_i$ are the modal displacements, the damping ratio, the natural frequency and the mass normalized eigenvector for the ith mode, respectively.

Figure 4.2 shows two mode shapes of the forging machine without a damper obtained from the FEM. The 6th and the 10th modes significantly contribute to the transfer of energy during the collision process. The 6th mode is the rigid body mode of forging machine and the 10th mode is the most dominant elastic mode of bed.

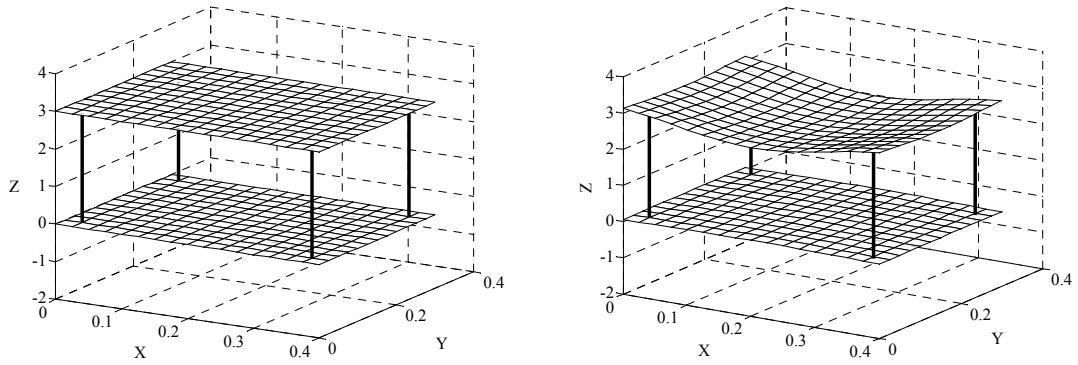

(a) 6th mode 6.35 Hz (b) 10th mode 283 Hz

Fig. 4.2 Significant mode shapes of the bed, column and floating base.

4.4 Energy Transfer and Transmitted Force

The main purpose of the impact damper is to minimize the momentum or energy of the forging machine. Generally, the transfer of momentum in the collision of elastic bodies is influenced by the mass ratio and the contact time. In order to find the optimum mass ratio and contact stiffness, several simulations were conducted. In the simulations, the energy of the forging machine after collisions are calculated as

$$E_{p+} = E_{s-} - E_{s+} - E_{d+} \tag{4.9}$$

where E_{p+}, E_{s-}, E_{s+} and E_{d+} are the energy of the forging machine after collision, the energies of the slider before and after collision and the energy of the impact damper after collision, respectively. These energies are calculated as

$$E_{s-} = T_{s-} = \frac{1}{2} m_s \dot{z}_{s-}^2 \quad , \tag{4.10}$$

$$E_{s+} = T_{s+} = \frac{1}{2} m_s \dot{z}_{s+}^2 \tag{4.11}$$

$$E_{d+} = T_{d+} + U_{d+} = \frac{1}{2} m_d \dot{z}_{d+}^2 + \frac{1}{2} k_d \left(z_d - u_f \right)_+^2 \quad . \tag{4.12}$$

where $\dot{z}_{s-}$, $\dot{z}_{s+}$, $\dot{z}_{d+}$ and $\left(z_d - u_f \right)_+$ are velocities of the slider before and after collision, velocity of the damper after collision and relative displacement of the damper after collision, respectively. T_{s-}, T_{s+}, T_{d+} and U_{d+} are the kinetic energies of the slider mass before and after collision, kinetic energy of the damper mass after collision and potential energy of the damper spring after collision, respectively. It can be assumed that there is no potential energy just after the collision.

The analysis of energy transfer from the slider to the damper was conducted for three different cases. For the first and second cases, the forging machine's floating base was supported by a spring with low stiffness(k_f = 1.54×10^4 N/m) and high stiffness(k_f = 1×10^7 N/m). In the third case, the forging machine column was connected rigidly to the ground without using a floating base.

4.4.1 Case 1: Using Floating Base with Soft Support Springs

The numerical integrations of Eqs. (4.2), (4.3) and (4.8) was carried in a MatLab/Simulink computational environment by using the fifth-order Dormand-Prince method with variable time steps. In the simulation, only the 6th mode (ω_6 = 40 rad/s) and 10th mode (ω_{10} = 1777 rad/s) were considered because they were dominant. Figure 4.3 shows the ratio of transferred energy (E_{p+}/ E_{s-}) as a function of ω_s / ω_6 and ω_d / ω_6 for mass ratios (m_d/m_b) of 0.35 and 0.7. The variables, ω_s and ω_d, are the natural frequencies of the slider and the impact damper.

$$\omega_s = \sqrt{\frac{K_s}{m_s}} , \tag{4.13}$$

$$\omega_d = \sqrt{\frac{K_d}{m_d}}\,. \tag{4.14}$$

These variables relate to the contact time with the bed.

As can be seen from Fig. 4.3, the minimum energy of the forging machine occurs in the neighborhood of the point where $\omega_d = \omega_s$. This energy decreases when the frequency ratio ω_s/ω_6 is increased. The conclusion that can be draw from these figures is that K_s must be higher in order to minimize the energy of the forging machine.

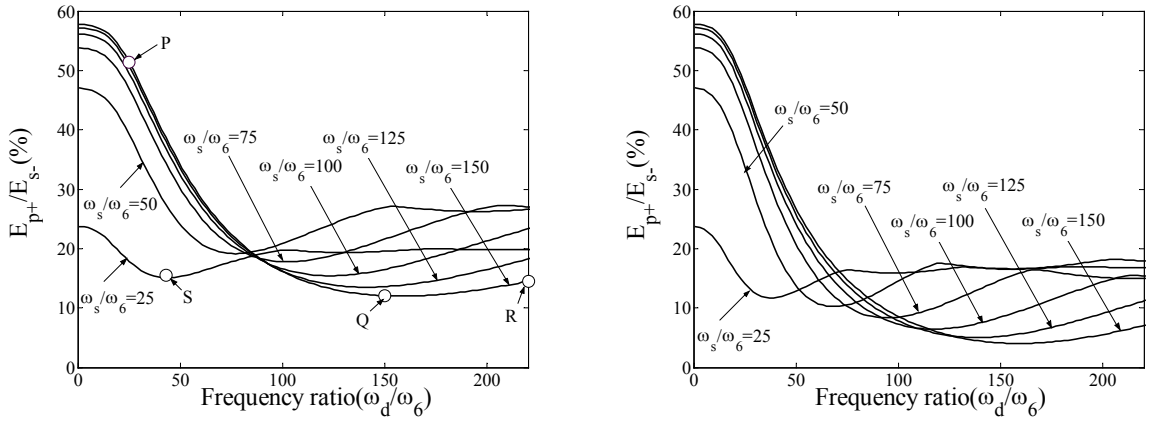

(a) m_d/m_b =0.35 (a) m_d/m_b =0.7

Fig. 4.3 Relationship between energy transfer and contact condition.

Figure 4.4 shows the variation of the forging machine energy ratio with the frequency ratio ω_d/ω_s and the impact damper mass ratio m_d/m_b. In the simulation, ω_s and ω_6 were fixed to be 6×10^3 rad/s and 40 rad/s, respectively, and the contact frequency ω_d were varied. Increasing the impact damper mass ratio causes the energy of the forging machine to decrease. The minimum energy is located at point ω_d/ω_s = 1 for all mass ratios. Considering the energy ratio E_{p+}/E_{s-} as impact damper efficiency, it can be concluded that the optimal frequency ratio ω_d/ω_s that is close to 1 is independent of the impact damper mass. For the optimal impact damper with a mass ratio of 1, E_{p+}/E_{s-}= 2.2 % as shown in Fig. 4.4.

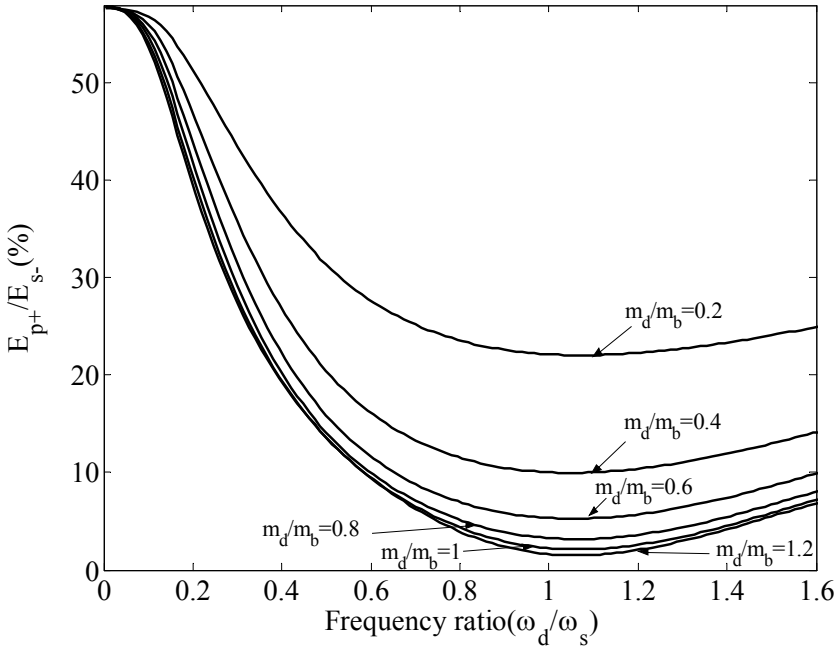

Fig. 4.4 Relationship between energy transfers and mass ratio.

Figure 4.5 shows the variation of the forging machine energy ratio when the frequency ratio ω_s/ω_6 and the mass ratio m_d/m_b are varied. In this simulation the natural frequency ω_6 = 40 rad/s and the contact frequency ω_s and ω_d were varied. During the simulation, the contact frequency ω_d is set to the same value as ω_s and m_s was kept constant. The curves for the energy have a maximum peak at the point close to ω_s/ω_6 = 45 (ω_s : 283 Hz). This was because the natural frequency of the 10th mode of the forging machine (ω_{10}) is 283 Hz and this value is the same as the contact frequency ω_s. At this point, the energy of the forging machine increases due to resonance. When the forging machine is operating at $\omega_s/\omega_6 < 45$, the impact damper mass ratio has little influence on the energy of the forging machine as shown in Fig. 4.5. However, for $\omega_s/\omega_6 > 45$, the mass ratio has a significant effect in determining the energy of forging machine after the impact. This is because, for $\omega_s/\omega_6 < 45$, the slider contact stiffness is so small that the amount of energy reflected to the slider is larger than the amount transferred. As shown in chapter 2, for this condition, the mass ratio has little influence on the amount of reflected energy. When $\omega_s/\omega_6 >> 45$, the energy transferred to the damper increases and this transferred energy is influenced greatly by the mass ratio.

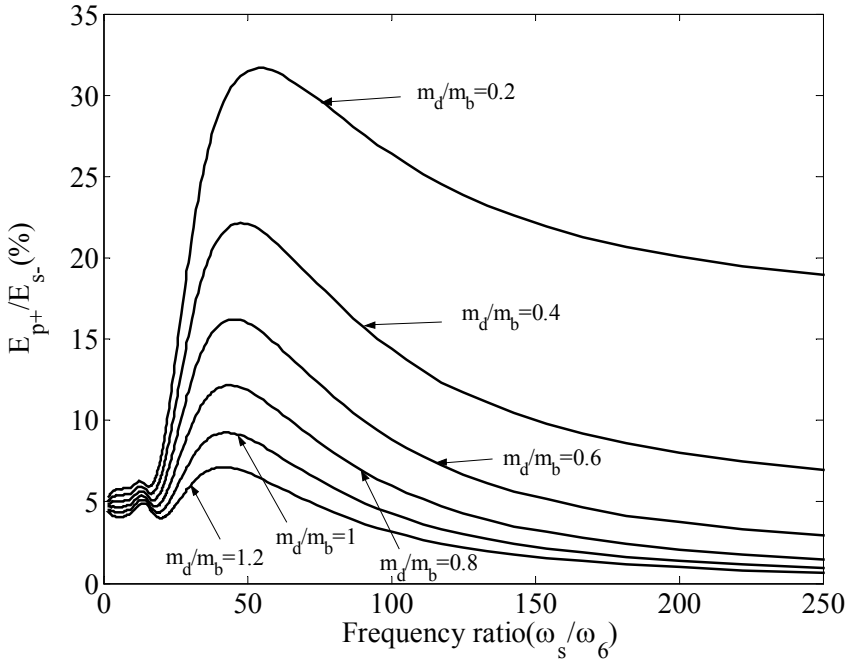

Fig. 4.5 Variation of energy ratio with frequency ratio ω_s/ω_6 and mass ratio m_d/m_b.

The time history of the energy during collision for a mass ratio of 0.35 and ω_s/ω_6=150 are depicted in Figs. 4.6-4.8. The energy components in Figs. 4.6-4.8 are calculated as follows.

1. The kinetic energy of the slider is

$$KE\,m_s = \frac{1}{2} m_s \dot{z}_s^2 \quad , \tag{4.15}$$

2. The potential energy stored internally by the slider contact spring is

$$PE\,K_s = \frac{1}{2} K_s \left| \left(z_s - u_b \right)^2 \right| \times \frac{1}{2} \left(1 - \mathrm{sgn}\left(z_s - u_b \right) \right), \tag{4.16}$$

3. The kinetic energy and potential energy of the forging machine

$$KE_p = \frac{1}{2} \left\{ \dot{\mathbf{X}} \right\}^{\mathbf{T}} \left[\mathbf{M} \right] \left\{ \dot{\mathbf{X}} \right\}, \tag{4.17}$$

$$PE_p = \frac{1}{2} \left\{ \mathbf{X} \right\}^{\mathbf{T}} \left[\mathbf{K} \right] \left\{ \mathbf{X} \right\}, \tag{4.18}$$

where $\{\mathbf{M}\}$, $\{\mathbf{K}\}$, $\{\mathbf{X}\}$ and $\{\dot{\mathbf{X}}\}$ are the modal mass, the modal stiffness, the displacement vector and the velocity vector of the forging machine, respectively.

4. The kinetic energy of the damper is

$$KE\, m_d = \frac{1}{2} m_d \dot{z}_d^2 \quad , \tag{4.19}$$

5. The potential energy stored in the damper spring is

$$PE\ k_d = \frac{1}{2} k_d \left(z_d - u_f \right)^2 , \tag{4.20}$$

6. The potential energy stored internally by the damper contact spring is

$$PE\, K_d = \frac{1}{2} K_d \left| \left(u_b - z_d \right)^2 \right| \times \frac{1}{2} \left(1 - \mathrm{sgn}\left(u_b - z_d \right) \right), \tag{4.21}$$

7. Energy dissipated by the forging machine structural damping is given by

$$Dissipated\ energy = KE\, m_{s-} - \left[PE\, K_s + KE\ structure + PE\ structure \right.$$

$$\left. + KE\, m_d + PE\, k_d + PE\, K_d \right], \tag{4.22}$$

where $KE\ m_{s-}$ is the kinetic energy of the slider before collision.

It should be noted that the energy of the forging machine is the summation of kinetic energy, potential energy and dissipated energy.

$$E_p = KE_P + PE_p + Dissipated\ energy\ . \tag{4.23}$$

Calculation of the energy components is conducted for $\omega_s / \omega_6 = 150$. Figures 4.6, 4.7 and 4.8 show the time history of energy for $\omega_d / \omega_6 = 150$ (point Q in Fig. 4.3 (a)), $\omega_d / \omega_6 = 25$ (point P in Fig. 4.3(a)) and $\omega_d / \omega_6 = 220$ (point R in Fig. 4.3(a)). Compared to the kinetic energy at point P and point R, the kinetic energy of the damper at point Q is much larger. This occurs because when the contact takes place, there is steady drop in the kinetic energy of the slider ($KE\ m_s$) as a result of energy transfer to the other energy compartments.

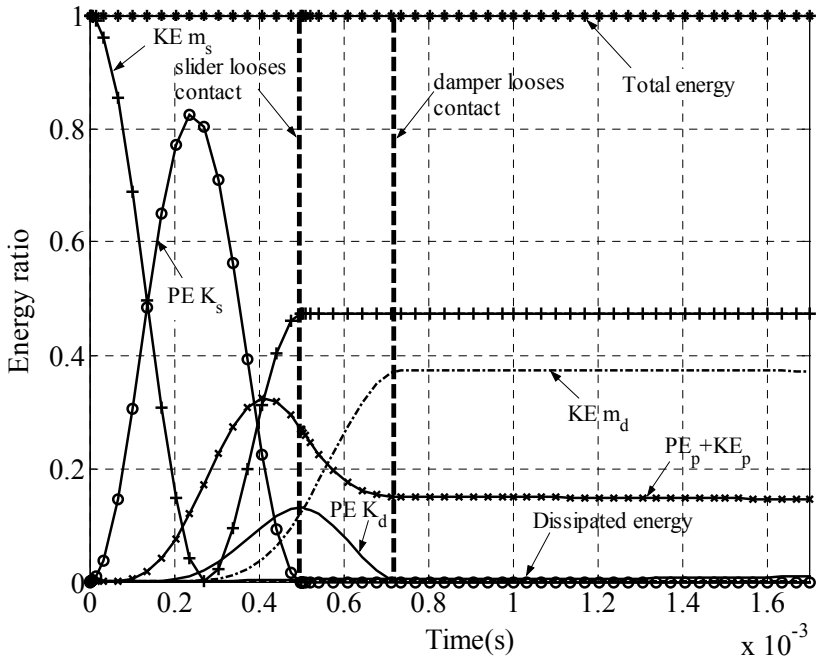

Fig. 4.6 Energy time history for m_d/m_b =0.35, ω_s/ω_6=150 and ω_d/ω_6=150 (point Q).

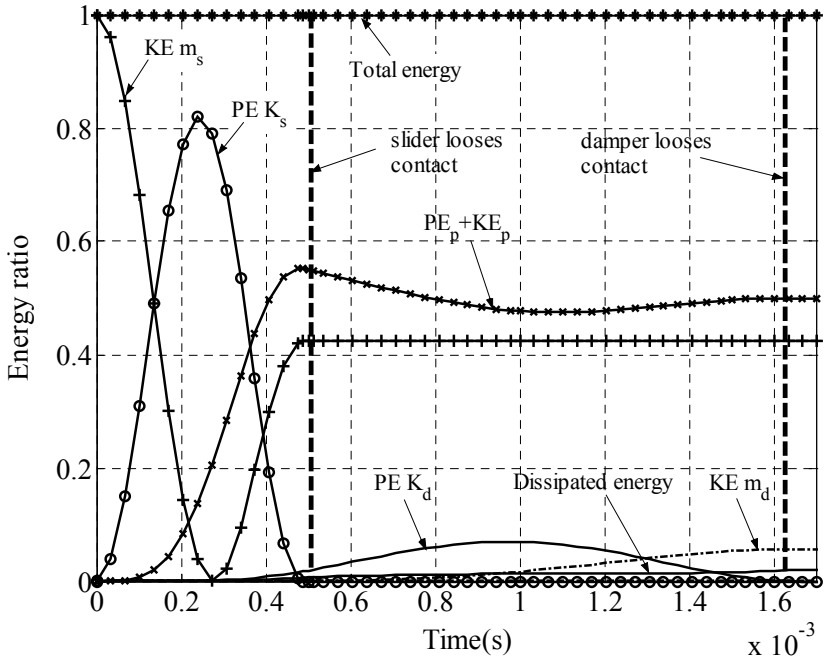

Fig. 4.7 Energy time history for m_d/m_b =0.35, ω_s/ω_6=150 and ω_d/ω_6=25 (point P).

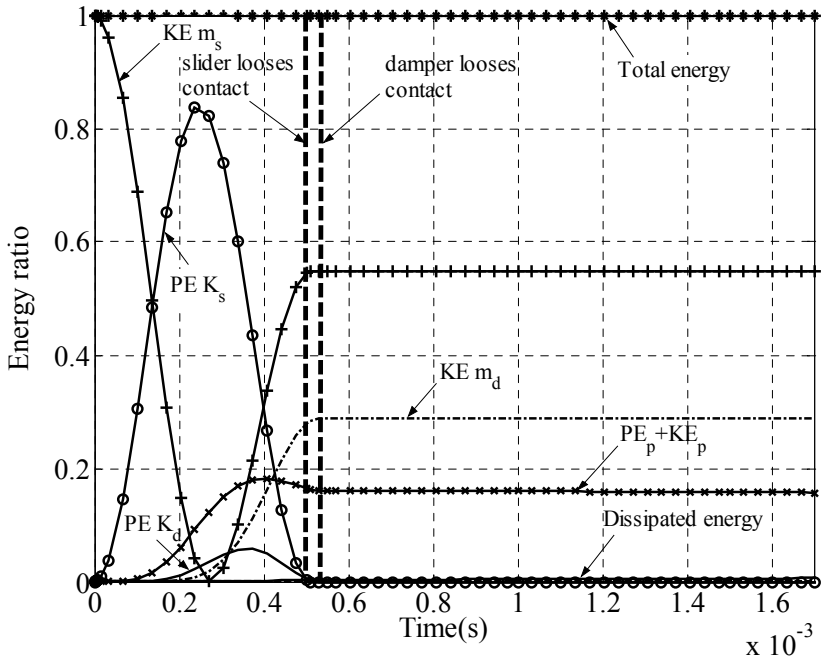

Fig. 4.8 Energy time history for m_d/m_b =0.35, ω_s/ω_6=150 and ω_d/ω_6=220 (point R).

The portion of energy transferred into the kinetic energy of the impact damper (*KE* m_d) is greatly influenced by the amount of potential energy stored in the impact damper contact spring (*PE* K_d). Figure 4.6 shows that when the impact damper is working at point Q, the maximum value of *PE* K_d occurs at the same time at which the slider losses contact.

When the impact damper is working at point P, as shown in Fig. 4.7, the kinetic energy of the impact damper after collision is smaller than that at point Q. This occurs because in this case the maximum value of *PE* K_d occurs after the slider losses contact. Alternatively, when the damper is working at point R, the maximum value of *PE* K_d occurs before the slider losses contact, so that the kinetic energy of the impact damper is lower than that at point Q.

The conclusion that can be reached from the above analysis is that the maximum energy transfer from the slider to the impact damper is obtained if the time when *PE* K_d is at a maximum and the time when slider looses contact are the same.

One of the conventional ways to reduce impact vibration is to add a mass on the bed or floating base. Comparison of performance of the impact damper with the conventional added mass method is depicted in Fig. 4.9. In this simulation the weight of the added mass is the same as that of the impact damper with a mass ratio 0.35. The frequency ratio of the impact damper is ω_d/ω_s=1. Figure 4.9 shows that the impact

damper has a better performance compared to the added mass method in the whole frequency range defined by the impact stiffness (ω_s/ω_6).

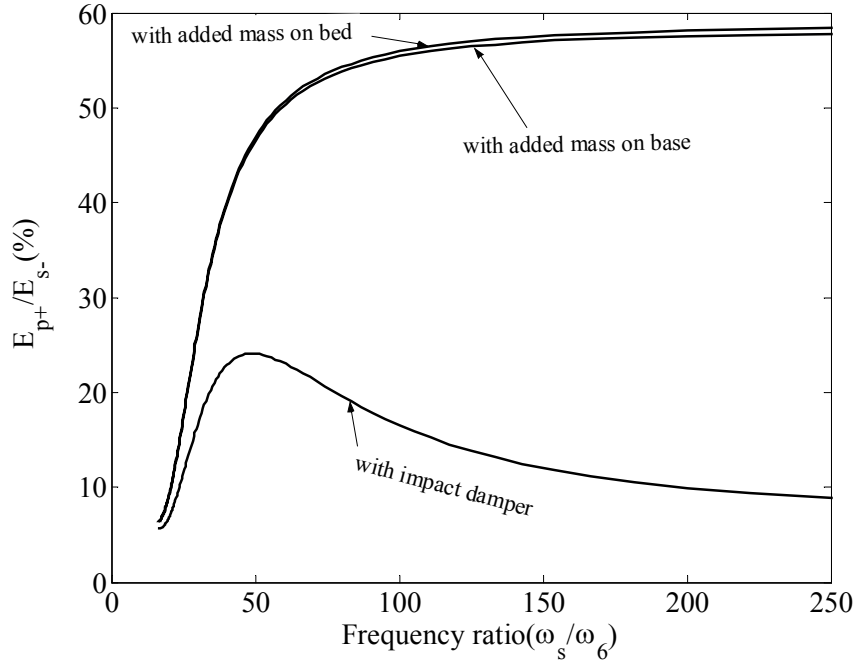

Fig. 4.9 Comparison between added mass and impact damper method.

Figure 4.10 and 4.11 show the simulated acceleration of the bed and transmitted force to the ground at the operating point S (see Fig. 4.3 (a)) for three cases: without impact damper, with impact damper and with added mass on the base. The added mass and the impact damper mass are $m_d/m_b = m_{add}/m_b = 0.35$. The acceleration and the transmitted force for the impact damper case are less than without the impact damper and the added mass cases. The added mass case has low transmitted force, but the acceleration response is poor compared to the impact damper case. Note that the acceleration response is dominated by elastic mode of the bed (283 Hz). Meanwhile the transmitted force is dominated by rigid body vibration (6.35 Hz).

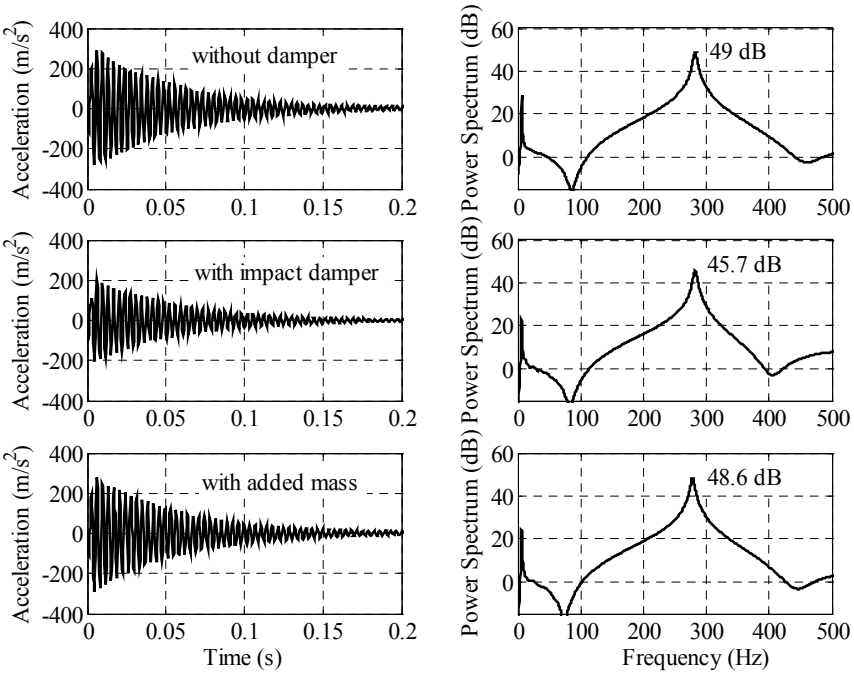

Fig. 4.10 Simulated acceleration response at point S.

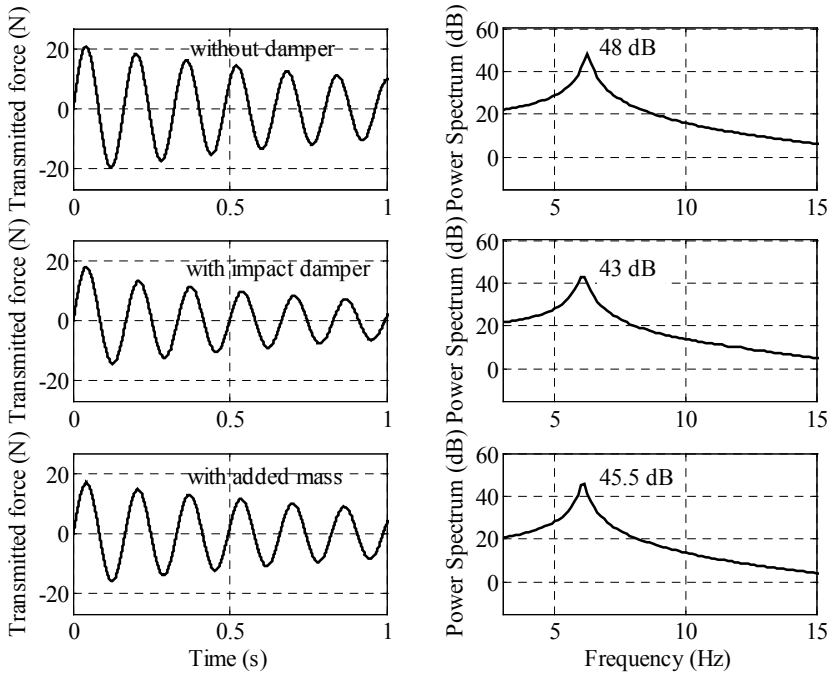

Fig. 4.11 Simulated force transmission at point S.

4.4.2 Case 2: Using Floating Base with Hard Support Springs

Figure 4.12 shows the forging machine energy obtained from the simulation by using a floating base stiffness $k_f = 1 \times 10^7$ N/m. This stiffness value is much larger than the stiffness used in the previous simulation. By using this spring, the 6th and 10th natural frequencies of the forging machine become 141 Hz and 292 Hz, respectively, while in the case of $k_f = 1.54 \times 10^4$ they are 6.35 Hz and 283 Hz. The mass ratio in this simulation is 0.35. Compared to the case with $k_f = 1.54 \times 10^4$ in Fig. 4.3 (a), the shapes of energy curve are similar and the minimum point is located in the vicinity of $\omega_d = \omega_s$.

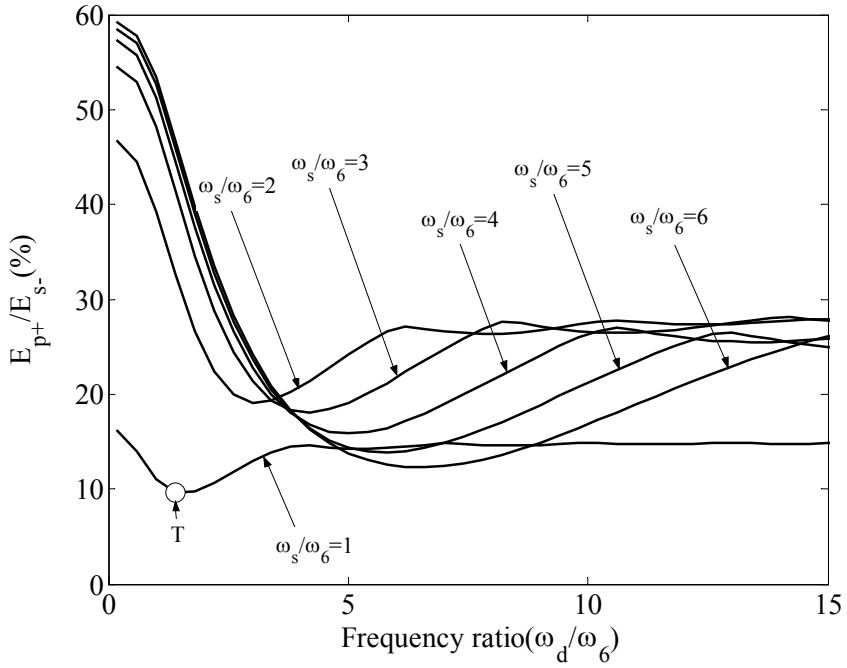

Fig. 4.12 Relationship between energy transfer and contact condition for $K_f = 1 \times 10^7$.

Figure 4.13 and Fig. 4.14 show the response of the bed acceleration and transmitted force at the operating point T in Fig. 4.12. The contact stiffness between slider and bed (K_s) at point T is the same as K_s at point S in Fig. 4.3 (a). It can be shown that the acceleration and transmitted force are less than those in the case with the soft support spring because most of energy of the slider is reflected back to the slider after the impact. By using the impact damper, the acceleration and transmitted force can be reduced by about 3 dB.

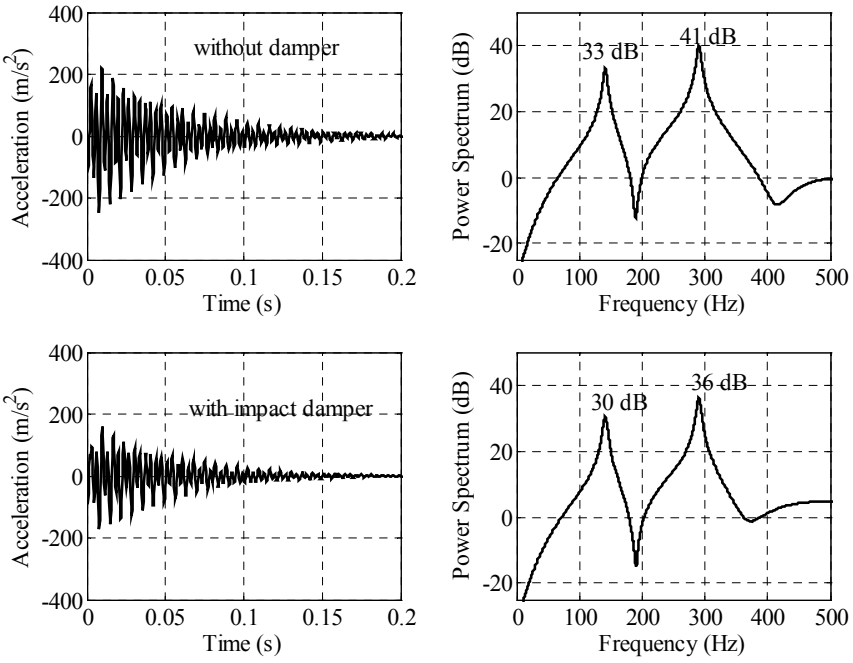

Fig. 4.13 Simulated acceleration at point T.

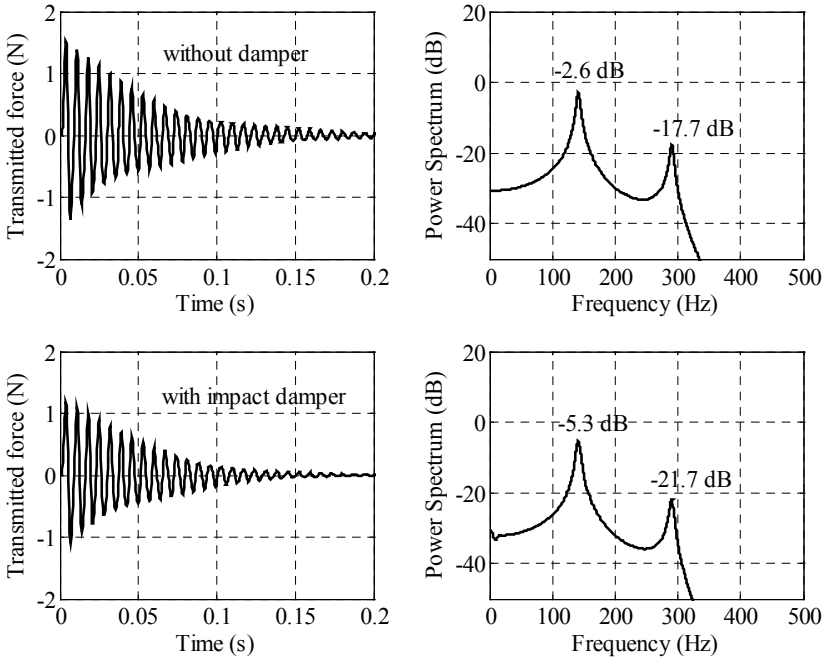

Fig. 4.14 Simulated force transmission at point T.

4.4.3 Case 3: Without Floating Base

In the case of small forging machine, the columns are usually connected directly to the ground without using a floating base. The transmitted force is simply calculated from the column's deflection ($F_t = k_c x_c$ where k_c and x_c are the stiffness and deflection of column, respectively). Several mode shapes of forging machine without floating base are depicted in Fig. 4.15. It can be shown from these figures that the 4th and 5th modes are significant for the case when the excitation point is located at the center of the bed.

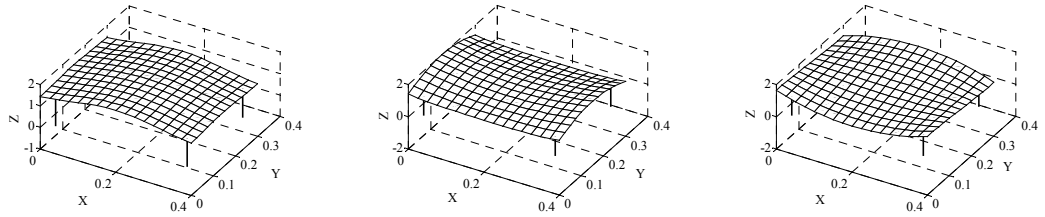

(a) 4th mode, 216 Hz (b) 5th mode, 275.6Hz (c) 6th mode, 281 Hz

Fig. 4.15 The significant mode shapes of forging machine without floating base.

Figure 4.16 show the variation of forging machine energy using the impact damper for cases without a floating base. The energy of forging machine is minimum at a point close to $\omega_s = \omega_d$ as shown in Fig. 4.16.

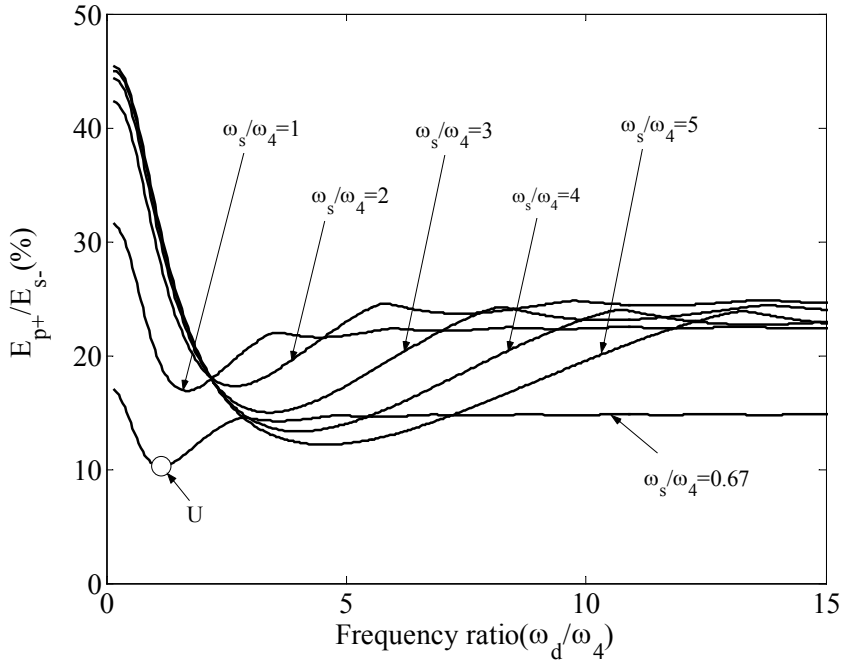

Fig. 4.16 Relationship between energy transfer and contact condition without a floating base.

Figure 4.17 shows the variation of energy with frequency ratio ω_s/ω_4 and mass ratio m_d/m_b. In this simulation the contact frequency ω_s and ω_d were varied. During the simulation, the contact frequency ω_d was set to the same value as ω_s and m_s was held constant. The energy curve has a maximum peak at the point close to $\omega_s/\omega_4 = 1$ because the resonance occurs when the excitation frequency ω_s is the same as the bed natural frequency ω_4.

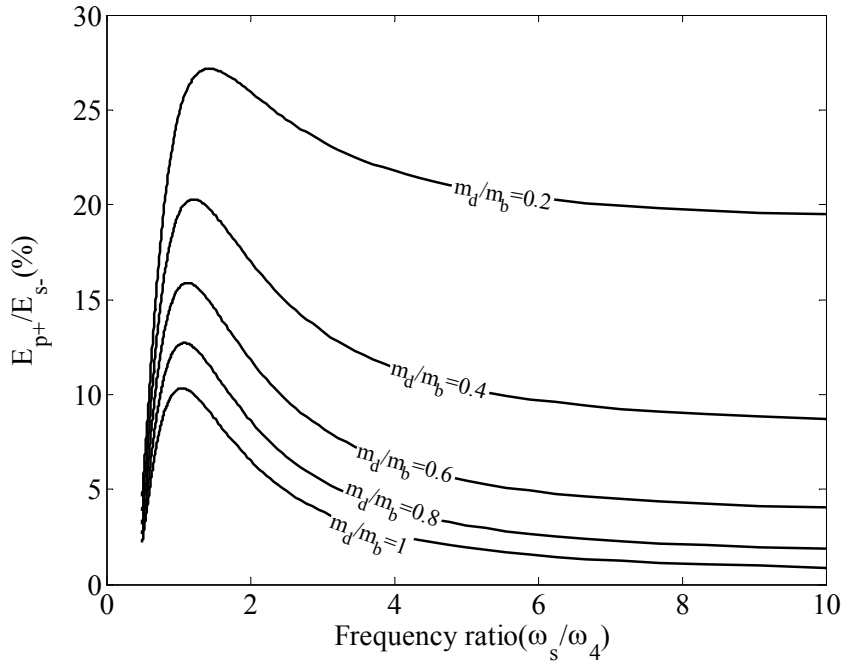

Fig. 4.17 Variation of energy with frequency ratio ω_s/ω_4 and mass ratio m_d/m_b.

The acceleration response at the center of bed and transmitted force from the column to ground at the operating point U(see Fig. 4.16) are depicted in Fig. 4.18 and Fig. 4.19. Figure 4.18 shows that the 4th mode of the forging machine has the most dominant peak. The peak for the 5th mode is small compared to the peak of the 4th mode. The attenuation of the peak acceleration by the impact damper with a mass ratio of 0.35 is 2.3dB.

The response of transmitted force from the column is depicted in Fig. 4.19. It can be shown from this figure that the transmitted force is reduced by 2.4 dB by using the impact damper with mass ratio of 0.35.

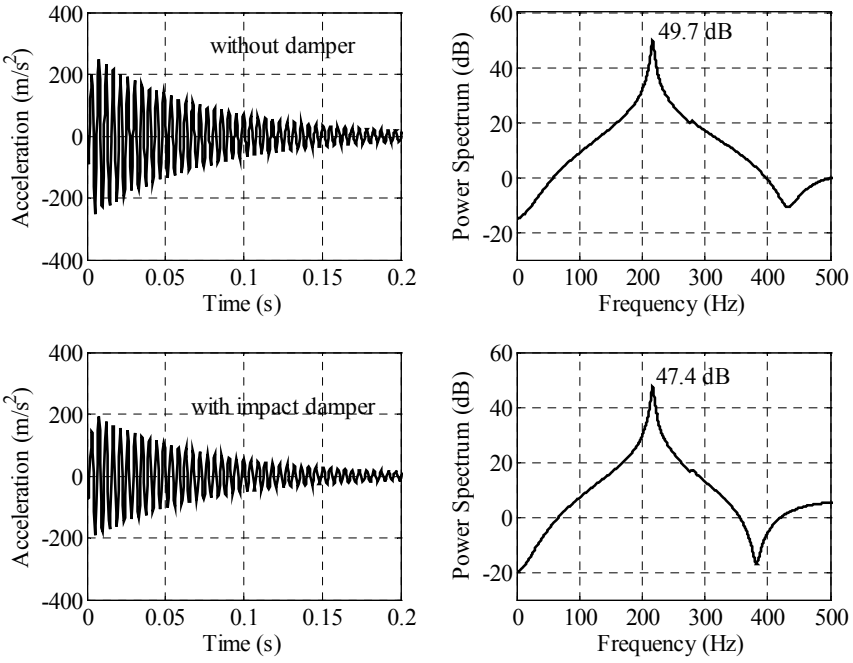

Fig. 4.18 Simulated acceleration response at point U($\omega_s = \omega_d$).

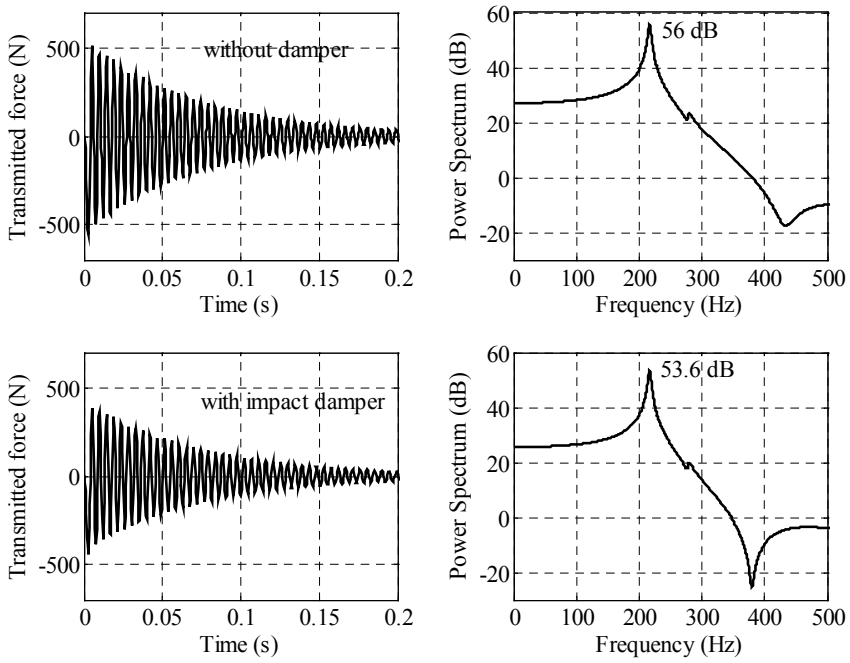

Fig. 4.19 Simulated force transmission at point U($\omega_s = \omega_d$).

4.5 Experimental Validation

In order to validate the simulation results, experiments were carried out using an experimental apparatus. The shape, size and parameter values are shown in Fig. 4.1 and Table 4.1. A photo of the experimental apparatus is shown in Fig. 4.20. Accelerometer and force transducer sensors were used in the experiment. The accelerometer is used to measure the acceleration response of bed. The acceleration measurement point is located at point B as depicted in Fig. 4.1. The force sensor is located at one of the floating base springs to measure the force transmitted to the ground.

Fig. 4.20 Photo of experimental apparatus.

The experimental results of the acceleration and transmited force for the case with the soft support spring and mass ratio of 0.35 are shown in Fig. 4.21 and 4.22. These figures show that the acceleration and transmitted force response can be reduced by 3.2 dB and 3.3 dB by using the impact damper. These experimental results and the simulation results in Fig. 4.10 and 4.11 are in good agreement, suggesting that the simulation results are reliable.

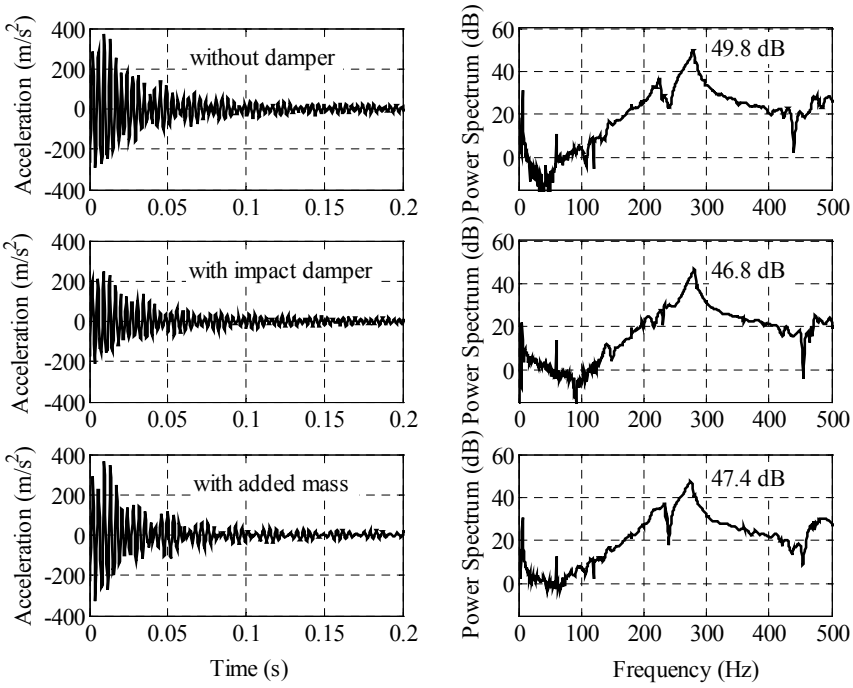

Fig. 4.21 Experimentally measured acceleration response.

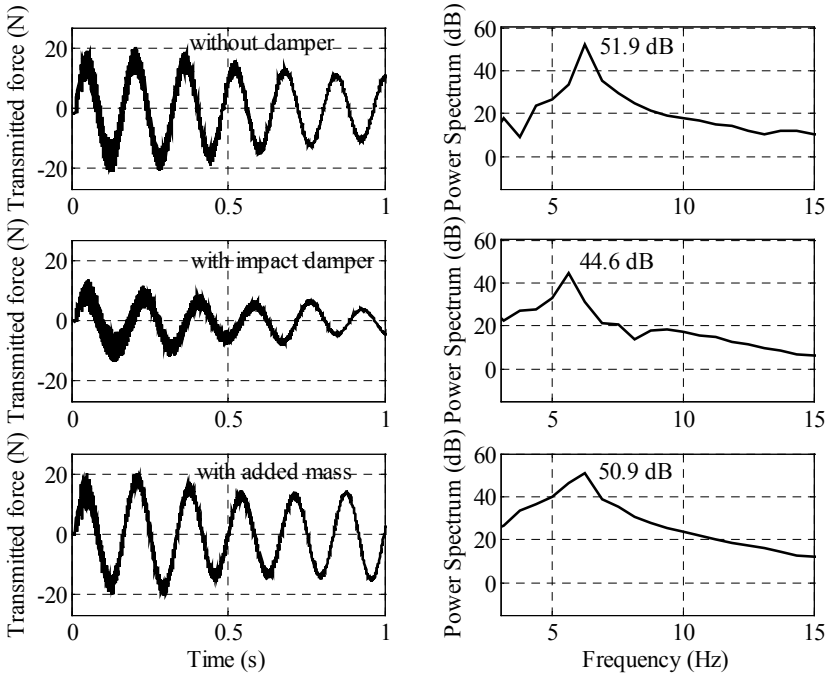

Fig. 4.22 Experimentally measured force transmission.

4.6 Summary

The proposed forging machine impact control method which is based on a momentum exchange principle exhibited a high level of vibration isolation and suppression. As shown in the simulation and experimental results, the vibration suppression depends on the mass ratio of the impact damper and the bed and the contact properties and natural frequencies of the forging machine. The energy of the forging machine will be decreased when the mass ratio increases. In addition, the transfer of energy from the slider to the damper also increases when the excitation frequency ω_s is much larger than the natural frequency of the forging machine. In the region where the excitation frequency ω_s is lower than the natural frequencies of the bed, the energy stored in the forging machine is not greatly influenced by the mass ratio because the reflected energy of the slider is dominant. However, in the region where the excitation frequency ω_s is higher than the natural frequencies of the bed, the transferred energy from slider to impact damper is dominant and the mass ratio plays a significant role in determining the energy of the forging machine. When one of the natural frequencies of the forging bed is the same as the excitation frequency, the forging machine resonates and the performance of the impact damper is poor.

Chapter 5
APPLICATION OF MOMENTUM EXCHANGE IMPACT DAMPER TO BOAT

5.1 Introduction

The safety and comfort are two important aspects that should be considered in designing a good transportation system such as a high speed boat. One important thing that affects this consideration is the shock vibration when the boat impacted by a wave. The shock vibration will induce the big acceleration that could be felt by the boat crews. Moreover, in the severe case a crack could be propagating in the structural material located at the bottom of the boat.

A method involving momentum exchange using an impact damper was proposed to reduce the shock vibration of a boat. The momentum exchange impact damper was previously used to reduce the impact vibration in the flooring system and the forging machine (Son and Matsuhisa, 2006). In this work the momentum exchange impact damper is applied to the boat. When the boat is impacted by a big wave, the kinetic energy of the boat is transferred to the absorber mass. Consequently, the boat receives a small amount of shock.

5.2 Two Degree of Freedom Model of Boat with Impact Damper

Figure 5.1 shows two degrees of freedom model representing the boat with impact damper. The boat was modeled by a mass m and a spring stiffness k. The impact damper was modeled using spring-mass system attached to the boat with mass m_d and stiffness k_d. The wave excitation is modeled as a half sinusoidal force with amplitude F_w and frequency ω_w.

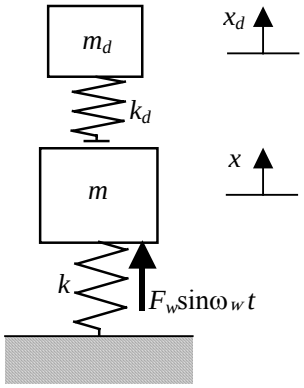

Fig. 5.1 Two degree of freedom model of boat.

The governing equation of boat model depicted in Fig. 5.1 are expressed as

$$m_d \ddot{x}_d - f_d = 0, \tag{5.1}$$

$$m\ddot{x} + kx + f_d = f_w. \tag{5.2}$$

where f_d and f_w are contact force between mass m and m_d and the force acting on mass m caused by wave excitation. These forces can be expressed as

$$f_d = \begin{cases} k_d\left(x - x_d\right), & for\ \left(x - x_d\right) \geq 0 \\ 0 \quad , & for\ \left(x - x_d\right) < 0 \end{cases}, \tag{5.3}$$

and

$$f_w = \begin{cases} F_w \sin \omega_w t, & for\ \ t \leq \dfrac{\pi}{\omega_w} \\ 0 \quad , & for\ \ t > \dfrac{\pi}{\omega_w} \end{cases}. \tag{5.4}$$

To investigate the free vibration for the system in Eq. (5.1) and (5.2) during contact period, the external force f_w is set equal to zero and the following homogeneous equations are given

$$m_d \ddot{x}_d - f_d = 0, \tag{5.5}$$

$$m\ddot{x} + kx + f_d = 0. \tag{5.6}$$

The solution of Eq. (5.5) and (5.6) is given as

$$x = A\sin\left(pt + \phi\right), \tag{5.7}$$

$$x_d = B\sin\left(pt + \phi\right). \tag{5.8}$$

Substitution of Eqs. (5.7) and (5.8) into Eqs. (5.5) and (5.6) produces the following algebraic equations that must be satisfied:

$$\left(k + k_d - p^2 m\right)A - k_d B = 0, \tag{5.9}$$

$$-k_d A + \left(k_d - p^2 m_d\right)B = 0. \tag{5.10}$$

Eqs. (5.9) and (5.10) can have nonzero solutions only if the determinant of the coefficients of A and B equal to zero. Thus

$$\begin{vmatrix} \left(k + k_d - p^2 m\right) & -k_d \\ -k_d & \left(k_d - p^2 m_d\right) \end{vmatrix} = 0 \quad . \tag{5.11}$$

Expansion of this determinant results in

$$mm_d p^4 - \left[mk_d + m_d \left(k + k_d \right) \right] p^2 + kk_d = 0 . \tag{5.12}$$

The expression in Eq. (5.12) is called the characteristic equation. The roots of this characteristic equation are the natural frequencies of vibration. These natural frequencies may be determined by quadratic formula

$$p_1^2 = \frac{\left(\omega^2 + \mu\omega_d^2 + \omega_d^2 \right) - \sqrt{\left(\omega^2 + \mu\omega_d^2 + \omega_d^2 \right)^2 - 4\omega^2\omega_d^2}}{2}, \tag{5.13}$$

$$p_2^2 = \frac{\left(\omega^2 + \mu\omega_d^2 + \omega_d^2 \right) + \sqrt{\left(\omega^2 + \mu\omega_d^2 + \omega_d^2 \right)^2 - 4\omega^2\omega_d^2}}{2}, \tag{5.14}$$

where

$$\omega_d = \sqrt{\frac{k_d}{m_d}} , \tag{5.15}$$

$$\omega = \sqrt{\frac{k}{m}} , \tag{5.16}$$

$$\mu = \frac{m_d}{m} . \tag{5.17}$$

Substituting the characteristic values p_1^2 and p_2^2 into the homogeneous algebraic equations (5.9) and (5.10) determining the shapes of the two natural modes of vibration (principal modes) by the amplitude ratios

$$r_1 = 1 - \left(\frac{p_1}{\omega_d} \right)^2 , \tag{5.18}$$

$$r_2 = 1 - \left(\frac{p_2}{\omega_d} \right)^2 . \tag{5.19}$$

The amplitude ratio in Eq. (5.18) and (5.19) depends only upon the physical constants m, m_d, k, and k_d. Using the smaller angular frequency p_1 and the corresponding amplitude ratio r_1 into Eqs. (5.7) and (5.8) yields

$$x' = r_1 B_1 \sin\left(p_1 t + \phi_1 \right), \tag{5.20}$$

$$x_d' = B_1 \sin\left(p_1 t + \phi_1 \right). \tag{5.21}$$

Expressions in Eqs. (5.20) and (5.21) completely describe the first mode of vibration, which is also called the fundamental mode. At any time during such motion, the displacement ratio is the same as the amplitude ratio r_1.

Substitution of the larger angular frequency p_2 and the corresponding amplitude ratio r_2 into Eqs. (5.7) and (5.8) yields

$$x'' = r_2 B_2 \sin\left(p_2 t + \phi_2\right), \tag{5.22}$$

$$x_d'' = B_2 \sin\left(p_2 t + \phi_2\right), \tag{5.23}$$

which describe the second mode of vibration. This simple harmonic motion of the two masses occurs at the angular frequency p_2 and displacement ratio is always r_2. The general solution of Eqs. (5.5) and (5.6) consists of the sum of the principal mode solutions in Eqs. (5.20)-(5.23).

$$x = x' + x'' = r_1 B_1 \sin\left(p_1 t + \phi_1\right) + r_2 B_2 \sin\left(p_2 t + \phi_2\right), \tag{5.24}$$

$$x_d = x_d' + x_d'' = B_1 \sin\left(p_1 t + \phi_1\right) + B_2 \sin\left(p_2 t + \phi_2\right). \tag{5.25}$$

The relative velocity between mass m and m_d can be written as

$$\dot{x} - \dot{x}_d = r_1 B_1 p_1 \cos\left(p_1 t + \phi_1\right) + r_2 B_2 p_2 \cos\left(p_2 t + \phi_2\right)$$

$$-\left[B_1 p_1 \cos\left(p_1 t + \phi_1\right) + B_2 p_2 \cos\left(p_2 t + \phi_2\right)\right], \tag{5.26}$$

or

$$\dot{x} - \dot{x}_d = \underbrace{B_1 p_1 \cos\left(p_1 t + \phi_1\right)\left(r_1 - 1\right)}_{mode\ 1} + \underbrace{B_2 p_2 \cos\left(p_2 t + \phi_2\right)\left(r_2 - 1\right)}_{mode\ 2}. \tag{5.27}$$

Equation (5.27) indicates that the relative velocity between m and m_d is summation of the relative velocity of each vibration mode.

In the real application of impact damper the frequency ratio ω/ω_d should be as small as possible to obtain maximum transfer of energy. Substitution of the small value of ω/ω_d into Eq. (5.13) will result the quadrate of frequency ratio $(p_1/\omega_d)^2 \approx 0$. Application this value into Eq. (5.18) resulted that

$$r_1 = 1 - \left(\frac{p_1}{\omega_d}\right)^2 = 1 - 0 = 1. \tag{5.28}$$

Substitution the result of Eq. (5.28) into Eq. (5.27), indicates that the relative velocity for impact damper application is only determined by relative velocity component of the

second mode of vibration.

Integration of Eq. (5.1)-(5.4) was carried in MatLab/Simulink by using the fifth-order Dormand-Prince method with variable time steps. During simulation, the acceleration ratio of mass m with using impact damper and without using impact damper is calculated. This ratio represents the amount of energy absorbed by mass m.

Fig. 5.2 shows the variation of maximum acceleration of mass m with frequency ratio ω_d/ω_w for $\omega = 0$. a and a_0 are the maximum of acceleration obtained with and without using impact damper, respectively. The acceleration ratio is decreasing with increasing in mass ratio.

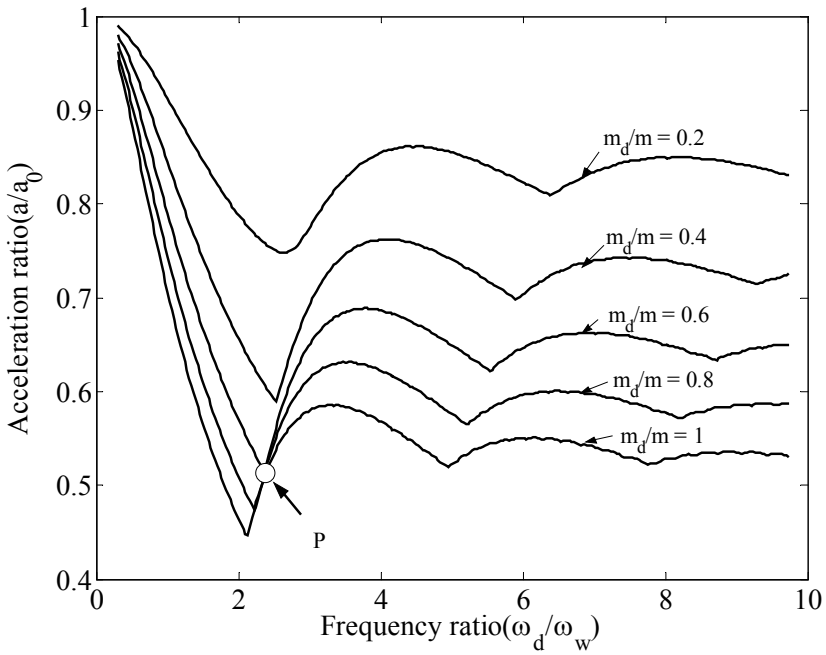

Fig. 5.2 Acceleration ratio of mass m.

Figure 5.3 shows time responses obtained for case mass ratio $m_d/m = 0.6$. When the damper operating at minimum peak of acceleration (point P), the relative velocity is equal to zero at the time maximum impact force f_w. From this result, it can be concluded that the location of minimum peak of acceleration could be calculated at the time of zero relative velocity. Regarding to Eq. (5.27), the relative velocity in the case of impact damper could be obtained using only the response of the 2nd mode of vibration.

Figure 5.4 shows the equivalent one-degree of freedom model of the system using only the 2nd mode of vibration. m_2 and k_2 are the modal mass and modal stiffness of the 2nd mode. The relation between m_2 and k_2 is expressed as

$$k_2 = m_2 p_2^2 = m_2 \frac{\left(\omega^2 + r_d\omega_d^2 + \omega_d^2\right) + \sqrt{\left(\omega^2 + r_d\omega_d^2 + \omega_d^2\right)^2 - 4\omega^2\omega_d^2}}{2} \tag{5.29}$$

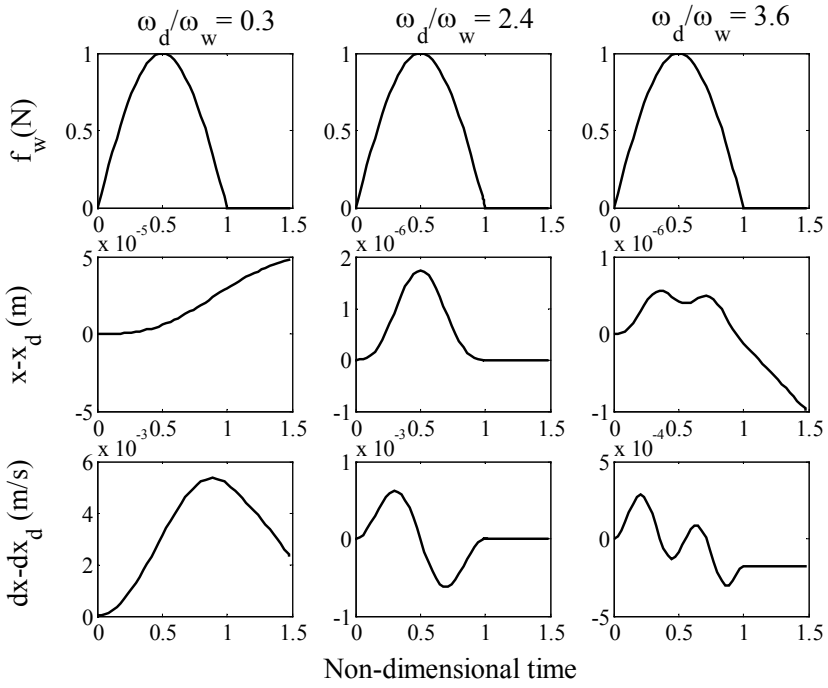

Fig. 5.3 Time history for $m_d/m = 0.6$.

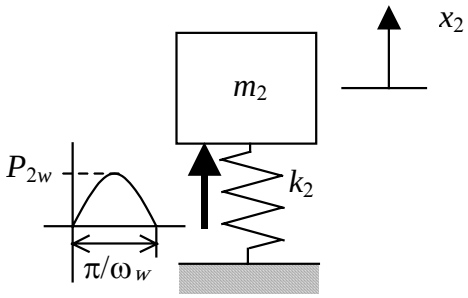

Fig. 5.4 One degree of freedom equivalent model.

The equation of motion of one degree of freedom (DOF) system in Fig. 5.4 can be written as

$$m_2\ddot{x}_2 + k_2 x_2 = P_{2w}\sin\omega_w t\,, \quad t \le \frac{\pi}{\omega_w}\,. \tag{5.30}$$

The displacement response of m_2 with initial condition $x_2(0)=0$ and $dx_2(0)/dt = 0$ is

$$x_2 = \frac{P_{2w}/k_2}{1-\left(\frac{\omega_w}{p_2}\right)^2}\left(\sin\omega_w t - \frac{\omega_w}{p_2}\sin p_2 t\right). \tag{5.31}$$

and the velocity response is obtained by differentiating Eq. (5.31) resulted

$$\dot{x}_2 = \frac{P_{2w}/k_2}{1-\left(\frac{\omega_w}{p_2}\right)^2}\omega_w\left(\cos\omega_w t - \cos p_2 t\right). \tag{5.32}$$

It should be noted that the response of the system in Eq. (5.32) consists of two components. The first component is relating to free vibration response with frequency p_2 and the second one is relating to force vibration response with frequency ω_w. When the zero velocity of the system response occurs at the same time as the maximum excitation force, the transfer of energy will maximum. The zero velocity response occurs at the time

$\dot{x}_2 = 0$,

$$\frac{P_{2w}/k_2}{1-\left(\frac{\omega_w}{p_2}\right)^2}\omega_w\left(\cos\omega_w t - \cos p_2 t\right) = 0. \tag{5.33}$$

The term in the bracket can be written as

$$\cos\omega_w t - \cos p_2 t = -2\sin\frac{(\omega_w + p_2)t}{2}\sin\frac{(\omega_w - p_2)t}{2}. \tag{5.34}$$

Substituting Eq. (5.34) into Eq. (5.33) resulting

$$(\omega_w \pm p_2)t = n\pi \quad , \tag{5.35}$$

$$t_2 = \frac{n\pi}{\omega_w + p_2} \quad . \tag{5.36}$$

where $n = 0, \pm 1, \pm 2, \cdots$ and $\omega_w > 0$, $p_2 > 0$ and $\omega_w \neq p_2$.

From Fig. 5.4, the maximum of excitation force occurs when

$$t_w = \frac{\pi}{2\omega_w}. \tag{5.37}$$

The maximum of transfer of energy occurs if $t_2 = t_w$ so that

$$\frac{n\pi}{\omega_w + p_2} = \frac{\pi}{2\omega_w}. \tag{5.38}$$

Because of $\omega_w > 0$, $p_2 > 0$ and $\omega_w \neq p_2$, the maximum transfer of energy can be obtained

by choosing $n = 2$. By inserting $n = 2$ into Eq. (5.38), yields

$$p_2 = 3\omega_w . \tag{5.39}$$

Substituting p_2 in Eq. (5.14) into Eq. (5.39), yields

$$\beta^2 + \gamma^2(\mu+1) + \sqrt{\left(\beta^2 + \gamma^2(\mu+1)\right)^2 - 4\beta^2\gamma^2} = 18, \tag{5.40}$$

where

$$\gamma = \frac{\omega_d}{\omega_w}, \tag{5.41}$$

$$\beta = \frac{\omega}{\omega_w}. \tag{5.42}$$

Solution of Eq. (5.40) for γ is given by

$$\gamma = \sqrt{\frac{9\left(9-\beta^2\right)}{9(\mu+1)-\beta^2}}. \tag{5.43}$$

In the real impact case between boat and wave, the boat motion is dominated by the rigid body mode of vibration with zero natural frequency because the excitation force from the wave acts uniformly in the whole surface of the boat bottom part. Considering this fact, then

$$\omega = 0 \rightarrow \beta = 0, \tag{5.44}$$

$$\gamma = 3\sqrt{\frac{1}{\mu+1}}. \tag{5.45}$$

The location of minimum peak of maximum acceleration is shown in Fig. 5.5. This figure shows that for mass ratio greater than 0.3 the result obtained from the simulation of Eq. (5.1)-(5.4) is almost the same with the optimal result calculated in Eq. (5.45). This may be resulted from the assumption of $(p_1/\omega_d)^2 \approx 0$ as in Eq. (5.28) which is no longer valid for mass ratio less than 0.3.

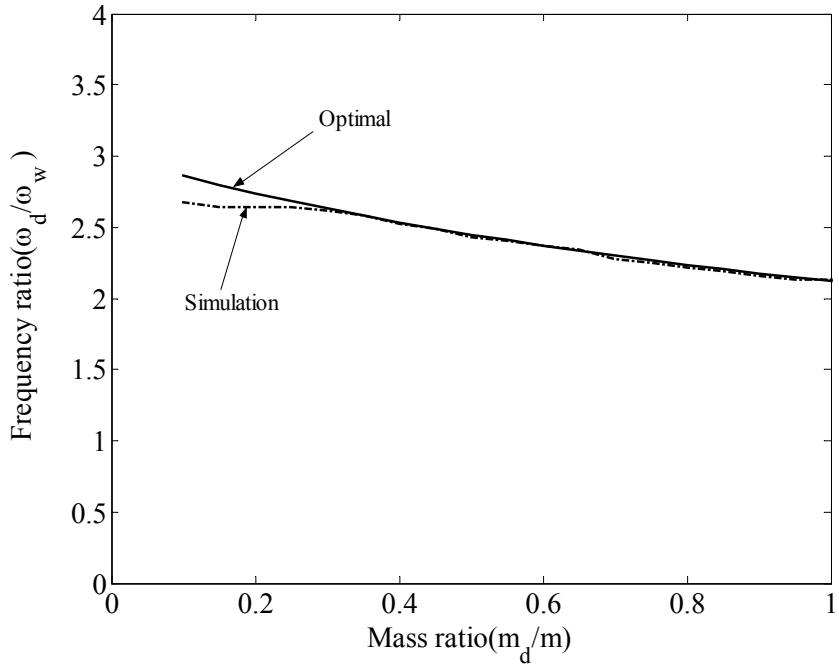

Fig. 5.5 Optimal value of contact parameter.

5.3 Laboratory Model

5.3.1 Pinned Beam Model

Figure 5.6 shows the pinned beam model of boat with impact damper. The wave force and impact damper force act at the center of the beam. The wave is modeled using mass-spring system with mass m_w and stiffness k_w. In the initial condition the beam has initial angular velocity ω_0. This initial condition is obtained by releasing the beam from a predetermined angular displacement. The contact condition between beam and m_w is modeled using contact spring with stiffness K_w. The impact damper is modeled using mass m_d, which is contacting to beam with contact stiffness K_d.

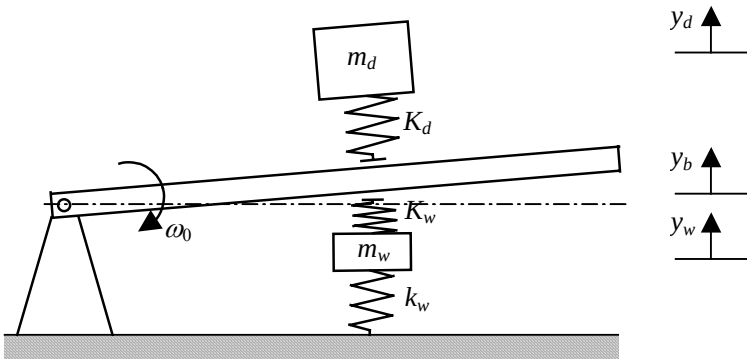

Fig. 5.6 Laboratory model of impact of boat.

The governing equations of motion are expressed as

$$\rho A\frac{\partial^2 y_b}{\partial t^2}+EI\frac{\partial^4 y_b}{\partial x^4}=\sum f_i\delta\left(x-x_i\right), \tag{5.46}$$

$$m_d\ddot{y}_d-f_d=0, \tag{5.47}$$

$$m_w\ddot{y}_w+f_w+k_w y_w=0. \tag{5.48}$$

where E is Young modulus, A is the cross section of area, I is the second order moment, δ is delta function and f_d and f_w are the contact force between beam and both m_d and m_w, respectively. The contact forces are given by

$$f_d=\begin{cases}K_d\left(y_b-y_d\right), & for\ y_b-y_d\geq 0\\ 0, & for\ y_b-y_d<0\end{cases}, \tag{5.49}$$

$$f_w=\begin{cases}K_w\left(y_w-y_b\right), & for\ y_w-y_b\geq 0\\ 0, & for\ y_w-y_b<0\end{cases}. \tag{5.50}$$

Lateral vibration of the beam can be given by summation of the mass normalized eigenfunctions $\psi_r(x)$ as

$$y_b\left(x,t\right)=\sum_{r=0}^{\infty}\psi_r\left(x\right)q_r\left(t\right), \tag{5.51}$$

where

$$\psi_0=\frac{\sqrt{3}}{\sqrt{\rho AL^3}}x, \tag{5.52}$$

$$\psi_r=\alpha_r\left(\sinh p_rL\sin p_rx+\sin p_rL\sinh p_rx\right),\quad (r=1,\cdots,\infty) \tag{5.53}$$

$$\alpha_r=\left\{\sinh^2 p_rL\left(\frac{L}{2}-\frac{\sin 2p_rL}{4p_i}\right)+\sin^2 p_rL\left(-\frac{L}{2}+\frac{\sinh 2p_rL}{4p_r}\right),\right.$$

$$\left.+\frac{1}{p_r}\sin p_rL\sinh p_rL\left(\sin p_rL\cosh p_rL-\cos p_rL\sinh p_rL\right)\right\}^{-1},\quad (r=1,\cdots,\infty). \tag{5.54}$$

and q_r is the general coordinate. ψ_0 represents the non-vibrational rigid body rotational motion. The variable p_r are obtained by solving the explicit equation

$$-\sin p_rL\cosh p_rL+\cos p_rL\sinh p_rL=0,\quad (r=1,\cdots\infty). \tag{5.55}$$

By substituting Eq. (5.51) for y_b and using the orthogonality of the eigenfunctions, the differential equation of motion Eq. (5.46) can be written as

$$\ddot{q}_r + \omega_r^2 q_r = \psi_r(x_i)\, f_i(t), \tag{5.56}$$

where ω_r is the natural frequency given by

$$\omega_0 = 0, \tag{5.57}$$

$$\omega_r^2 = \frac{EI}{\rho A} p_r^4 \quad , (r = 1, \cdots, \infty). \tag{5.58}$$

The simulation parameters were shown in Table 5.1. Only the rigid body mode and five lower elastic mode were considered in this simulation.

Table 5.1 Simulation parameters.

Damper	mass m_d	12～120g
	Stiffness K_d	1.0×10^5～7.0×10^7 N/m
Beam	size	$400\times35\times3\text{mm}^3$
	mass m_b	120 g
	flexural rigidity EI	5.9Nm^2
	natural frequencies	0, 68.0, 220.4, 459.9, 786.4, 1200 Hz
Wave	mass m_w	22 g
	Stiffness K_w	2.5×10^5～4.9×10^5 N/m
	Stiffness k_w	3100 N/m
	Angular speed ω_0	0.70 rad/s

Figure 5.7 shows mode shapes of the boat model. These figures show that nodal point at the 2nd and 4th mode is located close to point $L/2$. It means that only the rigid mode, 1st, 3th and 5th mode have dominant contribution in transfer the energy during collision.

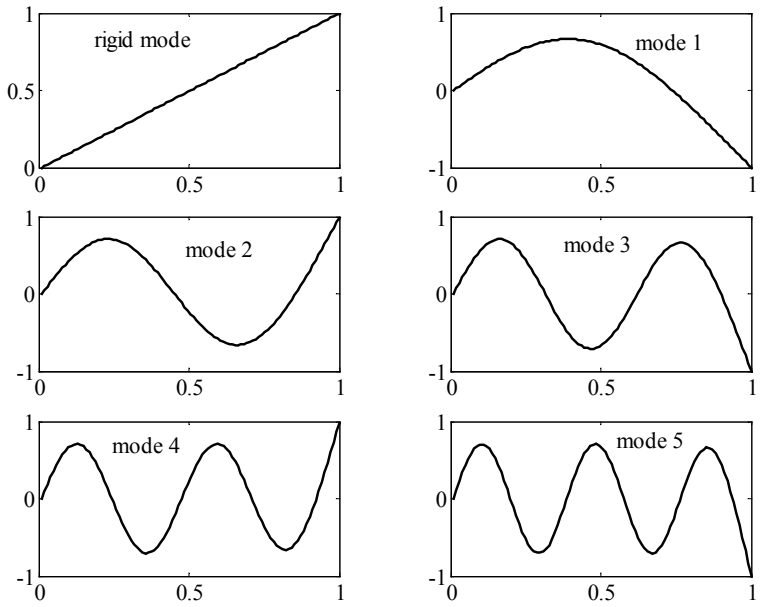

Fig. 5.7 Mode shape of beam.

Figure 5.8 shows the simulation result of beam energy variation. ω_1 is the natural frequency of first elastic mode and ω_w and ω_d denote the contact frequencies between beam and both m_w and m_d which are given by

$$\omega_w = \sqrt{\frac{K_w}{m_w}}, \tag{5.59}$$

$$\omega_d = \sqrt{\frac{K_d}{m_d}}. \tag{5.60}$$

The energy of beam is calculated as follows

$$E = E_o - \frac{1}{2} m_w v_{w+}^2 - \frac{1}{2} m_d v_{d+}^2, \tag{5.61}$$

where E_0, v_{w+} and v_{d+} is the initial energy of beam and damper before collision and velocity of m_w and m_d after collision, respectively.

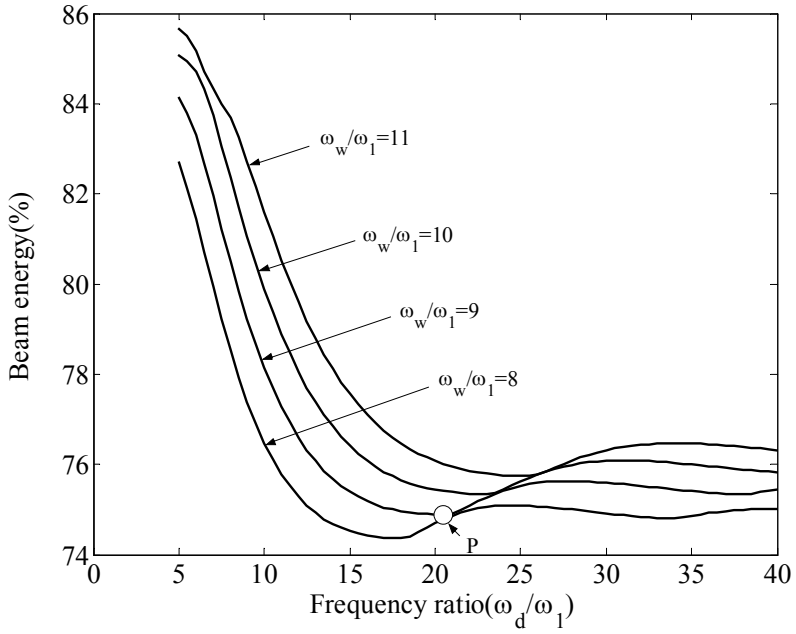

Fig. 5.8 Beam energy variation.

Figure 5.9 shows a set of time history of the response for $\omega_w/\omega_1=9$. This figure shows that the kinetic energy of m_d is independent from variation of ω_d. Conversely, the kinetic energy of m_w is influenced by variation of ω_d. The minimum energy of beam is obtained when the kinetic energy of m_w is maximum.

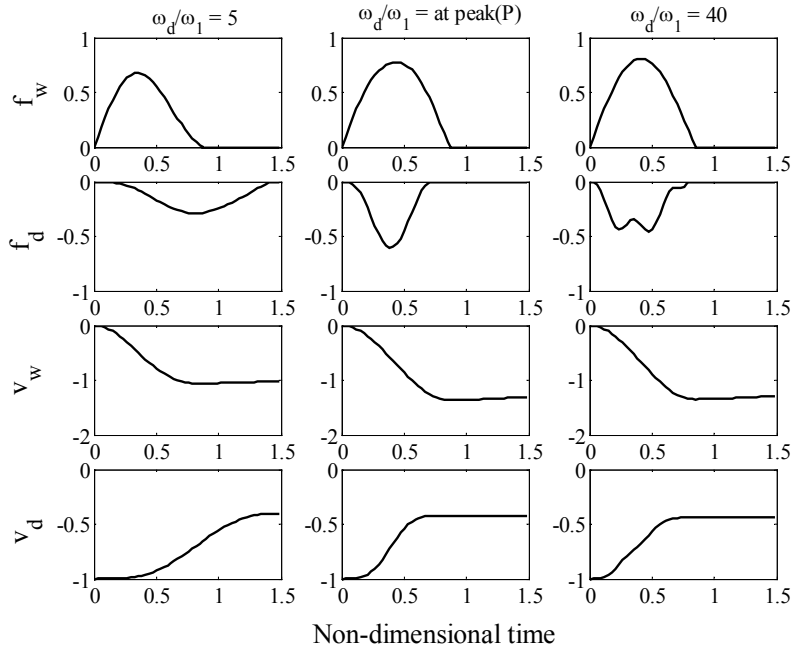

Fig. 5.9 Time history for $\omega_w/\omega_1=9$.

The energy profiles of beam vibration mode during collision are depicted in Fig. 5.10-5.13. Figure 5.10 shows the energy of beam without impact damper. In this figure only the elastic mode of vibration is shown because the energy component of beam rigid body mode is very large (more than 80% of the total energy) compared with the energy of its elastic mode. The contact time between m_w and beam is about 0.6 ms. The energy of each vibration mode is almost constant after contact time. Figure 5.10 shows that the energy portion of the 1st mode and 3rd mode are almost 4% and 5% of the total energy. The energy portion of the 2nd and the 4th mode are less than 1% of the total energy.

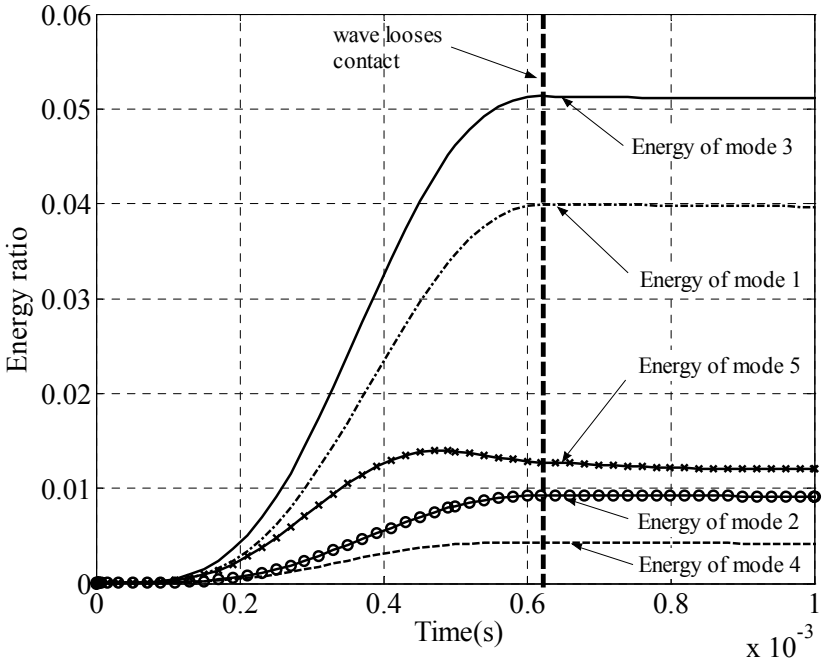

Fig. 5.10 Energy profile of beam mode shape without impact damper with $\omega_w/\omega_1=9$.

Fig. 5.11 show the energy profile with $\omega_w/\omega_1=9$ and $\omega_d/\omega_1=5$. Comparing to the case without impact damper in Fig. 5.10, the energy of 1st mode and 3rd mode are reduced to 0.7 % and 3.6 % after collision. The energy of 5th mode does not change significantly during collision.

The energy profile in the position of minimum peak of energy with $\omega_w/\omega_1=9$ (point P) is shown in Fig. 5.12. The reduction of total energy in this case is larger than the case without impact damper in Fig. 5.10 and with impact damper case for $\omega_d/\omega_1=5$ in Fig. 5.11. As can be seen from Fig. 5.12, for the 1st , 3rd and 5th modes, the energy decreases to 2%, 2.2% and 0.17%, respectively.

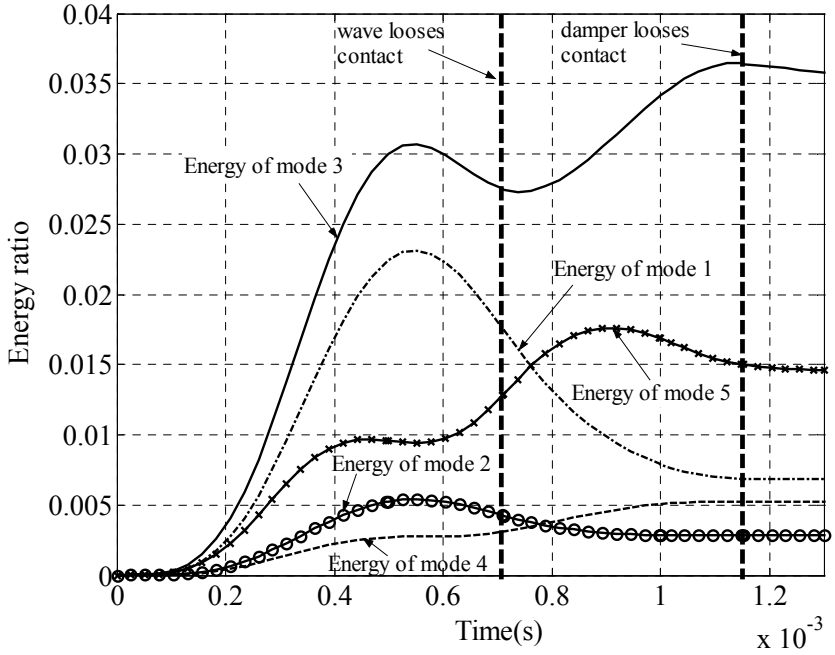

Fig. 5.11 Energy profile of beam mode shape with ω_w/ω_1=9 and ω_d/ω_1=5.

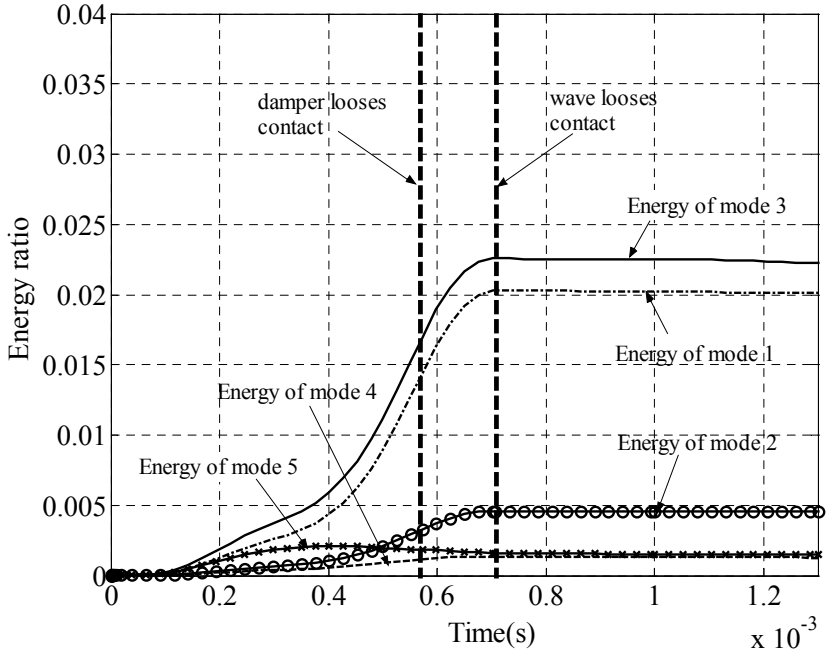

Fig. 5.12 Energy profile of beam mode shape with ω_w/ω_1=9 and ω_d/ω_1=5 at point P.

Figure 5.13 shows the energy profile with ω_w/ω_1=9 and ω_d/ω_1=40. For the 1st, 2nd, 3rd and 4th modes, the decreasing of energy obtained in this case are almost the same with the case in Fig. 5.12. However, for the 5th mode, the decreasing of energy is smaller compared to the case in Fig. 5.12.

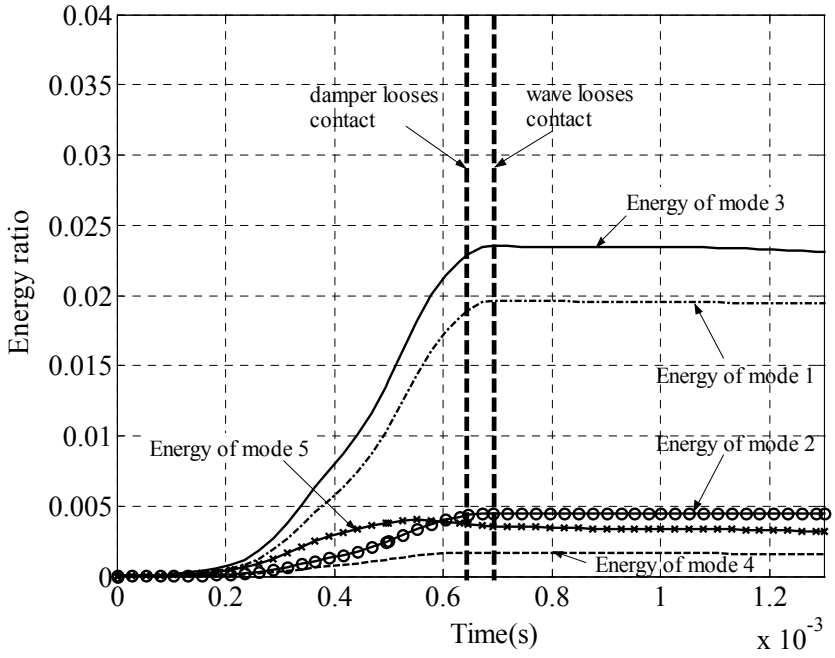

Fig. 5.13 Energy profile of beam mode shape with ω_w/ω_1=9 and ω_d/ω_1=40.

Figure 5.14 shows variation of beam energy with mass ratio. In the simulation, the contact frequency ω_w is kept constant as $\omega_w = 4.7\times 10^3$ N/m and variable ω_d is varied within the range $\omega_d \in [2.1\times 10^3, 1.7\times 10^4]$. The increasing in mass ratio of impact damper significantly reduces the energy of the beam.

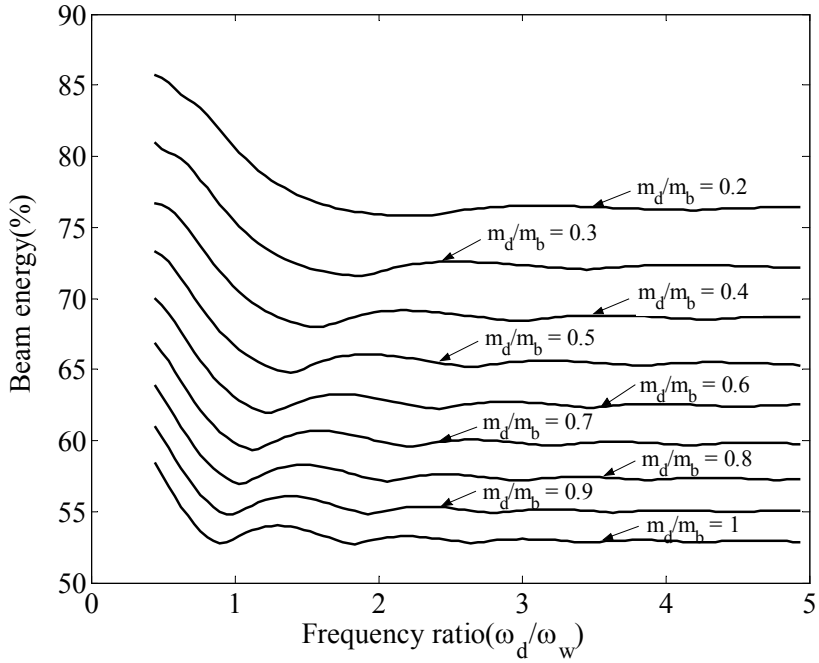

Fig. 5.14 Beam energy for $\omega_w = 4.7 \times 10^3$ N/m.

Figure 5.15 shows variation of frequency ratio with mass ratio in the location of minimum beam energy. The two minimum lines in Fig. 5.15 are plotted from the data of minimum beam energy in Fig. 5.14 in the frequency range $0<\omega_d/\omega_w<5$.

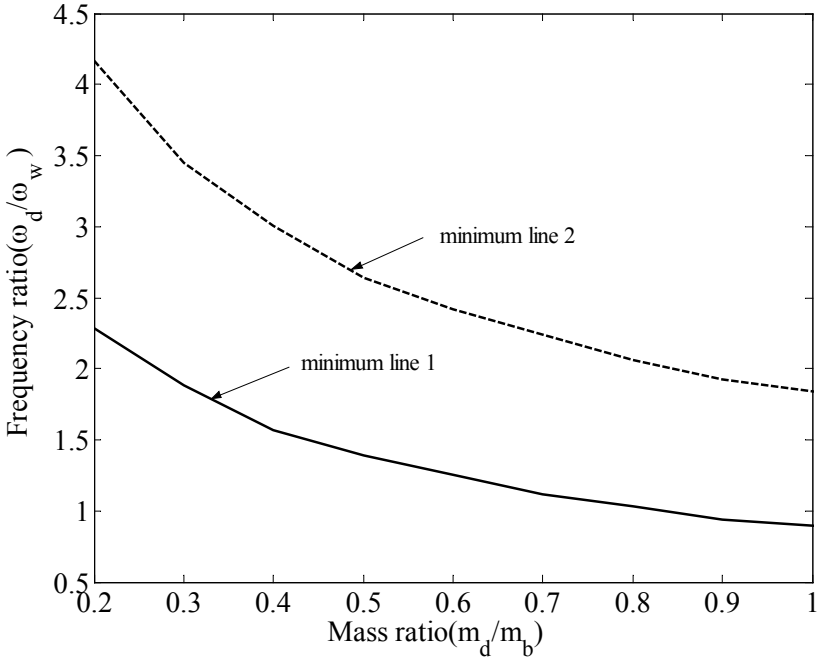

Fig. 5.15 Variation of minimum beam energy.

The acceleration response of the beam at the free end of beam for different mass ratio is depicted in Fig. 5.16. In this simulation $K_w=5\times 10^5$ N/m and the contact stiffness K_d are calculated using Eq. (5.45).

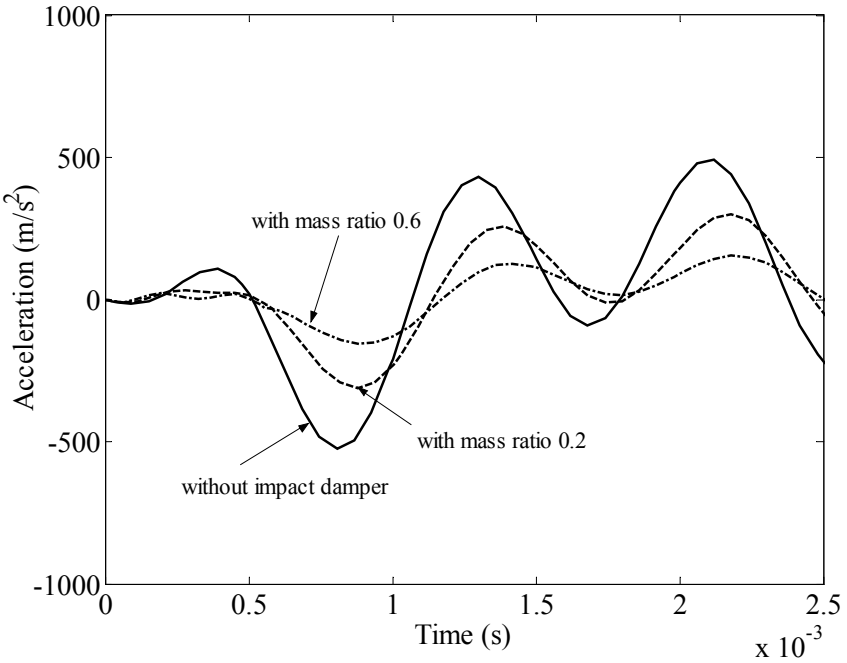

Fig. 5.16 Acceleration response for $K_{cw}=5\times 10^5$ and K_d calculated from Eq. (5.45).

Comparison of acceleration response obtained using impact damper and conventional added mass method is shown in Fig. 5.17. In this simulation, the added mass is located in the impact damper position with same mass ratio as impact damper mass. This figure shows that for the same mass ratio, the impact damper method has better performance in reducing the peak of acceleration compare to added mass method.

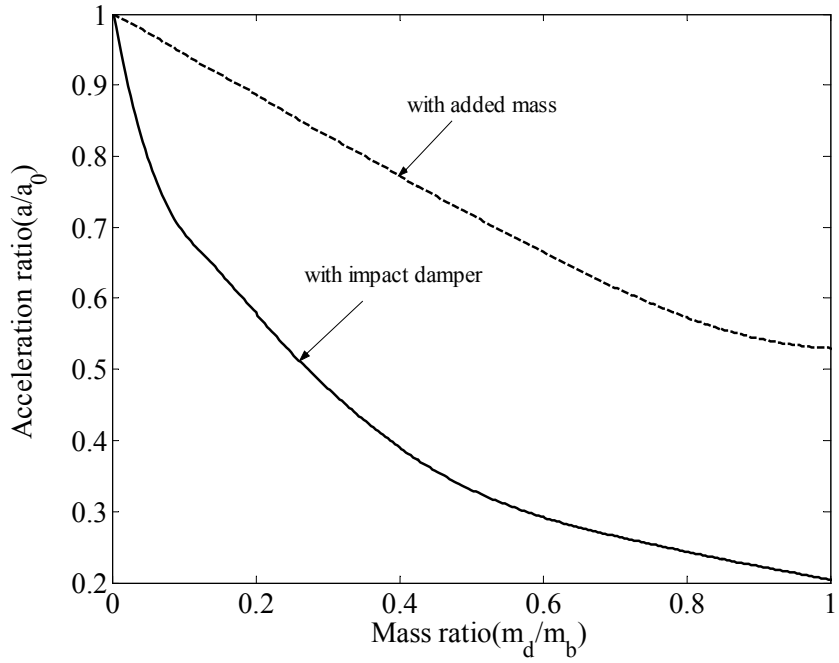

Fig. 5.17 Comparison between impact damper and added mass method.

5.3.2 Small Scale Boat Model

Figure 5.18 shows the small-scale model of the real boat used for the simulation. The size of this boat model is about 1/15 of the real boat size. The boat model is made of urethane foam with length of 0.45 m.

Fig. 5.18 The small scale model of the boat.

The model of the small-scale boat with impact damper is shown in Fig. 5.19. The boat is modeled using the finite element method (FEM) using ANSYS software. The damper is modeled as rigid body system. The wave is modeled as distributed water pressure acting on the bottom of the boat.

The equations of motion for the boat, damper and wave are written as

$$\mathbf{M_b}\ddot{\mathbf{X}}_\mathbf{b} + \mathbf{C_b}\dot{\mathbf{X}}_\mathbf{b} + \mathbf{K_b}\mathbf{X_b} = \sum_{h=1}^{H} \mathbf{B}_{w,\mathbf{h}} f_{w,h} - \mathbf{B_d} F_d \tag{5.62}$$

$$m_d \ddot{z}_d = F_d \tag{5.63}$$

where matrix $\mathbf{M_b}$, $\mathbf{C_b}$, and $\mathbf{K_b}$ are the boat mass matrix, damping matrix and stiffness matrix, respectively, while $f_{w,h}$, F_d and m_d are the contact force between wave and boat, contact force between boat and impact damper and mass of impact damper, respectively. Vector $\mathbf{X_b}$ and z_d are displacement vector of boat and displacement of impact damper, respectively. $\mathbf{B_{w,h}}$ and $\mathbf{B_d}$ are vector that show the position of the external force.

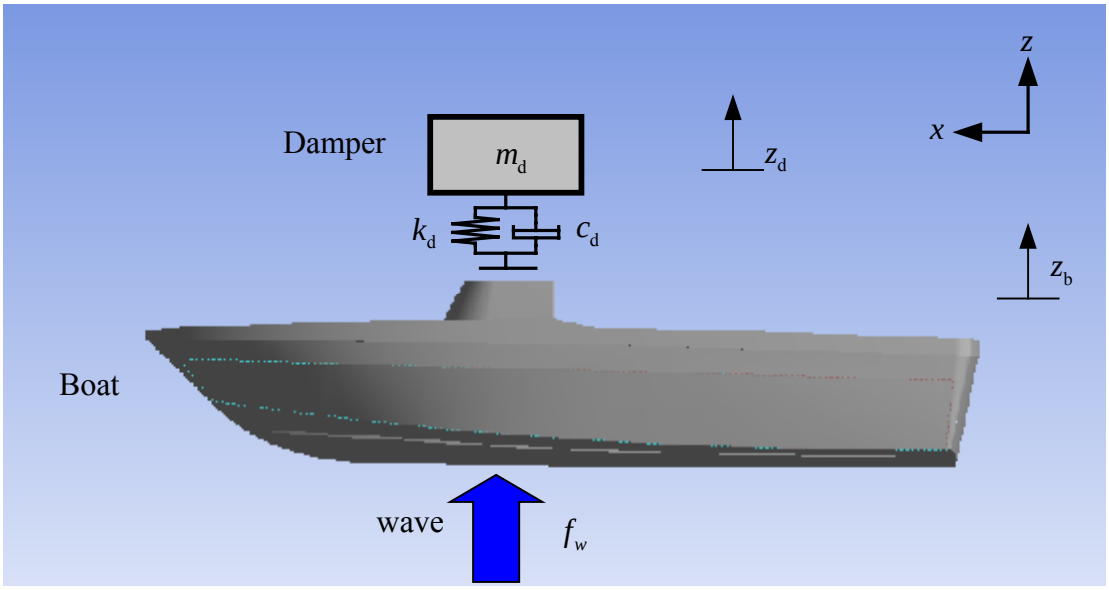

Fig. 5.19 Small scale boat and impact damper model.

The contact force between wave and the boat is given by

$$f_{w,h}(t) = \begin{cases} F_w \sin \omega_w t\ , & for\ \ 0 \le t \le \dfrac{\pi}{\omega_w} \\ 0\ , & for\ t > \dfrac{\pi}{\omega_w} \end{cases} \tag{5.64}$$

Figure 5.20 shows the location of contact force between wave and the boat. As can be seen from Fig. 5.20, the contact force is distributed along contact area between water and the boat.

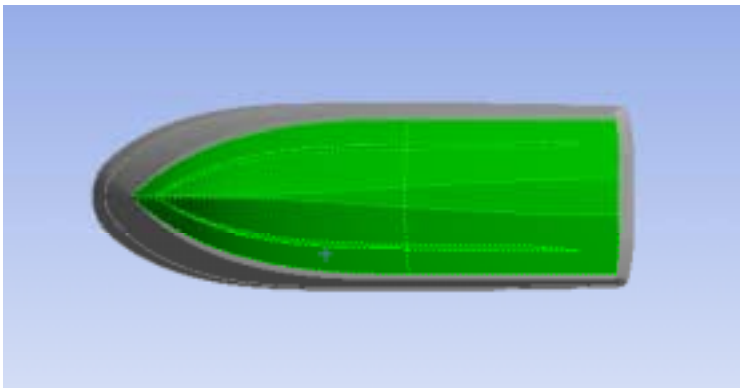

Fig. 5.20 Contact area between boat and water.

The contact force between boat and impact damper was modeled using a linear spring and dashpot

$$F_d = -k_d\left(z_d - z_b\right) - c_d\left(\dot{z}_d - \dot{z}_b\right) \tag{5.65}$$

where k_d, c_d, z_d and z_b are contact stiffness and damping coefficient between impact damper and the boat, displacement of damper and displacement of boat at the contact point with impact damper, respectively. The location of contact point between impact damper mass and the boat is denoted as point B as described in Fig. 5.21.

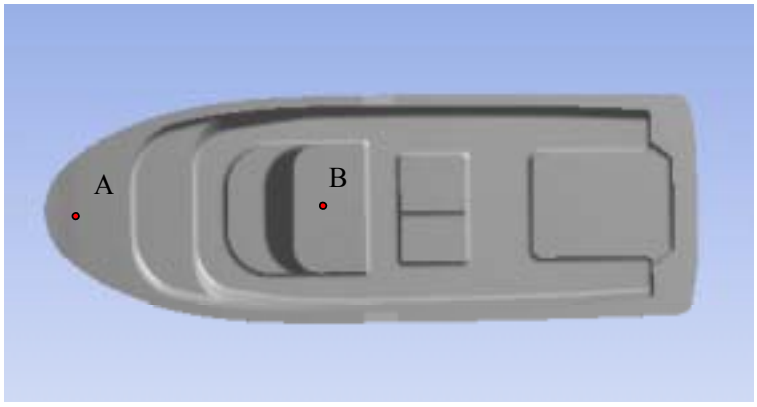

Fig. 5.21 Location of impact damper.

Figure 5.22 shows four lowest vibration modes of the boat without impact damper. The first and the second elastic mode at frequency 293 Hz and 388 Hz are relating to the bending mode and torsional mode of the boat, respectively.

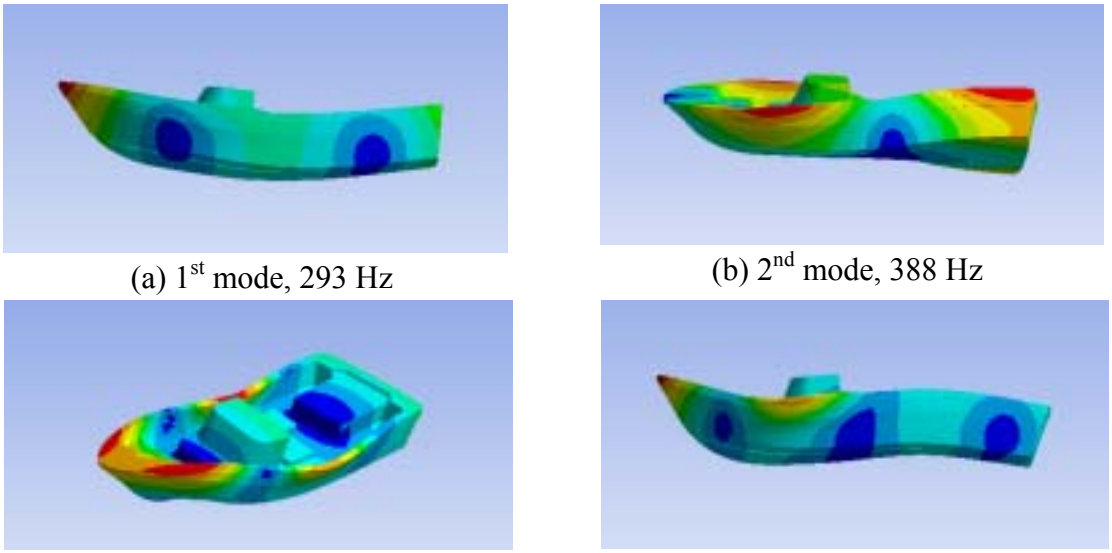

(a) 1st mode, 293 Hz (b) 2nd mode, 388 Hz

(c) 3rd mode, 628 Hz (d) 4th mode, 666 Hz

Fig. 5.22 Four lowest mode of the boat.

The acceleration is calculated at the front end of the boat (point A in Fig. 5.21). Simulation result of the acceleration ratio with variation of the frequency ratio (ω_d/ω_w) and mass ratio ($\mu = m_d/m$) is shown in Fig. 5.23. Here, ω_d and m are contact frequency between boat and impact damper and mass of the boat, respectively. The increasing in mass ratio of impact damper significantly reduces the acceleration of the boat.

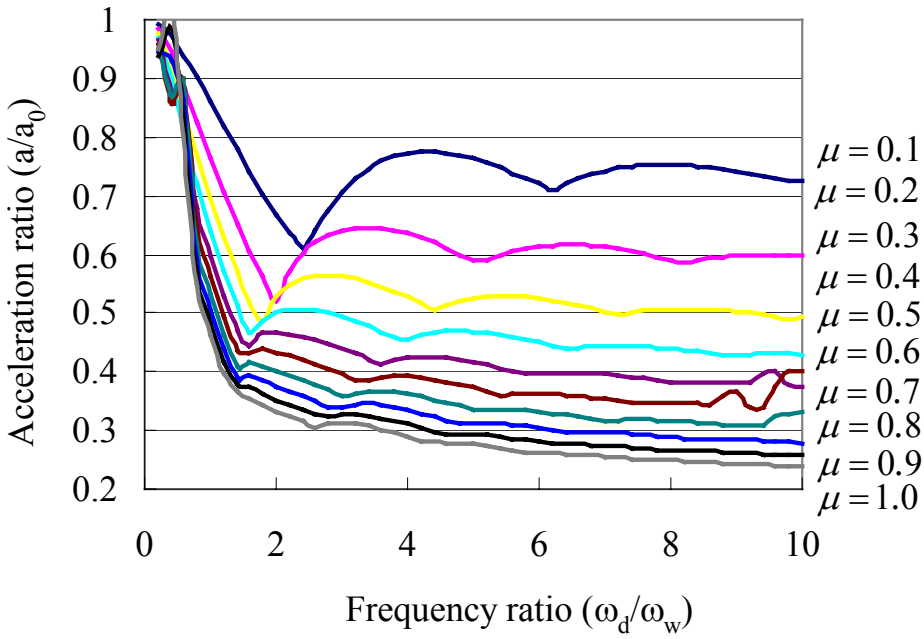

Fig. 5.23 Acceleration ratio of the boat.

5.4 Experiment

5.4.1 Pinned Beam Model

The experimental setup is shown in Fig. 5.24. The beam is made of an aluminum plate. The impact damper mass (m_d) and wave mass (m_w) are made of steel ball. The initial angular speed of the beam and impact damper is 0.70 rad/s. This initial speed is very slow so that the contact damping between beam and both m_w and m_d can be neglected. The contact stiffness is calculated by reconciling the impact response from experiment with the simulation.

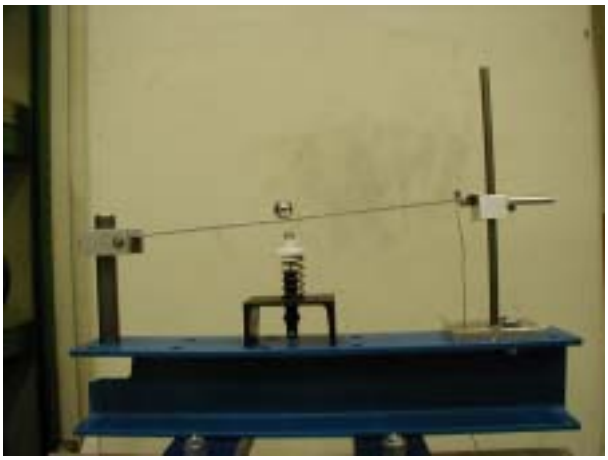

Fig. 5.24 Experimental setup beam and ball.

Comparison of frequency response function (FRF) obtained from the experiment and the simulation result is shown in Fig. 5.25. In the experiment, the transfer function is calculated from the data obtained from impact testing using impact hammer.

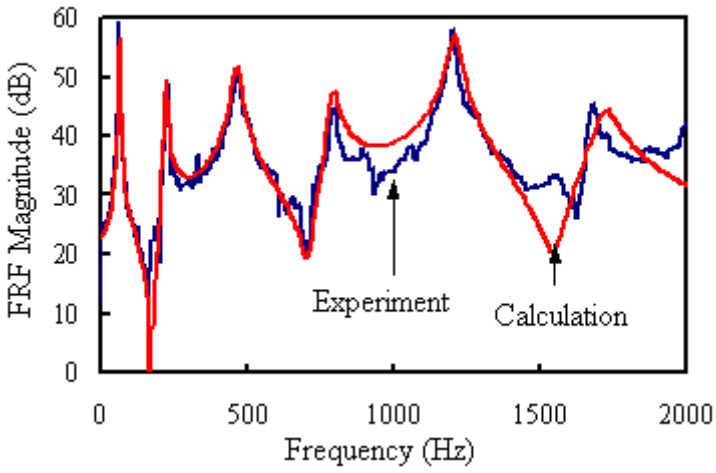

Fig. 5.25 Comparison between experiment and calculation result of transfer function.

Comparison of response system obtained from the experiment and the simulation are shown in Fig. 5.26. The parameter values for the simulation are depicted in Table 5.2. Figure 5.26 shows that the simulation result is good enough in simulating the experimental data. The decreasing in peak amplitude obtained from the experiment is also showed in the simulation result.

Table 5.2 Simulation parameters for response calculation.

Wave stiffness, K_w (N/m)	3.0×10^5

	$\mu=0.1$	$\mu=0.2$	$\mu=0.4$
Impact damper stiffness, K_d (N/m)	1.0×10^5	5.0×10^5	1.0×10^6

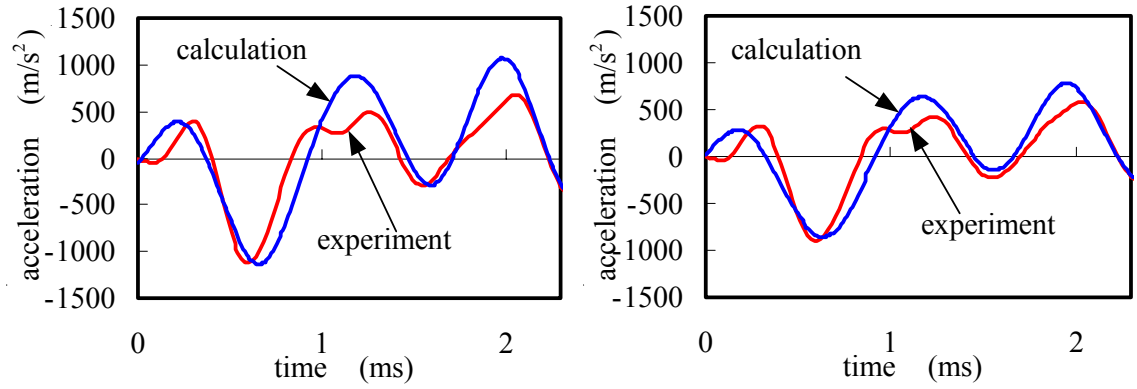

(a)without damper (b)with damper mass ratio 0.1

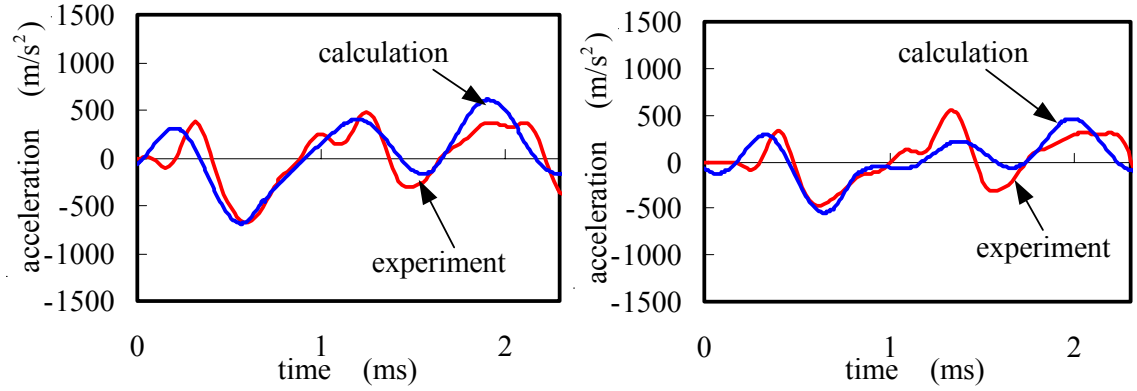

(c) with damper mass ratio 0.2 (d)with damper mass ratio 0.4

Fig. 5.26 Acceleration response of pinned beam model.

5.4.2 Small Scale Boat Model

The experimental study was conducted to the small-scale model of the boat in order to validate the simulation result. The length of this boat model is 0.45 m. The response of the boat is measured using an accelerometer. The measurement point is located at point A as shown in Fig. 5.21. The schematic of the experimental setup is shown in Fig. 5.27.

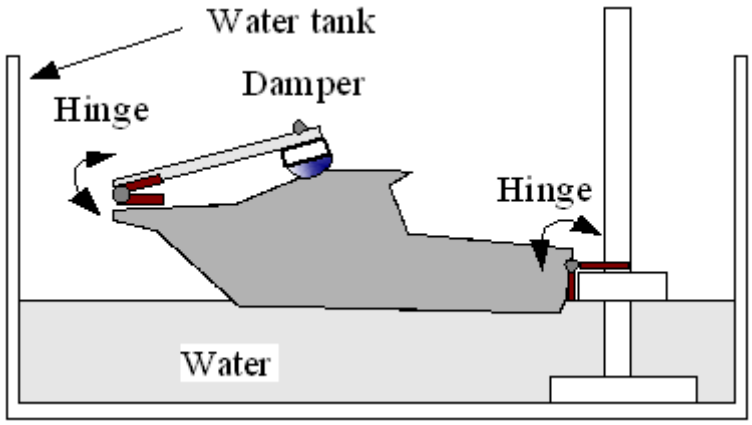

Fig. 5.27 Experimental setup of the boat.

A comparison between simulation result and experimental result of the boat acceleration ratio is shown in Fig. 5.28. This figure shows that the theoretical models are reliable to simulate the experimental result.

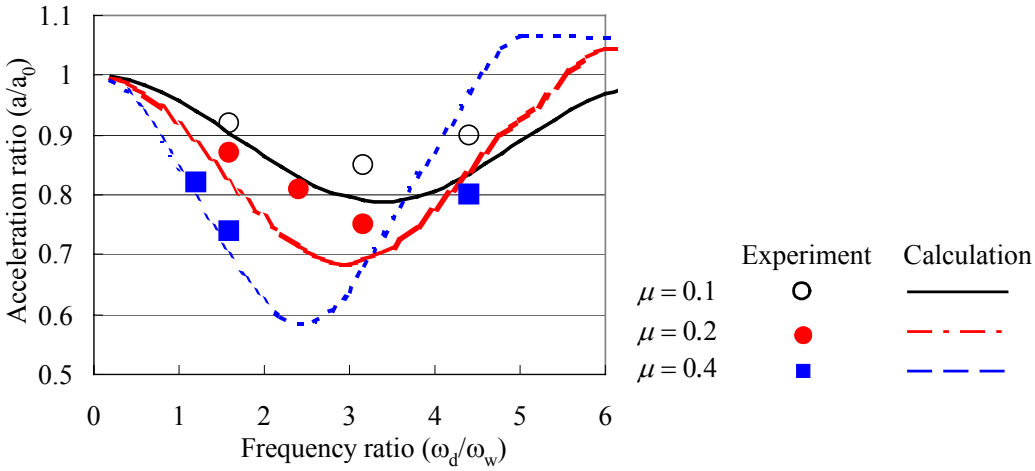

Fig. 5.28 Comparison between simulation and experimental result.

5.5 Summary

The two-degree of freedom model was developed to obtain the optimal impact damper parameter for boat application. It was shown that the contact frequency ratio depended

on the mass ratio between impact damper and boat. The transfer of energy analysis was conducted to pinned beam and ball model of boat impact. The dominant transfer of energy was mainly contributed by 1st, 3rd and 5th beam elastic modes of vibration. As the result, the optimal impact damper parameter developed for two degree of freedom model has a little difference compare to the optimal parameter calculated from the pinned beam model.

The simulation and experimental study was conducted to the small-scale model of the boat. The acceleration ratio obtained from this boat model almost the same as the acceleration ratio obtained using two degree of freedom model. As shown in the simulation and experimental result, the acceleration ratio decreases when the mass ratio increases.

Chapter 6
CONCLUSION

6.1 Summary

This research proposed a novel momentum exchange impact damper (MEID) for controlling impact induced vibration in machine and structures. Typically, MEID has provided excellent solutions in many impact problems because it can reduce the first transient wave generated by impulsive force. This study evaluated this new absorber, assessing its dynamic performance both numerically and experimentally.

The first phase of this study was evaluating the three-body collision problems consisted of impact mass, main body and absorber mass in which optimal parameter of MEID were calculated. Two configurations of three-body collision were evaluated. In the first configuration the main body was modeled as a single degree of freedom (SDOF) system. The transfer of energy from impact mass to the absorber mass depended strongly on the natural frequency of the main body and the contact frequencies between main body and both impact mass and absorber mass. It was shown from the simulation that the maximum transfer of energy was obtained when the two contact frequencies were the same. Moreover, the transfer of energy was increased if the natural frequency of main body was much smaller than the contact frequency. On the second configuration, the main body was an elastic rod. In contrast to the first configuration, the elastic rod has many elastic modes of vibration and these modes has contribution to the transfer of energy during collision. The simulation result showed that the maximum transfer of energy for this case was obtained if the two contact frequencies were almost the same. In addition, by using the same mass ratio between absorber mass and main body, the transfer of energy obtained from this configuration was much larger than the transfer of energy obtained using SDOF system in the first configuration because in this case the transfer of energy was dominated by the elastic mode of vibration.

The second phase of this study represented the application of MEID on floor impact vibration problem. The MEID adopted for this application consisted of a mass and spring system. The absorber mass was initially contacting with the floor. When impact load was applied to the floor, the kinetic energy and momentum of the floor were transferred to the absorber mass so that the floor had a small amount of shock. The vibration of the floor and sound generated in the room bellow the slab were simulated for various sized damper masses to show the effectiveness of the absorber. A

proof-of-concept experimental apparatus was fabricated to represent a floor with an impact damper. This example system consisted of an acrylic plate, a ball for falling object, and an impact damper. A comparison between the simulated and experimental results showed a good agreement in suggesting that the proposed impact damper was effective at reducing floor impact vibration and sound.

Application of MEID to a forging machine was presented in the third phase. In this application, MEID was used to reduce the bed vibration and transmitted force to the surrounding. The simulation result showed that the energy of forging machine increased when the contact frequency between impact source and press machine was close to the natural frequency of forging machine because of resonance phenomena. When this contact frequency was lower than the natural frequency of the forging machine, the reflected energy from the impact source became larger and as the consequence the kinetic energy of forging machine was decreased. Furthermore when this contact frequency was much larger than the natural frequency of the forging machine, the reflected energy was small but the transfer of energy increased with decreasing of forging machine energy.

Next, the MEID was applied to suppress the shock vibration of a boat. Two degrees of freedom model of boat with impact damper was proposed to evaluate the optimal parameter of impact damper for a boat application. A laboratory model of boat impacted by wave excitation was developed. The simulation and experimental result were in good agreement in suggesting that this model was good enough to simulate the experimental data.

6.2 Recommendation for Future Research

6.2.1 Full-scale Test

Laboratory model was quite effective for establishing the fundamental aspect of this study due to its simplicity. However the test condition may differ from the practical case. In order to bridge this gap, it is recommended to perform a series of test with a full scale of application system.

6.2.2 Modification of MEID

In order to obtain the larger transfer of energy, modification of MEID is recommended. This modification could be realized by using initial load (preload) and initial velocity of absorber mass.

APPENDIX

A.1 The Plate Element.

Consider an elastic element in Fig. A.1 subjected to a set of n forces

$$S = \left\{ S_1 \; S_2 \cdots S_i \;\; S_j \cdots S_n \right\}. \tag{A.1.1}$$

The displacements corresponding to the forces is denoted by the column matrix

$$\mathbf{u} = \left\{ u_1 \; u_2 \cdots u_i \; u_j \cdots u_n \right\}. \tag{A.1.2}$$

A typical force S_i is calculated using the unit displacement theorem. Hence

$$S_i = \int_{\upsilon} \underline{\boldsymbol{\varepsilon}}_i^T \boldsymbol{\sigma} dV \,. \tag{A.1.3}$$

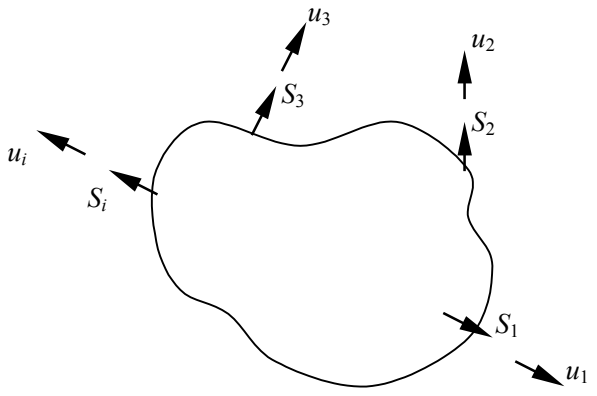

Fig. A.1 Elastic element.

where $\underline{\boldsymbol{\varepsilon}}_i$ represents the matrix of compatible strains due to a unit displacement in the direction of S_i and $\boldsymbol{\sigma}$ is the exact stress matrix due to the applied forces S. The unit displacement can be applied in turn at all points where the forces are impressed, and hence

$$\mathbf{S} = \int_{\upsilon} \underline{\boldsymbol{\varepsilon}}^T \boldsymbol{\sigma} dV \,, \tag{A.1.4}$$

where $\underline{\boldsymbol{\varepsilon}} = \left[\underline{\varepsilon}_1 \; \underline{\varepsilon}_1 \cdots \underline{\varepsilon}_i \; \underline{\varepsilon}_j \cdots \underline{\varepsilon}_n \right]$. (A.1.5)

For a linear system, the total strains ***e*** must be expressed by relationship

$$\mathbf{e} = \mathbf{b}\mathbf{u} \,. \tag{A.1.6}$$

where **b** represents a matrix of the exact strains due to unit displacement **u**

From Hookes law, the stress-strain relationship is given by

$$\begin{Bmatrix} \sigma_{xx} \\ \sigma_{yy} \\ \sigma_{zz} \\ \sigma_{xy} \\ \sigma_{yz} \\ \sigma_{zx} \end{Bmatrix} = \frac{E}{(1+\nu)(1-2\nu)} \begin{bmatrix} 1-\nu & \nu & \nu & 0 & 0 & 0 \\ \nu & 1-\nu & \nu & 0 & 0 & 0 \\ \nu & \nu & 1-\nu & 0 & 0 & 0 \\ 0 & 0 & 0 & \frac{1-2\nu}{2} & 0 & 0 \\ 0 & 0 & 0 & 0 & \frac{1-2\nu}{2} & 0 \\ 0 & 0 & 0 & 0 & 0 & \frac{1-2\nu}{2} \end{bmatrix} \begin{Bmatrix} e_{xx} \\ e_{yy} \\ e_{zz} \\ e_{xy} \\ e_{yz} \\ e_{zx} \end{Bmatrix}, \tag{A.1.7}$$

which in matrix notation can be presented as

$$\boldsymbol{\sigma} = \boldsymbol{\chi}\mathbf{e}, \tag{A.1.8}$$

substituting Eq. (A.1.6) into (A.1.8), yields

$$\boldsymbol{\sigma} = \boldsymbol{\chi}\mathbf{b}\mathbf{u}, \tag{A.1.9}$$

Hence, from Eqs. (A.1.4) and (A.1.9) the element force-displacement relationship becomes

$$\mathbf{S} = \int_{\upsilon} \underline{\boldsymbol{\varepsilon}}^{T} \boldsymbol{\chi}\mathbf{b} dV \mathbf{u}, \tag{A.1.10}$$

or

$$\mathbf{S} = \mathbf{k}\mathbf{u}, \tag{A.1.11}$$

where

$$\mathbf{k} = \int_{\upsilon} \underline{\boldsymbol{\varepsilon}}^{T} \boldsymbol{\chi}\mathbf{b} dV. \tag{A.1.12}$$

represent the element stiffness matrix

The matrix $\underline{\boldsymbol{\varepsilon}}$ representing compatible strain distribution can be evaluated without any appreciable difficulties, even for complex structural elements. On the other hand, evaluation of the matrix **b**, representing exact strain distributions, is often exceedingly difficult, if not impossible. In cases for which no exact strain distribution can be found approximate procedures must be used. This requires determination of approximate functional relationships between strain and displacements. Naturally, the degree of approximation then depends on the extent to which the equations of equilibrium and compatibility are satisfied. One possible approach is to select the matrix b in such a way that it will satisfy only the equations of compatibility. Denoting this approximate matrix by $\underline{\mathbf{b}}$, and noting that $\underline{\boldsymbol{\varepsilon}} = \underline{\mathbf{b}}$, the stiffness matrix can be written as

$$\mathbf{k} \simeq \int_{\upsilon} \underline{\mathbf{b}}^T \boldsymbol{\chi} \underline{\mathbf{b}} dV \,. \tag{A.1.13}$$

The model of four-node quadrilateral plate element is shown in Fig. A.2. The element properties are specified by four deflections and eight rotations. The degree of freedom (DOF) for each node consists of one translation and two rotations. Consequently, the total number of DOF for one element is 12. The interior displacements in the z direction (u_z) is expressible in terms of the discrete displacement $\mathbf{u} = \{u_1 \quad u_2 \quad u_3 \ldots\ldots u_{12}\}$

$$u_z = \mathbf{a}\mathbf{u}\,, \tag{A.1.14}$$

where $\mathbf{a} = \mathbf{a}(x,y,z)$ is a function of the position coordinates. The $\mathbf{a}$ matrix is calculated as follows[1]

$$\mathbf{a}^T = \begin{bmatrix} (1+2\xi)(1-\xi)^2(1+2\eta)(1-\eta)^2 \\ (1+2\xi)(1-\xi)^2\eta(1-\eta)^2 b \\ -\xi(1-\xi^2)(1+2\eta)(1-\eta)^2 a \\ (1+2\xi)(1-\xi)^2(3-2\eta)\eta^2 \\ -(1+2\xi)(1-\xi)^2(1-\eta)\eta^2 b \\ -\xi(1-\xi)^2(3-2\eta)\eta^2 a \\ (3-2\xi)\xi^2(3-2\eta)\eta^2 \\ -(3-2\xi)\xi^2(1-\eta)\eta^2 b \\ (1-\xi)\xi^2(3-2\eta)\eta^2 a \\ (3-2\xi)\xi^2(1+2\eta)+(1-\eta)^2 \\ (3-2\xi)\xi^2\eta(1-\eta)^2 b \\ (1-\xi)\xi^2(1+2\eta)(1-\eta)^2 a \end{bmatrix}, \tag{A.1.15}$$

where

$$\xi = \frac{x}{a} \quad ; \quad \eta = \frac{y}{b} \quad ; \quad \beta = \frac{b}{a}. \tag{A1.16}$$

The deflection function represented by Eqs. (A.1.14) and (A.1.15) ensures that the boundary deflections and slope on adjacent plate elements are compatible.

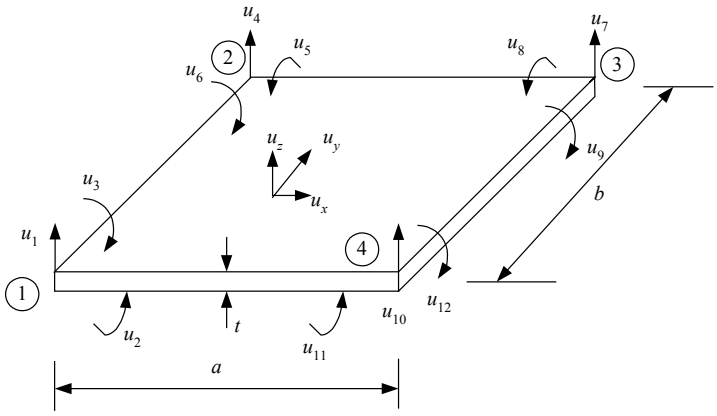

Fig. A.2 Plate element.

From the theory of elasticity, the strain are expressed as

$$e_{xx} = -z\frac{\partial^2 u_z}{\partial x^2} \quad ; \quad e_{yy} = -z\frac{\partial^2 u_z}{\partial y^2} \quad ; \quad e_{xy} = -2z\frac{\partial^2 u_z}{\partial x \partial y}. \tag{A.1.17}$$

which in matrix notation can be presented as

$$\mathbf{e} = \underline{\mathbf{b}}\mathbf{u}. \tag{A.1.18}$$

where

$$\underline{\mathbf{b}}^T = \begin{bmatrix}
(1-2\xi)(1+2\eta)(1-\eta)^2\frac{6z}{a^2} & (1+2\xi)(1-\xi)^2(1-2\eta)\frac{6z}{b^2} & -\xi(1-\xi)\eta(1-\eta)\frac{72z}{ab} \\
(1-2\xi)\eta(1-\eta)^2\frac{6bz}{a^2} & (1+2\xi)(1-\xi)^2(2-3\eta)\frac{2z}{b} & \xi(1-\xi)(1-\eta)(1-3\eta)\frac{12z}{a} \\
-(2-3\xi)(1+2\eta)(1-\eta)^2\frac{2z}{a} & -\xi(1-\xi)^2(1-2\eta)\frac{6az}{b^2} & -(1-\xi)(1-3\xi)\eta(1-\eta)\frac{12z}{b} \\
(1-2\xi)(3-2\eta)\eta^2\frac{6z}{a^2} & -(1+2\xi)(1-\xi)^2(1-2\eta)\frac{6z}{b^2} & \xi(1-\xi)\eta(1-\eta)\frac{72z}{ab} \\
-(1-2\xi)(1-\eta)\eta^2\frac{6bz}{a^2} & (1+2\xi)(1-\xi)^2(1-3\eta)\frac{2z}{b} & -\xi(1-\xi)\eta(2-3\eta)\frac{12z}{a} \\
-(2-3\xi)(3-2\eta)\eta^2\frac{2z}{a} & \xi(1-\xi)^2(1-2\eta)\frac{6az}{b^2} & (1-\xi)(1-3\xi)\eta(1-\eta)\frac{12z}{b} \\
-(1-2\xi)(3-2\eta)\eta^2\frac{6z}{a^2} & -(3-2\xi)\xi^2(1-2\eta)\frac{6z}{b^2} & -\xi(1-\xi)\eta(1-\eta)\frac{72z}{ab} \\
(1-2\xi)(1-\eta)\eta^2\frac{6bz}{a^2} & (3-2\xi)\xi^2(1-3\eta)\frac{2z}{b} & \xi(1-\xi)\eta(2-3\eta)\frac{12z}{a} \\
-(1-3\xi)(3-2\eta)\eta^2\frac{2z}{a} & -(1-\xi)\xi^2(1-2\eta)\frac{6az}{b^2} & -\xi(2-3\xi)\eta(1-\eta)\frac{12z}{b} \\
-(1-2\xi)(1+2\eta)(1-\eta)^2\frac{6z}{a^2} & (3-2\xi)\xi^2(1-2\eta)\frac{6z}{b^2} & \xi(1-\xi)\eta(1-\eta)\frac{72z}{ab} \\
-(1-2\xi)(1+2\eta)(1-\eta)^2\frac{6bz}{a^2} & (3-2\xi)\xi^2(2-3\eta)\frac{2z}{b} & -\xi(1-\xi)(1-\eta)(1-3\eta)\frac{12z}{a} \\
-(1-3\xi)(1+2\eta)(1-\eta)^2\frac{2z}{a} & (1-\xi)\xi^2(1-2\eta)\frac{6az}{b^2} & \xi(1-\xi)\eta(1-\eta)\frac{12z}{b}
\end{bmatrix} \tag{A.1.19}$$

For thin plate element, the stress distribution is the plane stress type. For this case the stress distribution assumed

$$\sigma_{zz} = \sigma_{zx} = \sigma_{zy} = 0\,. \tag{A.1.20}$$

Considering Eq. (A.1.20), the Hookes law in Eq. (A.1.7) can be written as

$$\begin{Bmatrix} \sigma_{xx} \\ \sigma_{yy} \\ \sigma_{xy} \end{Bmatrix} = \frac{E}{1-\nu^2} \begin{bmatrix} 1 & \nu & 0 \\ \nu & 1 & 0 \\ 0 & 0 & \dfrac{1-\nu}{2} \end{bmatrix} \begin{Bmatrix} e_{xx} \\ e_{yy} \\ e_{xy} \end{Bmatrix}, \tag{A.1.21}$$

which in matrix notation can be presented as

$$\boldsymbol{\sigma} = \boldsymbol{\chi}\mathbf{e}\,. \tag{A.1.22}$$

Acording to Eq. (A.1.13), element stiffness matrix ($\mathbf{k}_e$) is calculated as follows

$$\mathbf{k}_e \simeq \int_{\upsilon} \underline{\mathbf{b}}^T \boldsymbol{\chi} \underline{\mathbf{b}} dV\,. \tag{A.1.23}$$

Substitution of Eq. (A.1.19) into Eq. (A.1.23) and yields

$$\mathbf{k}_e = \begin{array}{c} 1 \\ \vdots \\ 6 \\ 7 \\ \vdots \\ 12 \end{array} \begin{bmatrix} \mathbf{K}_{\mathbf{I,I}} & & \textit{Symmetric} \\ & & \\ & & \\ \mathbf{K}_{\mathbf{II,I}} & & \mathbf{K}_{\mathbf{II,II}} \end{bmatrix}. \tag{A.1.24}$$

$$\begin{array}{cccccc} 1 & \cdots & 6 & 7 & & 12 \end{array}$$

where the submatrices $\mathbf{k_{I,I}}$, $\mathbf{k_{II,I}}$, and $\mathbf{k_{II,II}}$ presented separately Eq. (A.1.25)-(A.1.27)

$$\mathbf{k}_{\mathbf{I,I}} = \frac{Et^3}{12(1-\nu^2)ab} \begin{bmatrix} \frac{156}{35}(\beta^2+\beta^{-2})+\frac{72}{25} & & & & & \\ \left[\frac{22}{35}\beta^2+\frac{28}{35}\beta^{-2}+\frac{6}{25}(1+5\nu)\right]b & \left(-\frac{4}{35}\beta^2+\frac{52}{35}\beta^{-2}+\frac{8}{25}\right)b^2 & & \textit{Symmetric} & & \\ -\left[\frac{78}{35}\beta^2+\frac{22}{35}\beta^{-2}+\frac{6}{25}(1+5\nu)\right]a & -\left[\frac{11}{35}(\beta^2+\beta^{-2})+\frac{1}{50}(1+60\nu)\right]ab & \left(\frac{52}{35}\beta^2+\frac{4}{35}\beta^{-2}+\frac{8}{25}\right)a^2 & & & \\ \frac{54}{35}\beta^2-\frac{156}{35}\beta^{-2}-\frac{72}{25} & \left(\frac{13}{35}\beta^2-\frac{78}{35}\beta^{-2}-\frac{6}{25}\right)b & \left[-\frac{27}{35}\beta^2+\frac{22}{35}\beta^{-2}+\frac{6}{25}(1+5\nu)\right]a & \frac{156}{35}(\beta^2+\beta^{-2})+\frac{22}{25} & & \\ \left(-\frac{13}{35}\beta^2+\frac{78}{35}\beta^{-2}+\frac{6}{25}\right)b & \left(\frac{3}{35}\beta^2+\frac{26}{35}\beta^{-2}-\frac{2}{25}\right)b^2 & \left[\frac{13}{70}\beta^2-\frac{11}{35}\beta^{-2}-\frac{1}{50}(1+5\nu)\right]ab & \left[-\frac{22}{35}\beta^2+\frac{78}{35}\beta^{-2}+\frac{6}{25}(1+5\nu)\right]b & \left(\frac{4}{35}\beta^2+\frac{52}{35}\beta^{-2}+\frac{8}{25}\right)b^2 & \\ \left[-\frac{27}{35}\beta^2+\frac{22}{35}\beta^{-2}+\frac{6}{25}(1+5\nu)\right]a & \left[-\frac{13}{70}\beta^2+\frac{11}{35}\beta^{-2}+\frac{1}{50}(1+5\nu)\right]ab & \left(\frac{18}{35}\beta^2-\frac{4}{35}\beta^{-2}-\frac{8}{25}\right)a^2 & -\left[\frac{78}{35}\beta^2+\frac{22}{35}\beta^{-2}+\frac{6}{25}(1+5\nu)\right]a & \left[\frac{11}{35}(\beta^2+\beta^{-2})+\frac{1}{50}(1+60\nu)\right]ab & \left(\frac{52}{35}\beta^2+\frac{4}{35}\beta^{-2}+\frac{8}{25}\right)a^2 \end{bmatrix} \tag{A.1.25}$$

$$\mathbf{k}_{\mathbf{II,I}} = \frac{Et^3}{12(1-\nu^2)ab} \begin{bmatrix} -\frac{54}{35}(\beta^2+\beta^{-2})+\frac{72}{25} & \left(-\frac{13}{35}\beta^2-\frac{27}{35}\beta^{-2}+\frac{6}{25}\right)b & \left(\frac{27}{35}\beta^2+\frac{13}{35}\beta^{-2}-\frac{6}{25}\right)a & -\frac{156}{35}\beta^2+\frac{54}{35}\beta^{-2}-\frac{72}{25} & \left[\frac{22}{35}\beta^2-\frac{27}{35}\beta^{-2}+\frac{6}{25}(1+5\nu)\right]b & \left(\frac{78}{35}\beta^2-\frac{13}{35}\beta^{-2}+\frac{6}{25}\right)a \\ \left(\frac{13}{35}\beta^2+\frac{27}{35}\beta^{-2}-\frac{6}{25}\right)b & \left(\frac{3}{35}\beta^2+\frac{9}{35}\beta^{-2}+\frac{2}{25}\right)b^2 & \left[\frac{13}{70}(\beta^2+\beta^{-2})-\frac{1}{50}\right]ab & \left[\frac{22}{35}\beta^2-\frac{27}{35}\beta^{-2}+\frac{6}{25}(1+5\nu)\right]b & \left(-\frac{4}{35}\beta^2+\frac{18}{35}\beta^{-2}-\frac{8}{25}\right)b^2 & \left[-\frac{11}{35}\beta^2+\frac{13}{70}\beta^{-2}-\frac{1}{50}(1+5\nu)\right]ab \\ \left(-\frac{27}{35}\beta^2-\frac{13}{35}\beta^{-2}+\frac{6}{25}\right)a & \left[-\frac{13}{70}(\beta^2+\beta^{-2})+\frac{1}{50}\right]ab & \left(\frac{9}{35}\beta^2+\frac{3}{35}\beta^{-2}+\frac{2}{25}\right)a^2 & \left(-\frac{78}{35}\beta^2+\frac{13}{35}\beta^{-2}-\frac{6}{25}\right)a & \left[\frac{11}{35}\beta^2-\frac{13}{70}\beta^{-2}+\frac{1}{50}(1+5\nu)\right]ab & \left(\frac{26}{35}\beta^2-\frac{3}{35}\beta^{-2}-\frac{2}{25}\right)a^2 \\ -\frac{156}{35}\beta^2+\frac{54}{35}\beta^{-2}-\frac{72}{25} & \left[-\frac{22}{35}\beta^2+\frac{27}{35}\beta^{-2}-\frac{6}{25}(1+5\nu)\right]b & \left(\frac{78}{35}\beta^2-\frac{13}{35}\beta^{-2}+\frac{6}{25}\right)a & -\frac{54}{35}(\beta^2+\beta^{-2})+\frac{72}{25} & \left(\frac{13}{35}\beta^2+\frac{27}{35}\beta^{-2}-\frac{6}{25}\right)b & \left(\frac{27}{35}\beta^2+\frac{13}{35}\beta^{-2}-\frac{6}{25}\right)a \\ \left[-\frac{22}{35}\beta^2+\frac{27}{35}\beta^{-2}-\frac{6}{25}(1+5\nu)\right]b & \left(\frac{4}{35}\beta^2+\frac{18}{35}\beta^{-2}-\frac{8}{25}\right)b^2 & \left[\frac{11}{35}\beta^2-\frac{13}{70}\beta^{-2}+\frac{1}{50}(1+5\nu)\right]ab & \left(-\frac{13}{35}\beta^2-\frac{27}{35}\beta^{-2}+\frac{6}{25}\right)b & \left(\frac{3}{35}\beta^2+\frac{9}{35}\beta^{-2}+\frac{2}{25}\right)b^2 & \left[\frac{13}{70}(\beta^2+\beta^{-2})-\frac{1}{50}\right]ab \\ \left(-\frac{78}{35}\beta^2+\frac{13}{35}\beta^{-2}-\frac{6}{25}\right)a & \left[-\frac{11}{35}\beta^2+\frac{13}{70}\beta^{-2}-\frac{1}{50}(1+5\nu)\right]ab & \left(\frac{26}{35}\beta^2-\frac{3}{35}\beta^{-2}-\frac{2}{25}\right)a^2 & \left(-\frac{27}{35}\beta^2-\frac{27}{35}\beta^{-2}+\frac{6}{25}\right)a & \left[\frac{13}{70}(\beta^2+\beta^{-2})-\frac{1}{50}\right]ab & \left(\frac{9}{35}\beta^{-2}+\frac{3}{35}\beta^{-2}+\frac{2}{25}\right)a^2 \end{bmatrix} \tag{A.1.26}$$

$$\mathbf{k}_{1,1}=\frac{Et^3}{12(1-\nu^2)ab}\begin{bmatrix}
\frac{156}{35}(\beta^2+\beta^{-2})+\frac{72}{25} & & & & & & & & & & & \\
-\left[\frac{22}{35}\beta^2+\frac{78}{35}\beta^{-2}+\frac{6}{25}(1+5\nu)\right]b & \left(\frac{4}{35}\beta^2+\frac{52}{35}\beta^{-2}+\frac{8}{25}\right)b^2 & & & & & & & & & & \\
\left[\frac{78}{35}\beta^2+\frac{22}{35}\beta^{-2}+\frac{6}{25}(1+5\nu)\right]a & -\left[\frac{11}{35}(\beta^2+\beta^{-2})+\frac{1}{50}(1+60\nu)\right]ab & \left(\frac{52}{35}\beta^2+\frac{4}{35}\beta^{-2}+\frac{8}{25}\right)a^2 & & & & & & & & & \\
\frac{54}{35}\beta^2-\frac{156}{35}\beta^{-2}-\frac{72}{25} & \left(-\frac{13}{35}\beta^2+\frac{78}{35}\beta^{-2}+\frac{6}{25}\right)b & \left[\frac{27}{35}\beta^2-\frac{22}{35}\beta^{-2}-\frac{6}{25}(1+5\nu)\right]a & \frac{156}{35}(\beta^2+\beta^{-2})+\frac{72}{25} & & & & & & & & \\
\left(\frac{13}{35}\beta^2-\frac{78}{35}\beta^{-2}-\frac{6}{25}\right)b & \left(\frac{-3}{35}\beta^2+\frac{26}{35}\beta^{-2}-\frac{2}{25}\right)b^2 & \left[\frac{13}{70}\beta^2-\frac{11}{35}\beta^{-2}-\frac{1}{50}(1+5\nu)\right]ab & \left[\frac{22}{35}\beta^2+\frac{78}{35}\beta^{-2}+\frac{6}{25}(1+5\nu)\right]b & \left(\frac{4}{35}\beta^2+\frac{52}{35}\beta^{-2}+\frac{8}{25}\right)b^2 & & & & & & \\
\left[\frac{27}{35}\beta^2-\frac{22}{35}\beta^{-2}-\frac{6}{25}(1+5\nu)\right]a & \left[-\frac{13}{70}\beta^2+\frac{11}{35}\beta^{-2}+\frac{1}{50}(1+5\nu)\right]ab & \left(\frac{18}{35}\beta^2-\frac{4}{35}\beta^{-2}-\frac{8}{25}\right)a^2 & \left[\frac{78}{35}\beta^2+\frac{22}{35}\beta^{-2}+\frac{6}{25}(1+5\nu)\right]a & \left[\frac{11}{35}(\beta^2+\beta^{-2})+\frac{1}{50}(1+60\nu)\right]ab & \left(\frac{52}{35}\beta^{-2}+\frac{4}{35}\beta^{-2}+\frac{8}{25}\right)a^2 & & & & & \\
\end{bmatrix}$$

Symmetric

(A.1.27)

The element mass matrix ($\mathbf{m}_e$) is calculated as follows (Pziemeniecky, 1967)

$$\mathbf{m}_e=\int_v \rho\mathbf{a}^T\mathbf{a}dV\ . \tag{A.1.28}$$

by subtituting the **a** matriks in Eq. (A.1.15) into Eq. (A.1.28) and performing integration over the whole volume of the rectangle, the mass matrix is obtained as

$$\mathbf{m}_e=\frac{\rho ab}{176400}\begin{bmatrix}
24336 & & & & & & & & & & & \\
3432b & 624b^2 & & & & & & & & & & \\
-3432a & -484ab & 624b^2 & & & & & & & & & \\
8424 & 2028b & -1188a & 24336 & & & & & & & & \\
-2028b & -468b^2 & 286ab & -3432b & 624b^2 & & & & & & & \\
-1188a & -286ab & 216a^2 & -3432a & 484ab & 624a^2 & & & & & & \\
2916 & 702b & -702a & 8424 & -1188b & -2028a & 24336 & & & & & \\
-702b & -162b^2 & 169ab & -1188b & 216b^2 & 286ab & -3432b & 624b^2 & & & & \\
702a & 169ab & -162a^2 & 2028a & -286ab & -468a^2 & 3432a & -484ab & 624a^2 & & & \\
8424 & 1188b & -2028a & 2916 & -702b & -702a & 8424 & -2028b & 1188a & 24336 & & \\
1188b & 216b^2 & -286ab & 702b & -162b^2 & -169ab & 2028b & -468b^2 & 286ab & 3432b & 624b^2 & \\
2028a & 286ab & -468a^2 & 702a & -169ab & -162a^2 & 1188a & -286ab & 216a^2 & 3432a & 484ab & 624a^2
\end{bmatrix}$$

(A.1.29)

A.2 The Three Dimensional Frame Element

A.2.1 Stiffness Matrix and Mass Matrix in Local Coordinate

The model of three dimensional frame element is shown in Fig. A.3. The element properties are specified by six deflections and six rotations. The degree of freedom (DOF) for each node consists of three translation and three rotations. Consequently, the total number of DOF for one element is 12.

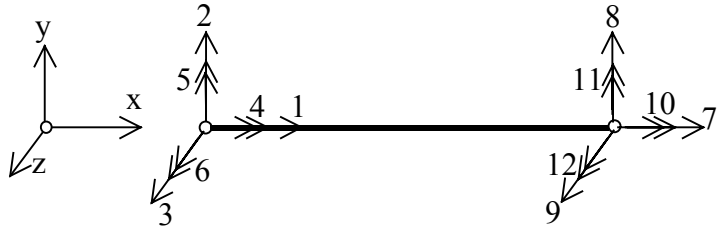

Fig. A.3 Three dimensional frame element.

A.2.1.1 The Axial Displacement Shape Function

The axial displacement of frame element can be approximated using a linear function as.

$$u(x) = \alpha_1 + \alpha_2 x . \tag{A.2.1}$$

By inserting the of boundary condition into Eq. (A.2.1) yields
for $x = 0$

$$u(0) = \alpha_1 + \alpha_2 0 , \tag{A.2.2}$$

$$\alpha_1 = u_1 . \tag{A.2.3}$$

for $x = \ell$

$$u(\ell) = \alpha_1 + \alpha_2 \ell = u_7 , \tag{A.2.4}$$

$$\alpha_2 = -\frac{u_1}{\ell} + \frac{u_7}{\ell} . \tag{A.2.5}$$

Subtitution of α_1 and α_2 in Eqs. (A.2.3) and (A.2.5) into Eq. (A.2.1) resulting

$$u(x) = u_1 - \frac{u_1}{\ell} x + \frac{u_7}{\ell} x , \tag{A.2.6}$$

$$u(x) = \begin{pmatrix} \psi_1(x) & \psi_7(x) \end{pmatrix} \begin{Bmatrix} u_1 \\ u_7 \end{Bmatrix} . \tag{A.2.7}$$

Using the result in Eq. (A.2.7), the shape function for axial displacement can be written as

$$\psi_1(x) = 1 - \frac{x}{\ell} , \tag{A.2.8}$$

$$\psi_7(x) = \frac{x}{\ell} . \tag{A.2.9}$$

A.2.1.2 The Rotational Displacement Shape Function

The rotational displacement for frame element can be expressed using the same linear function as in the axial displacement so that the shape functions are also the same

$$\psi_4(x) = 1 - \frac{x}{\ell} , \tag{A.2.10}$$

$$\psi_{10}(x) = \frac{x}{\ell} . \tag{A.2.11}$$

A.2.1.3 The Displacement Shape Function for Flexural in x-y Plane

The displacement in *x-y* plane is shown in Fig. A.4. The displacement can be approximated using a cubic function as.

$$u(x) = \alpha_1 + \alpha_2 x + \alpha_3 x^2 + \alpha_4 x^3 . \tag{A.2.12}$$

$$\theta(x) = u'(x) = \alpha_2 + 2\alpha_3 x + 3\alpha_4 x^2 . \tag{A.2.13}$$

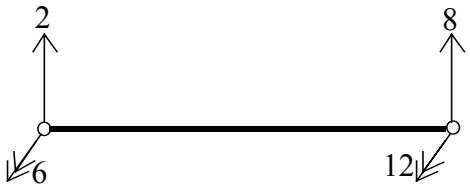

Fig. A.4 Displacement in *x-y* plane.

By inserting the of boundary condition into Eq. (A.2.12) and Eq. (A.2.13) yields

$$u_2 = \alpha_1 , \tag{A.2.14}$$

$$u_8 - u_2 = \alpha_2 \cdot \ell + \alpha_3 \cdot \ell^2 + \alpha_4 \cdot \ell^3 , \tag{A.2.15}$$

$$\theta_6 = \alpha_2 , \tag{A.2.16}$$

$$\theta_{12} - \theta_6 = 2\alpha_3 \cdot \ell + 3\alpha_4 \cdot \ell^2 . \tag{A.2.17}$$

Solution of Eqs. (A.2.14)- .(A.2.17) for α_3 and α_4 resulting

$$\alpha_3 = -\frac{3u_2}{\ell^2} - \frac{2\theta_6}{\ell} + \frac{3u_8}{\ell^2} - \frac{\theta_{12}}{\ell} , \tag{A.2.18}$$

$$\alpha_4 = \frac{2u_2}{\ell^3} + \frac{\theta_6}{\ell^2} - \frac{2u_8}{\ell^3} + \frac{\theta_{12}}{\ell^2} . \tag{A.2.19}$$

Subtitution of α_1, α_2, ,α_3 and α_4 into Eq. (A.2.12) given

$$u(x) = u_1 + \theta_2 x + \left(-\frac{3u_2}{\ell^2} - \frac{2\theta_6}{\ell} + \frac{3u_8}{\ell^2} - \frac{\theta_{12}}{\ell} \right) x^2 + \left(\frac{2u_2}{\ell^3} + \frac{\theta_6}{\ell^2} - \frac{2u_8}{\ell^3} + \frac{\theta_{12}}{\ell^2} \right) x^3 , \tag{A.2.20}$$

$$u(x) = \begin{pmatrix} \psi_2(x) & \psi_6(x) & \psi_8(x) & \psi_{12}(x) \end{pmatrix} \begin{Bmatrix} u_2 \\ \theta_6 \\ u_8 \\ \theta_{12} \end{Bmatrix} . \tag{A.2.21}$$

From Eq. (A.2.21) the shape function are obtained as

$$\psi_2(x) = 1 - \frac{3}{\ell^2}x^2 + \frac{2}{\ell^3}x^3, \quad \text{(A.2.22)}$$

$$\psi_6(x) = x - \frac{2}{\ell^2}x^2 + \frac{1`}{\ell^2}x^3, \quad \text{(A.2.23)}$$

$$\psi_8(x) = \frac{3}{\ell^2}x^2 - \frac{2}{\ell^3}x^3, \quad \text{(A.2.24)}$$

$$\psi_{12}(x) = -\frac{1}{\ell}x^2 + \frac{1}{\ell^2}x^3. \quad \text{(A.2.25)}$$

A.2.1.4 The Displacement Function for Flexural in x-z Plane

The displacement of frame element in *x-z* plane is shown in Fig. A.5. The displacement can be approximated using a cubic function as.

$$u(x) = \alpha_1 + \alpha_2 x + \alpha_3 x^2 + \alpha_4 x^3, \quad \text{(A.2.26)}$$

$$\theta(x) = u'(x) = \alpha_2 + 2\alpha_3 x + 3\alpha_4 x^2. \quad \text{(A.2.27)}$$

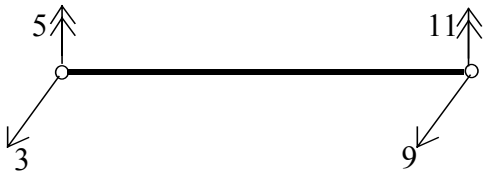

Fig. A.5 Displacement in *x-z* plane.

By using the same procedures as for *x-y* plane, the shape function for x-z plane is given by

: $$\psi_3(x) = 1 - \frac{3}{\ell^2}x^2 + \frac{2}{\ell^3}x^3, \quad \text{(A.2.28)}$$

$$\psi_5(x) = -x + \frac{2}{\ell^2}x^2 - \frac{1`}{\ell^2}x^3, \quad \text{(A.2.29)}$$

$$\psi_9(x) = \frac{3}{\ell^2}x^2 - \frac{2}{\ell^3}x^3, \quad \text{(A.2.30)}$$

$$\psi_{11}(x) = \frac{1}{\ell}x^2 - \frac{1}{\ell^2}x^3. \quad \text{(A.2.31)}$$

Table A.1 The shape function and its differentiation for 3D frame element.

No.	$\psi(x)$	$\psi'(x)$	$\psi''(x)$
1	$\psi_1(x) = 1-\frac{x}{\ell}$	$-\frac{1}{\ell}$	0
2	$\psi_2(x) = 1-\frac{3}{\ell^2}x^2+\frac{2}{\ell^3}x^3$	$-\frac{6x}{\ell^2}+\frac{6x^2}{\ell^3}$	$-\frac{6}{\ell^2}+\frac{12x}{\ell^3}$
3	$\psi_3(x) = 1-\frac{3}{\ell^2}x^2+\frac{2}{\ell^3}x^3$	$-\frac{6x}{\ell^2}+\frac{6x^2}{\ell^3}$	$-\frac{6}{\ell^2}+\frac{12x}{\ell^3}$
4	$\psi_4(x) = 1-\frac{x}{\ell}$	$-\frac{1}{\ell}$	0
5	$\psi_5(x) = -x+\frac{2}{\ell^2}x^2-\frac{1`}{\ell^2}x^3$	$-1+\frac{4x}{\ell}-\frac{3x^2}{\ell^2}$	$\frac{4}{\ell}-\frac{6x}{\ell^2}$
6	$\psi_6(x) = x-\frac{2}{\ell^2}x^2+\frac{1`}{\ell^2}x^3$	$1-\frac{4x}{\ell}+\frac{3x^2}{\ell^2}$	$-\frac{4}{\ell}-\frac{6x}{\ell^2}$
7	$\psi_7(x) = \frac{x}{\ell}$	$\frac{1}{\ell}$	0
8	$\psi_8(x) = \frac{3}{\ell^2}x^2-\frac{2}{\ell^3}x^3$	$\frac{6x}{\ell^2}-\frac{6x^2}{\ell^3}$	$\frac{6}{\ell^2}-\frac{12x}{\ell^3}$
9	$\psi_9(x) = \frac{3}{\ell^2}x^2-\frac{2}{\ell^3}x^3$	$\frac{6x}{\ell^2}-\frac{6x^2}{\ell^3}$	$\frac{6}{\ell^2}-\frac{12x}{\ell^3}$
10	$\psi_{10}(x) = \frac{x}{\ell}$	$\frac{1}{\ell}$	0
11	$\psi_{11}(x) = \frac{1}{\ell}x^2-\frac{1}{\ell^2}x^3$	$\frac{2x}{\ell}-\frac{3x^3}{\ell^2}$	$\frac{2}{\ell}-\frac{6x^2}{\ell^2}$
12	$\psi_{12}(x) = -\frac{1}{\ell}x^2+\frac{1}{\ell^2}x^3$	$-\frac{2x}{\ell}+\frac{3x^3}{\ell^2}$	$-\frac{2}{\ell}+\frac{6x^2}{\ell^2}$

The stiffness coefficient for frame element in the normal displacement is given by

$$K_{ij} = \int_0^{\ell} AE\psi_i'\psi_j'(x)\,dx \qquad \text{i = 1, 7} \quad \text{and } j = 1, 7. \tag{A.2.32}$$

The stiffness coefficient for frame element in the rotational displacement is given by

$$K_{ij} = \int_0^{\ell} GJ\psi_i'\psi_j'(x)\,dx \qquad \text{i = 4, 10} \quad \text{and} \quad j = 4, 10. \tag{A.2.33}$$

The coefficients relating to the flexural displacement in *x*-*y* plane and *x*-*z* plane are given by

$$K_{ij} = \int_0^{\ell} EI_z\psi_i'''\psi_j''(x)\,dx \quad \text{i = 2, 6, 8, 12} \quad \text{and} \quad \text{j = 2, 6, 8, 12,} \tag{A.2.34}$$

$$K_{ij} = \int_0^{\ell} EI_y\psi_i''\psi_j''(x)\,dx \qquad \text{i = 3, 5, 9, 11 and} \quad \text{j = 3, 5, 9, 11.} \tag{A.2.35}$$

The stiffness component in the axial direction are given by

$$K_{11} = \int_0^{\ell} AE\psi_1'\psi_1'(x)\,dx,$$

$$= AE\int_o^{\ell}\left(-\frac{1}{\ell}\right)\left(-\frac{1}{\ell}\right)dx,$$

$$= \frac{AE}{\ell}. \tag{A.2.36}$$

$$K_{17} = \int_0^{\ell} AE\psi_1'(x)\psi_7'(x)\,dx,$$

$$= AE\int_o^{\ell}\left(-\frac{1}{\ell}\right)\left(\frac{1}{\ell}\right)dx,$$

$$= -\frac{AE}{\ell}. \tag{A.2.37}$$

$$K_{77} = \int_0^{\ell} AE\psi_7'(x)\psi_7'(x)\,dx,$$

$$= AE\int_o^{\ell}\left(\frac{1}{\ell}\right)\left(\frac{1}{\ell}\right)dx,$$

$$= \frac{AE}{\ell}. \tag{A.2.38}$$

The stiffness component in the rotational direction are given by

$$K_{44} = \int_0^{\ell} GJ\psi_4'(x)\psi_4'(x)\,dx,$$

$$= GJ\int_o^{\ell}\left(-\frac{1}{\ell}\right)\left(-\frac{1}{\ell}\right)dx,$$

$$= \frac{GJ}{\ell}. \qquad \text{(A.2.39)}$$

$$K_{4,10} = \int_0^{\ell} GJ\psi_4'(x)\psi_{10}'(x)\,dx,$$

$$= GJ\int_o^{\ell}\left(-\frac{1}{\ell}\right)\left(\frac{1}{\ell}\right)dx,$$

$$= -\frac{GJ}{\ell}. \qquad \text{(A.2.40)}$$

$$K_{10,10} = \int_0^{\ell} GJ\psi_{10}'(x)\psi_{10}'(x)\,dx,$$

$$= GJ\int_o^{\ell}\left(\frac{1}{\ell}\right)\left(\frac{1}{\ell}\right)dx,$$

$$= \frac{GJ}{\ell}. \qquad \text{(A.2.41)}$$

For the stiffness component in the x-y plane, the values are given by

$$K_{2,2} = \int_0^{\ell} EI_z\psi_2''(x)\psi_2''(x)\,dx,$$

$$= EI_z\int_o^{\ell}\left(-\frac{6}{\ell^2}+\frac{12x}{\ell^3}\right)^2 dx,$$

$$= \frac{12EI_z}{\ell^3}. \qquad \text{(A.2.42)}$$

$$K_{2,6} = \int_0^{\ell} EI_z \psi_2''(x)\psi_6''(x)\,dx,$$

$$= EI_z \int_o^{\ell} \left(-\frac{6}{\ell^2} + \frac{12x}{\ell^3}\right)\left(-\frac{4}{\ell} + \frac{6x}{\ell^2}\right)dx,$$

$$= \frac{6EI_z}{\ell^2}. \qquad \text{(A.2.43)}$$

$$K_{2,8} = \int_0^{\ell} EI_z \psi_2''(x)\psi_8''(x)\,dx,$$

$$= EI_z \int_o^{\ell} \left(-\frac{6}{\ell^2} + \frac{12x}{\ell^3}\right)\left(\frac{6}{\ell^2} - \frac{12x}{\ell^3}\right)dx,$$

$$= -\frac{12EI_z}{\ell^3}. \qquad \text{(A.2.44)}$$

$$K_{2,12} = \int_0^{\ell} EI_z \psi_2''(x)\psi_{12}''(x)\,dx,$$

$$= EI_z \int_o^{\ell} \left(-\frac{6}{\ell^2} + \frac{12x}{\ell^3}\right)\left(-\frac{2}{\ell} - \frac{6x}{\ell^2}\right)dx,$$

$$= \frac{6EI_z}{\ell^2}. \qquad \text{(A.2.45)}$$

$$K_{8,8} = \int_0^{\ell} EI_z \psi_8''(x)\psi_8''(x)\,dx,$$

$$= EI_z \int_o^{\ell} \left(\frac{6}{\ell^2} - \frac{12x}{\ell^3}\right)^2 dx,$$

$$= \frac{12EI_z}{\ell^3}. \qquad \text{(A.2.46)}$$

$$K_{6,6} = \int_0^{\ell} EI_z \psi_6''(x)\psi_6''(x)\,dx,$$

$$= EI_z \int_o^{\ell} \left(-\frac{4}{\ell} - \frac{6x}{\ell^2} \right)^2 dx ,$$

$$= \frac{4EI_z}{\ell} . \qquad \text{(A.2.47)}$$

$$K_{6,8} = \int_0^{\ell} EI_z \psi_6''(x) \psi_8''(x) dx ,$$

$$= EI_z \int_o^{\ell} \left(-\frac{4}{\ell} + \frac{6x}{\ell^2} \right) \left(\frac{6}{\ell^2} - \frac{12x}{\ell^3} \right) dx ,$$

$$= -\frac{6EI_z}{\ell^3} . \qquad \text{(A.2.48)}$$

$$K_{6,12} = \int_0^{\ell} EI_z \psi_6'''(x) \psi_{12}'''(x) dx ,$$

$$= EI_z \int_o^{\ell} \left(-\frac{4}{\ell} + \frac{6x}{\ell^2} \right) \left(-\frac{2}{\ell} + \frac{6x}{\ell^2} \right) dx ,$$

$$= \frac{2EI_z}{\ell^3} . \qquad \text{(A.2.49)}$$

$$K_{8,12} = \int_0^{\ell} EI_z \psi_8'''(x) \psi_{12}'''(x) dx ,$$

$$= EI_z \int_o^{\ell} \left(\frac{6}{\ell^2} - \frac{12x}{\ell^3} \right) \left(-\frac{2}{\ell} + \frac{6x}{\ell^2} \right) dx ,$$

$$= -\frac{6EI_z}{\ell^2} . \qquad \text{(A.2.50)}$$

$$K_{12,12} = \int_0^{\ell} EI_z \psi_{12}''(x) \psi_{12}''(x) dx ,$$

$$= EI_z \int_o^{\ell} \left(-\frac{2}{\ell} + \frac{6x}{\ell^2} \right)^2 dx ,$$

$$= \frac{4EI_z}{\ell^2}. \tag{A.2.51}$$

For the stiffness component in the x-z plane, the values are given by

$$K_{3,3} = \int_0^\ell EI_y \psi_3''(x)\psi_3''(x)\,dx,$$

$$= EI_y \int_o^\ell \left(-\frac{6}{\ell^2} + \frac{12x}{\ell^3}\right)^2 dx,$$

$$= \frac{12EI_y}{\ell^3}. \tag{A.2.52}$$

$$K_{3,5} = \int_0^\ell EI_y \psi_3''(x)\psi_5''(x)\,dx,$$

$$= EI_y \int_o^\ell \left(-\frac{6}{\ell^2} + \frac{12x}{\ell^3}\right)\left(\frac{4}{\ell} - \frac{6x}{\ell^2}\right)dx,$$

$$= -\frac{6EI_y}{\ell^2}. \tag{A.2.53}$$

$$K_{3,9} = \int_0^\ell EI_y \psi_3''(x)\psi_9''(x)\,dx,$$

$$= EI_y \int_o^\ell \left(-\frac{6}{\ell^2} + \frac{12x}{\ell^3}\right)\left(\frac{6}{\ell^2} - \frac{12x}{\ell^3}\right)dx,$$

$$= -\frac{12EI_y}{\ell^2}. \tag{A.2.54}$$

$$K_{3,11} = \int_0^\ell EI_y \psi_3''(x)\psi_{11}''(x)\,dx,$$

$$= EI_y \int_o^\ell \left(-\frac{6}{\ell^2} + \frac{12x}{\ell^3}\right)\left(\frac{2}{\ell} - \frac{6x}{\ell^3}\right)dx,$$

$$= -\frac{6EI_y}{\ell^2}. \tag{A.2.55}$$

$$K_{5,5} = \int_0^{\ell} EI_y \psi_5''(x)\psi_5''(x)\,dx,$$

$$= EI_y \int_o^{\ell} \left(\frac{4}{\ell} - \frac{6x}{\ell^2}\right)^2 dx,$$

$$= \frac{4EI_y}{\ell}. \qquad \text{(A.2.56)}$$

$$K_{9,9} = \int_0^{\ell} EI_y \psi_9''(x)\psi_9''(x)\,dx,$$

$$= EI_y \int_o^{\ell} \left(\frac{6}{\ell^2} + \frac{12x}{\ell^3}\right)^2 dx,$$

$$= \frac{12EI_y}{\ell^3}. \qquad \text{(A.2.57)}$$

$$K_{9,11} = \int_0^{\ell} EI_y \psi_9''(x)\psi_{11}''(x)\,dx,$$

$$= EI_y \int_o^{\ell} \left(\frac{6}{\ell^2} + \frac{12x}{\ell^3}\right)\left(\frac{2}{\ell} - \frac{6x}{\ell^2}\right) dx,$$

$$= \frac{6EI_y}{\ell^2}. \qquad \text{(A.2.58)}$$

$$K_{11,11} = \int_0^{\ell} EI_y \psi_{11}''(x)\psi_{11}''(x)\,dx,$$

$$= EI_y \int_o^{\ell} \left(\frac{2}{\ell} - \frac{6x}{\ell^2}\right)^2 dx,$$

$$= \frac{4EI_y}{\ell}. \qquad \text{(A.2.59)}$$

The stiffness matrix of frame element in local coordinate is given by (Bur, 1994)

$$\bar{\mathbf{k}}_e = \begin{bmatrix}
\frac{AE}{\ell} & & & & & & & & & & & \\
0 & \frac{12EI_z}{\ell^3} & & & & & & & & & & \\
0 & 0 & \frac{12EI_y}{\ell^3} & & & & & & & & & \\
0 & 0 & 0 & \frac{GJ}{\ell} & & & & & & & & \\
0 & 0 & -\frac{6EI_y}{\ell^2} & 0 & \frac{4EI_y}{\ell} & & & & & & & \\
0 & \frac{6EI_z}{\ell^2} & 0 & 0 & 0 & \frac{4EI_z}{\ell} & & & & & & \\
-\frac{AE}{\ell} & 0 & 0 & 0 & 0 & 0 & \frac{AE}{\ell} & & & & & \\
0 & -\frac{12EI_z}{\ell^3} & 0 & 0 & 0 & -\frac{6EI_z}{\ell^2} & 0 & \frac{12EI_z}{\ell^3} & & & & \\
0 & 0 & -\frac{12EI_y}{\ell^3} & 0 & \frac{6EI_y}{\ell^2} & 0 & 0 & 0 & \frac{12EI_y}{\ell^3} & & & \\
0 & 0 & 0 & -\frac{GJ}{\ell} & 0 & 0 & 0 & 0 & 0 & \frac{GJ}{\ell} & & \\
0 & 0 & -\frac{6EI_y}{\ell^2} & 0 & \frac{2EI_y}{\ell} & 0 & 0 & 0 & \frac{6EI_y}{\ell^2} & 0 & \frac{4EI_y}{\ell} & \\
0 & \frac{6EI_z}{\ell^2} & 0 & 0 & 0 & \frac{2EI_z}{\ell} & 0 & -\frac{6EI_z}{\ell^2} & 0 & 0 & 0 & \frac{4EI_z}{\ell}
\end{bmatrix} \quad \text{symm}$$

(A.2.60)

where E, G, J, I_y and I_z are Young Modulus, Shear Modulus and the inertia in x, y and z direction, respectively.

The components of mass matrix are calculated from the shape function in Table A.1. For the mass component in the axial direction, these values are given by

$$m_{11} = \int_0^\ell \overline{m}\psi_1 \psi_1 (x)\, dx,$$

$$= \rho A \int_o^\ell \left(1 - \frac{x}{\ell}\right)^2 dx,$$

$$= \frac{\rho A \ell}{3}. \qquad \text{(A.2.61)}$$

$$m_{17} = \int_0^\ell \overline{m}\psi_1 \psi_7 (x)\, dx,$$

$$= \rho A \int_o^\ell \left(1 - \frac{x}{\ell}\right)\left(\frac{x}{\ell}\right) dx,$$

$$= \frac{\rho A \ell}{6}. \qquad \text{(A.2.62)}$$

$$m_{77} = \int_0^{\ell} \overline{m} \psi_7 \psi_7 (x)\, dx,$$

$$= \rho A \int_o^{\ell} \left(\frac{x}{\ell} \right)^2 dx,$$

$$= \frac{\rho A \ell}{3}. \qquad \text{(A.2.63)}$$

For the mass component in the rotational direction, the values are given by

$$m_{44} = \int_0^{\ell} I_{\overline{m}} \psi_4 (x) \psi_4 (x)\, dx,$$

$$= I_{\overline{m}} \int_0^{\ell} \left(1 - \frac{x}{\ell} \right)^2 dx,$$

$$= I_{\overline{m}} \frac{\ell}{3}. \qquad \text{(A.2.64)}$$

$$m_{4,10} = \int_0^{\ell} I_{\overline{m}} \psi_4 (x) \psi_{10} (x)\, dx,$$

$$= I_{\overline{m}} \int_0^{\ell} \left(1 - \frac{x}{\ell} \right) \left(\frac{x}{\ell} \right) dx,$$

$$= I_{\overline{m}} \frac{\ell}{6}. \qquad \text{(A.2.65)}$$

$$m_{10,10} = \int_0^{\ell} I_{\overline{m}} \psi_{10} (x) \psi_{10} (x)\, dx,$$

$$= I_{\overline{m}} \int_0^{\ell} \left(\frac{x}{\ell} \right) \left(\frac{x}{\ell} \right) dx,$$

$$= I_{\overline{m}} \frac{\ell}{3}. \qquad \text{(A.2.66)}$$

For the mass component in the x-y plane, the values are given by

$$m_{2,2} = \int_0^{\ell} \rho A \psi_2(x) \psi_2(x)\, dx,$$

$$= \rho A \int_0^{\ell} \left(1 - \frac{3x^2}{\ell^2} + \frac{2x^3}{\ell^3}\right)\left(1 - \frac{3x^2}{\ell^2} + \frac{2x^3}{\ell^3}\right) dx,$$

$$= \frac{13}{35} \rho A \ell. \qquad \text{(A.2.67)}$$

$$m_{2,6} = \int_0^{\ell} \rho A \psi_2(x) \psi_6(x)\, dx,$$

$$= \rho A \int_0^{\ell} \left(1 - \frac{3x^2}{\ell^2} + \frac{2x^3}{\ell^3}\right)\left(x - \frac{2x^2}{\ell} + \frac{x^3}{\ell^2}\right) dx,$$

$$= \frac{11}{210} \rho A \ell. \qquad \text{(A.2.68)}$$

$$m_{2,8} = \int_0^{\ell} \rho A \psi_2(x) \psi_8(x)\, dx,$$

$$= \rho A \int_0^{\ell} \left(1 - \frac{3x^2}{\ell^2} + \frac{2x^3}{\ell^3}\right)\left(\frac{3x^2}{\ell^2} - \frac{2x^3}{\ell^3}\right) dx,$$

$$= \frac{9}{70} \rho A \ell. \qquad \text{(A.2.69)}$$

$$m_{2,12} = \int_0^{\ell} \rho A \psi_2(x) \psi_{12}(x)\, dx,$$

$$= \rho A \int_0^{\ell} \left(1 - \frac{3x^2}{\ell^2} + \frac{2x^3}{\ell^3}\right)\left(-\frac{x^2}{\ell} + \frac{x^3}{\ell^2}\right) dx,$$

$$= \frac{-13}{420} \rho A \ell. \qquad \text{(A.2.70)}$$

$$m_{6,6} = \int_0^{\ell} \rho A \psi_6(x) \psi_6(x)\, dx,$$

$$= \rho A \int_0^\ell \left(x - \frac{2x^2}{\ell} + \frac{x^3}{\ell^2} \right) \left(x - \frac{2x^2}{\ell} + \frac{x^3}{\ell^2} \right) dx ,$$

$$= \frac{1}{105} \rho A \ell . \qquad \text{(A.2.71)}$$

$$m_{6,8} = \int_0^\ell \rho A \psi_6(x) \psi_8(x) dx ,$$

$$= \rho A \int_0^\ell \left(x - \frac{2x^2}{\ell} + \frac{x^3}{\ell^2} \right) \left(\frac{3x^2}{\ell^2} - \frac{2x^3}{\ell^3} \right) dx ,$$

$$= \frac{13}{420} \rho A \ell . \qquad \text{(A.2.72)}$$

$$m_{6,12} = \int_0^\ell \rho A \psi_6(x) \psi_{12}(x) dx ,$$

$$= \rho A \int_0^\ell \left(x - \frac{2x^2}{\ell} + \frac{x^3}{\ell^2} \right) \left(-\frac{x^2}{\ell} - \frac{x^3}{\ell^2} \right) dx ,$$

$$= -\frac{3}{420} \rho A \ell^3 . \qquad \text{(A.2.73)}$$

$$m_{8,8} = \int_0^\ell \rho A \psi_8(x) \psi_8(x) dx ,$$

$$= \rho A \int_0^\ell \left(\frac{3x^2}{\ell^2} - \frac{2x^3}{\ell^3} \right) \left(\frac{3x^2}{\ell^2} - \frac{2x^3}{\ell^3} \right) dx ,$$

$$= \frac{13}{35} \rho A \ell . \qquad \text{(A.2.74)}$$

$$m_{8,12} = \int_0^\ell \rho A \psi_8(x) \psi_{12}(x) dx ,$$

$$= \rho A \int_0^\ell \left(\frac{3x^2}{\ell^2} - \frac{2x^3}{\ell^3} \right) \left(-\frac{x^2}{\ell} + \frac{x^3}{\ell^2} \right) dx ,$$

$$= -\frac{11}{210}\rho A\ell^2 . \qquad \text{(A.2.75)}$$

$$m_{12,12} = \int_0^\ell \rho A\psi_{12}(x)\psi_{12}(x)\,dx ,$$

$$= \rho A\int_0^\ell \left(-\frac{x^2}{\ell}+\frac{x^3}{\ell^2}\right)\left(-\frac{x^2}{\ell}+\frac{x^3}{\ell^2}\right)dx ,$$

$$= \frac{1}{105}\rho A\ell^3 . \qquad \text{(A.2.76)}$$

For the mass component in the x-z plane, the values are given by

$$m_{3,3} = \int_0^\ell \rho A\psi_3(x)\psi_3(x)\,dx ,$$

$$= \rho A\int_0^\ell \left(1-\frac{3x^2}{\ell^2}+\frac{2x^3}{\ell^3}\right)\left(1-\frac{3x^2}{\ell^2}+\frac{2x^3}{\ell^3}\right)dx ,$$

$$= \frac{39}{105}\rho A\ell . \qquad \text{(A.2.77)}$$

$$m_{3,5} = \int_0^\ell \rho A\psi_3(x)\psi_5(x)\,dx ,$$

$$= \rho A\int_0^\ell \left(1-\frac{3x^2}{\ell^2}+\frac{2x^3}{\ell^3}\right)\left(-x+\frac{2x^2}{\ell}-\frac{x^3}{\ell^2}\right)dx ,$$

$$= -\frac{11}{210}\rho A\ell^2 . \qquad \text{(A.2.78)}$$

$$m_{3,9} = \int_0^\ell \rho A\psi_3(x)\psi_9(x)\,dx ,$$

$$= \rho A\int_0^\ell \left(1-\frac{3x^2}{\ell^2}+\frac{2x^3}{\ell^3}\right)\left(\frac{3x^2}{\ell^2}-\frac{2x^3}{\ell^3}\right)dx ,$$

$$= \frac{27}{210}\rho A\ell . \qquad \text{(A.2.79)}$$

$$m_{3,11} = \int_0^{\ell} \rho A \psi_3(x) \psi_{11}(x)\, dx ,$$

$$= \rho A \int_0^{\ell} \left(1 - \frac{3x^2}{\ell^2} + \frac{2x^3}{\ell^3}\right)\left(\frac{x^2}{\ell} + \frac{x^3}{\ell^2}\right) dx ,$$

$$= \frac{13}{420} \rho A \ell^2 . \qquad \text{(A.2.80)}$$

$$m_{5,5} = \int_0^{\ell} \rho A \psi_5(x) \psi_5(x)\, dx ,$$

$$= \rho A \int_0^{\ell} \left(-x + \frac{2x^2}{\ell} - \frac{x^3}{\ell^2}\right)\left(-x + \frac{2x^2}{\ell} - \frac{x^3}{\ell^2}\right) dx ,$$

$$= \frac{1}{105} \rho A \ell^3 . \qquad \text{(A.2.81)}$$

$$m_{5,9} = \int_0^{\ell} \rho A \psi_5(x) \psi_9(x)\, dx ,$$

$$= \rho A \int_0^{\ell} \left(-x + \frac{2x^2}{\ell} - \frac{x^3}{\ell^2}\right)\left(\frac{3x^2}{\ell^2} - \frac{2x^3}{\ell^3}\right) dx ,$$

$$= -\frac{13}{420} \rho A \ell^2 . \qquad \text{(A.2.82)}$$

$$m_{5,11} = \int_0^{\ell} \rho A \psi_5(x) \psi_{11}(x)\, dx ,$$

$$= \rho A \int_0^{\ell} \left(-x + \frac{2x^2}{\ell} - \frac{x^3}{\ell^2}\right)\left(-\frac{x^2}{\ell} - \frac{x^3}{\ell^2}\right) dx ,$$

$$= -\frac{1}{140} \rho A \ell^3 . \qquad \text{(A.2.83)}$$

$$m_{9,9} = \int_0^{\ell} \rho A \psi 9(x) \psi_9(x)\, dx ,$$

$$= \rho A \int_0^{\ell} \left(\frac{3x^2}{\ell^2} - \frac{2x^3}{\ell^3} \right) \left(\frac{3x^2}{\ell^2} - \frac{2x^3}{\ell^3} \right) dx ,$$

$$= \frac{13}{35} \rho A \ell . \qquad \text{(A.2.84)}$$

$$m_{9,11} = \int_0^{\ell} \rho A \psi_9(x) \psi_{11}(x) \, dx ,$$

$$= \rho A \int_0^{\ell} \left(\frac{3x^2}{\ell^2} - \frac{2x^3}{\ell^3} \right) \left(\frac{x^2}{\ell} - \frac{x^3}{\ell^2} \right) dx ,$$

$$= \frac{11}{210} \rho A \ell^2 . \qquad \text{(A.2.85)}$$

$$m_{11,11} = \int_0^{\ell} \rho A \psi_{11}(x) \psi_{11}(x) \, dx ,$$

$$= \rho A \int_0^{\ell} \left(\frac{x^2}{\ell} - \frac{x^3}{\ell^2} \right) \left(\frac{x^2}{\ell} - \frac{x^3}{\ell^2} \right) dx ,$$

$$= \frac{1}{105} \rho A \ell^3 . \qquad \text{(A.2.86)}$$

The mass matrix of frame element in local coordinate is given by (Bur, 1994)

$$\bar{\mathbf{m}}_{\mathbf{e}} = \frac{\rho A \ell}{420} \begin{bmatrix}
140 & & & & & & & & & & & \\
0 & 156 & & & & & & & & & & \\
0 & 0 & 156 & & & & & & & & & \\
0 & 0 & 0 & \frac{140 I_{\bar{m}}}{\bar{m}} & & & & & & & & \\
0 & 0 & -22\ell & 0 & 4\ell^2 & & & & & & & \\
0 & 22\ell & 0 & 0 & 0 & 4\ell^2 & & & & & & \\
70 & 0 & 0 & 0 & 0 & 0 & 140 & & & & & \\
0 & 54 & 0 & 0 & 0 & 13\ell & 0 & 156 & & & & \\
0 & 0 & 54 & 0 & -13\ell & 0 & 0 & 0 & 156 & & & \\
0 & 0 & 0 & \frac{70 I_{\bar{m}}}{\bar{m}} & 0 & 0 & 0 & 0 & 0 & \frac{140 I_{\bar{m}}}{\bar{m}} & & \\
0 & 0 & 13\ell & 0 & -3\ell^2 & 0 & 0 & 0 & 22\ell & 0 & 4\ell^2 & \\
0 & -13\ell & 0 & 0 & 0 & -3\ell^2 & 0 & -22\ell & 0 & 0 & 0 & 4\ell^2
\end{bmatrix} \qquad \text{(A.2.87)}$$

where $\rho, A, \ell, \overline{m}$ and $I_{\overline{m}}$ are mass density, cross sectional area, length, mass per unit of length and torque inertia of the frame element, respectively.

A.2.2 Stiffness Matrix and Mass Matrix in Global Coordinate

The local coordinate system and global coordinated system in the three dimensional space is shown in Fig. A.6

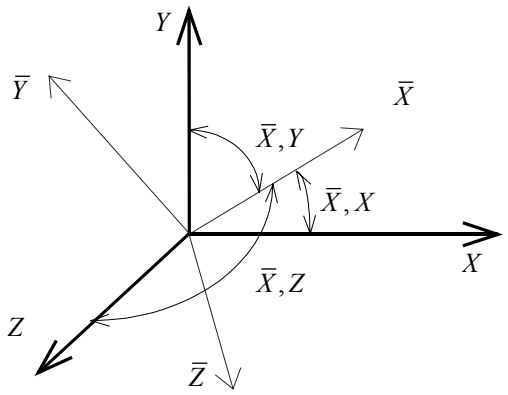

Fig. A.6 Axes rotation in 3 dimensional space.

The vector component of one axes can be expressed as the function of another axes components. This relation is expressed in matrix form as

$$\begin{Bmatrix} \overline{X} \\ \overline{Y} \\ \overline{Z} \end{Bmatrix} = \begin{bmatrix} \ell_1 & m_1 & n_1 \\ \ell_2 & m_2 & n_2 \\ \ell_3 & m_3 & n_3 \end{bmatrix} \begin{Bmatrix} X \\ Y \\ Z \end{Bmatrix} . \qquad \text{(A.2.88)}$$

where

ℓ_1 = cosine between($\overline{X}$, X),

m_1 = cosine between ($\overline{X}$, Y),

n_1 = cosine between ($\overline{X}$, Z),

ℓ_2 = cosine between ($\overline{Y}$, X),

m_2 = cosine between ($\overline{Y}$, Y)…..

or

$$\ell_1 = \cos\frac{X_j - X_i}{L}, \tag{A.2.89}$$

$$m_1 = \cos\frac{Y_j - Y_i}{L}, \tag{A.2.90}$$

$$n_1 = \cos\frac{Z_j - Z_i}{L}. \tag{A.2.91}$$

where :

$$L = \sqrt{\left(X_j - X_i\right)^2 + \left(Y_j - Y_i\right)^2 + \left(Z_j - Z_i\right)^2}\ . \tag{A.2.92}$$

The direction from coordinated axes $\overline{Z}$ can be obtained by assumed that each vector $\vec{Z}$ in $\overline{Z}$ axes direction should be perpendicular to the plane which is constructed by two vector. These two vectors consist of a vector $\vec{X}$ which is originated from node α to node β and another vector is vector $\vec{P}$ which is originated from node α to point P. The orthogonality is showed by cross product

$$\vec{Z} = \vec{X} \times \vec{P}\ , \tag{A.2.93}$$

If the vector components in Eqs. (A.2.89)-(A.2.91) is substituted then we have

$$Z_X\hat{\mathbf{i}} + Z_Y\hat{\mathbf{j}} + Z_Z\hat{\mathbf{k}} = \begin{vmatrix} \hat{\mathbf{i}} & \hat{\mathbf{j}} & \hat{\mathbf{k}} \\ X_\beta - X_\alpha & Y_\beta - Y_\alpha & Z_\beta - Z_\alpha \\ X_P - X_\alpha & Y_P - Y_\alpha & Z_P - Z_\alpha \end{vmatrix}. \tag{A.2.94}$$

where $\hat{\mathbf{i}}$, $\hat{\mathbf{j}}$ and $\hat{\mathbf{k}}$ are the unit vector in the global axes. The cosine direction in $\overline{Z}$ axes can be calculated as

$$\cos\overline{Z}X = \frac{Z_X}{L_Z},\ \cos\overline{Z}Y = \frac{Z_Y}{L_Z},\ \cos\overline{Z}Z = \frac{Z_Z}{L_Z}, \tag{A.2.95}$$

where

$$Z_X = \left(Y_\beta - Y_\alpha\right)\left(Z_P - Z_\alpha\right) - \left(Y_P - Y_\alpha\right)\left(Z_\beta - Z_\alpha\right), \tag{A.2.96}$$

$$Z_Y = \left(Z_\beta - Z_\alpha\right)\left(X_P - X_\alpha\right) - \left(Z_P - Z_\alpha\right)\left(X_\beta - X_\alpha\right), \tag{A.2.97}$$

$$Z_Z = \left(X_\beta - X_\alpha\right)\left(Y_P - Y_\alpha\right) - \left(X_P - X_\alpha\right)\left(Y_\beta - Y_\alpha\right), \tag{A.2.98}$$

and

$$L_Z = \sqrt{Z_X^2 + Z_Y^2 + Z_Z^2}\,. \tag{A.2.99}$$

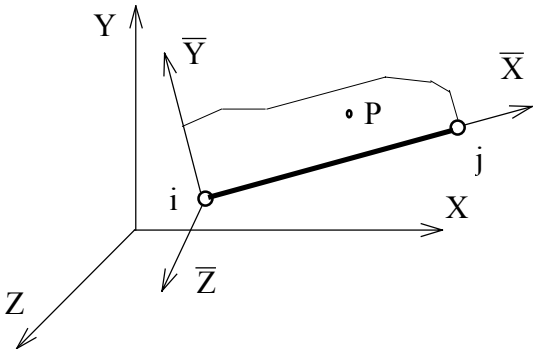

Fig. A.7 The P point in space frame.

By using the same analogy as in the $\overline{Z}$ axes, the cosine direction in the $\overline{Y}$ axes can be obtained by using the orthogonality between a vector $\vec{Y}$ in the $\overline{Y}$ axes with the unit vector $\vec{Z}_1$ and $\vec{X}_1$ in $\overline{X}$ and $\overline{Z}$ axes, respectively

$$\vec{Y} = \vec{Z}_1 \times \vec{X}_1, \tag{A.2.100}$$

or

$$Y_X\hat{\mathbf{i}} + Y_Y\hat{\mathbf{j}} + Y_Z\hat{\mathbf{k}} = \begin{vmatrix} \hat{\mathbf{i}} & \hat{\mathbf{j}} & \hat{\mathbf{k}} \\ \cos\overline{Z}X & \cos\overline{Z}Y & \cos\overline{Z}Z \\ \cos\overline{X}X & \cos\overline{X}Y & \cos\overline{X}Z \end{vmatrix}, \tag{A.2.101}$$

where

$$Y_X = \cos\overline{Z}Y \cdot \cos\overline{X}Z - \cos\overline{X}Y \cdot \cos\overline{Z}Z\,, \tag{A.2.102}$$

$$Y_Y = \cos\overline{Z}Z \cdot \cos\overline{X}X - \cos\overline{X}Z \cdot \cos\overline{Z}X\,, \tag{A.2.103}$$

$$Y_Z = \cos\overline{Z}X \cdot \cos\overline{X}Y - \cos\overline{X}X \cdot \cos\overline{Z}Y\,, \tag{A.2.104}$$

where cosine value are calculated as

$$\cos\overline{Y}X = \frac{Y_X}{L_Y},\ \ \cos\overline{Y}Y = \frac{Y_Y}{L_Y}, \cos\overline{Y}Z = \frac{Y_Z}{L_Y}, \tag{A.2.105}$$

and L_Y is calculated as follows

$$L_Y = \sqrt{Y_X^2 + Y_Y^2 + Y_Z^2}\ . \tag{A.2.106}$$

The cosine value of rotation matrix **T** can be calculated using nodal point α and β which is located at the end of the frame and one point P which located in $\overline{\mathrm{X}}-\overline{\mathrm{Y}}$ plane. The calculation become simpler if the P point is located in the local axes $\overline{\mathrm{Y}}$. The displacement transformation for 3D coordinate is :

$$\begin{Bmatrix} \overline{u}_{ix} \\ \overline{u}_{iy} \\ \overline{u}_{iz} \\ \overline{u}_{jx} \\ \overline{u}_{jy} \\ \overline{u}_{jz} \end{Bmatrix} = \left[\begin{array}{ccc:ccc} \ell_1 & m_1 & n_1 & 0 & 0 & 0 \\ \ell_2 & m_2 & n_2 & 0 & 0 & 0 \\ \ell_3 & m_3 & n_3 & 0 & 0 & 0 \\ \hdashline 0 & 0 & 0 & \ell_1 & m_1 & n_1 \\ 0 & 0 & 0 & \ell_2 & m_2 & n_2 \\ 0 & 0 & 0 & \ell_3 & m_3 & n_3 \end{array}\right] \begin{Bmatrix} u_{ix} \\ u_{iy} \\ u_{iz} \\ u_{jx} \\ u_{jy} \\ u_{jz} \end{Bmatrix}, \tag{A.2.107}$$

or

$$\overline{\mathbf{U}} = \mathbf{T}\,\mathbf{U}\ . \tag{A.2.108}$$

where $\overline{\mathbf{U}}$ is the displacement in the local coordinated, **T** is transformation matrix and **U** is the displacement in global coordinate.

The stiffness matrix in the global coordinate is calculated as

$$\mathbf{k_e} = \mathbf{T}^{-1}\overline{\mathbf{k}}_e\mathbf{T}\,. \tag{A.2.109}$$

and the mass matrix in global coordinate is

$$\mathbf{m_e} = \mathbf{T}^{-1}\overline{\mathbf{m}}_\mathbf{e}\mathbf{T}\,. \tag{A.2.110}$$

BIBLIOGRAPHY

Abbate, C., Micali,E., and Giorgianni, C., Affective Correlates of Occupational Exposure to Whole-Body Vibration: a Case Control Study, *Psychotherapy and Psychosomatics*, Vol. 73(2004), pp.375-379.

Allen, D.E., and Pernica, G., A simple absorber for walking vibrations, *Canadian Journal of Civil Engineering*, Vol. 11(1984), pp.112-117.

Babitsky, V.I., and Veprik, A.M., Universal bumpered vibration isolator for severe environment, *J. Sound and Vibration*, Vol. 218(1998), pp. 269-292.

Bayman, B.F., Model of the behavior of solid objects during collision, *Am.J.Phys.*, Vol. 44(7)(1976), pp.671-676.

Bekesy, G..V., Vibration of the head in the sound field and its role in hearing by bone construction, *Journal of the Acoustical Society of America.*, Vol. 20(1948), pp.749-760.

Brach, R.M., *Mechanical Impact Dynamic* : *Rigid Body Collision*. John Wiley and Sons, New York (1991).

Bur, M., *Dynamische Analyse Linearer und Nichtlinearer Structuren Anhand Theoretischer und Versuchstechnischer Untersuchungen*, Diss RWTH Aachen(1994).

Ceanga, V., and Hurmuzlu, Y., A New look at an old problem: Newtons Cradle, *ASME Journal of Applied Mechanics*, Vol. 68(2001), pp. 575-583.

Chatterjee, A., On the realism of complementarity conditions in rigid body collision, *Nonlinear Dynamics*, Vol.20 (1999), pp. 159-168.

Chatterjee, A., *Rigid Body Collisions: Some General Considerations, New Collision Laws, and Some Experimental data*. PHD thesis, Cornel University(1997).

Chatterjee, A., Ruina, A., Two interpretations of rigidity in rigid body collisions, *ASME Journal of Applied Mechanics*, Vol.65 (1998),pp.894-900.

Chung,J.L., and Ming C.K., Coefficients of restitution based on a fractal surface model, *ASME Journal of Applied Mechanics,* Vol.70 (2003), pp.339-345.

Collette, F.S., A combined tuned absorber and pendulum impact damper under random excitation, *J. Sound and Vibration*, Vol. 216(1998), pp.199-213.

Craggi, A., A Finite element Model for Acoustically Lined Small Rooms, *J. Sound and Vibration*, Vol. 108(1986), pp. 327-337.

Crawford, F.S., A theorem on elastic collisions between ideal rigid bodies, *Am.J.Phys.*, Vol. 57(2)(1989), pp.121-125.

Escalona, J.M., Mayo, J.M., and Dominguez, J., A critical study of the use of the generalized impulse-momentum balance equations in flexible multibody system, *J. Sound and Vibration*, Vol. 217(1999), pp.523-545.

Fegelman, K.J.L., and Gross,K., Dynamics of a flexible beam contacting a linear spring at low frequency excitation : experiment and analysis, *J. Vibration and Acoustics*, Vol.124 (2002), pp.237-249.

Friend.R.D., and Kinra, V.K., Particle impact damping, *J. Sound and Vibration*, Vol. 233(2000), pp. 93-118.

Goldsmith, W., *Impact: The Theory and Physical Behavior of Colliding Solids*, Edward Arnold, Ltd., London, 1960.

Griffin, M.J., *Handbook of human Vibration*, Academic Press, San Diego, CA, USA(1990).

Hanagan, L.M., and Murray, T.M., Active control approach for reducing floor vibrations, *ASCE Journal of Structural Engineering*, Vol. 123(1997), pp.1497-1505.

Hanagan, L.M., and Murray, T.M., Experimental results from the active control of floor motion. *Proceedings of the first world conference on structural control*, Pasadena, Calif., Vol. 3(1994), pp. FP4-71-FP4-78.

Harris, C.M. and Crede, C.E., *Shock and Vibration Handbook*, McGraw-Hill, New York, USA(1976).

Herrmann, F., and Schmalzle, P., Simple explanation of well-known collision experiment, *Am.J.Phys.*, Vol. 49(8)(1981), pp.761-764.

Herrmann, F., and Seitz, M., How does the ball-chain work, *Am.J.Phys.*, Vol. 50(11)(1984), pp.977-981.

Hongo, T., Sato, H., Iwata, Y., Komatsuzaki, T., and Hongo, Y., Modeling and Analysis of Impact Syatem Composed of Ball and Plane, *J.Jpn. Soc.Mech.Eng.*,(in Japanese), Vol.65, No.634, C(1999), pp.2287-2293.

Hu, B., Eberhard, P., and Schiehlen, W., Symbolical impact analysis for a falling canonical rod against the rigid ground, *J. Sound and Vibration*, Vol. 240(2001), pp.41-57.

Hurmuzlu, Y., An Energy based coefficient of restitution for planar impacts of slender bars with massive external surfaces, *ASME Journal of Applied Mechanics*, Vol. 65(1998), pp. 952-962.

Johnson, K.L., *Contact Mechanics*. Cambridge University Press(1985).

Kane, T.R., and Levinson,D.A., *Dynamics: Theory and Applications*, McGraw-Hill, New York(1985).

Kilmister, C.W., and Reeve, J.E., *Rational Mechanics*. Longmans, London(1966).

Kim, D.H., Park,J.W., Lee, G..S., and Lee, K.I., Active impact control system design with a hydraulic damper, *J. Sound and Vibration*. Vol. 250(2002), pp. 485-501

Lagrange, J.L., *Mechanique Analytique*. Mme. Ve Courcier, Paris(1811).

Lee, C.H., and Byrne, K.P., *Calculating the time-histories of impacting systems described by their receptances, J. Vibration and Acoustics*, Vol. 120(1998), pp.491-495.

Love, A.E.H., *A Treatise on the Mathematical Theory of Elasticity* (Dover, New York), 4th ed. (1944), pp.193-200.

McKay, J.R., *Human Response to Vibration: Some Studies of Perception and Startle*, PhD Thesis, University of Southhampton, England (1972).

Newton, I., *The Principia*. University of California Press, 1999, Translation of the third(1976) edition, by I. Bernard Cohen and Anne Whitman.

Peterka, F., and Blazejczyk, B., Some aspects of the dynamical behavior of the impact damper, *J. Vibration and Control*. Vol.11(2005), pp. 459-479.

Pinnington, R.J., Collision dynamics of two adjacent oscillators, *Journal of Sound and Vibration*, Vol. 268(2003), pp.343-360.

Pinnington, R.J., Energy dissipation prediction in a line of colliding oscillators, *Journal of Sound and Vibration*, Vol. 268(2003), pp.361-384.

Rajalingham, C., Rakheja, S., Analysis of impact force variation during collision of two bodies using a single degree of freedom system model, *J. Sound and Vibration*, Vol. 229(2000), pp.823-835.

Reinsch, M., Dispersion-free linear chain. *Am.J.Phys.*, Vol. 62(3)(1994), pp.271-278.

Routh, E.J., *Dynamics of a system of Rigid Bodies*, Macmillan and Co., London, sixth edition(1897).

Schedin, S., Lambourge, C., and Chaigne, A., Transient sounds fields from impacted plates: comparison between numerical simulations and experiments, *J. Sound and Vibration*, Vol. 221(1999), pp.471-490.

Setareh, M., and Hanson, R.D., Tuned mass dampers to control floor vibrations from humans, *ASCE Journal of Structural Engineering*, Vol. 118(1992), pp.741-762.

Shoenberger, R.W., Subjective Response to Whole-Body Vibration, *Presented at the Meeting of the Acoustical Society of America*, Miami Beach, FL(November 1981).

Smith, C.E., and Liu, P.P., Coefficients of restitution, *ASME Journal of Applied Mechanics*, Vol.59(1992),pp.963-969.

Son, L., Matsuhisa, H., and Utsuno, H., Application of momentum exchange impact damper on reducing the impact induce vibration on press machine, *The Third Asian Conference on Multibody Dynamics(ACMD)*, Tokyo, Japan(2006).

Son, L., Matsuhisa, H., and Utsuno, H., Reducing Floor Impact Vibration and Sound Using a momentum exchange impact damper, *Motion and Vibration Control Conference (MOVIC)*, Daejeon, Korea(2006).

Stoianovici, D., and Hurmuzlu, Y., A Critical study of the applicability of rigid body collision theory, *ASME Journal of Applied Mechanics*, Vol. 63(1996), pp. 307-316.

Tanaka, N., and Kikushima, Y., A Study on the dynamic damper with a preview action(1 st report, a principle of the dynamic damper with a preview action), *J. Jpn. Soc. Mech. Eng*.,(in Japanese), Vol. 52 No.484, C(1986), pp.3176-3183.

Tanaka, N., and Kikushima, Y., A Study on the dynamic damper with a preview action(2 nd report, experiment of the dynamic damper with a preview action), *J. Jpn. Soc. Mech. Eng*.,(in Japanese), Vol. 53 No.487, C(1987), pp.650-655.

Timoshenko, S., Vibration problems in engineering, *Jhon Wiley & Sons*, Fourth Edition(1974).

Webster, A.C., and Vaicajtis, R., Application of tuned mass dampers to control vibrations of composite-floor systems, *Engineering Journal of the American Institute of Steel Construction*, Vol. 29(1992), pp. 116-124.

Whittaker, E.T., *A Treatise on the Analytical Dynamics of Particles and Rigid Bodies*, Cambridge University Press, fourth edition(1947).

Wu, X., and Grifffin, M.J., A semi-active control policy to reduce the occurrence and severity of and-stop impacts in a suspension seat with an electrorheological fluid damper, J. *Sound and Vibration*. Vol.203(1997), pp. 781-793.

Przemieniecky, J.S., *Theory of Matrix Structural Analysis*. McGraw-Hill (1967).

Zhong, Z.H., *Finite Element Procedure for Contact-Impact Problems*. Oxford University Press (1993).

ACKNOWLEDGEMENTS

I would like to thank my advisors, Professor Hiroshi MATSUHISA and Associate Professor Hideo UTSUNO for their patience and guidance throughout my time as PhD student. Their enthusiasm and interest in the work of all their students is encouraging. I would also like to thank to Research Associate Jeong Gyu PARK for offering valuable suggestions in my research, and technician Mr. SAWADA for making perfect experimental setup.

I would like to thank Professor Mulyadi BUR at Andalas University, who recommended me to Kyoto University and providing valuable advices during my study in Kyoto University.

I would like to thank Dr. Keisuke YAMADA, Dr. Yanqing LIU, Dr. Tomonao OKUYAMA, Dr. Kourou UENISHI, Makoto KAWACHI, Daisaku NAKATANI, Tomosakuro MUKAI and all my current and former Vibration Control labmates for their help, companionship and memories.

I would like to thank my family and friends for their love and support. I would like to express my deepest gratitude to my parents. My Family in Indonesia deserves my thanks for their prayers and love. I would especially like to thank my wife, Tanti Fauliza, for her encouragement and patience. I would like to thank my sons, Abdurrahim Ali Hatim and Muhammad Zuhdi Yasykur. Their smile offered me welcome relief from work.

Finally, I would like to thank the Association of International Education of Japan (AIEJ) for providing my financial support for three years. The developed educating method, excellent studying environment and perfect managing system of Kyoto University gave me deep impression.